# IDENTIFICATION OF NOVEL TREATMENTS FOR A HEREDITARY STROKE DISORDER USING QUANTITATIVE PHENOTYPIC FINGERPRINTING

by

Christopher C. Gibson

A dissertation submitted to the faculty of
The University of Utah
in partial fulfillment of the requirements for the degree of

Doctor of Philosophy

Department of Bioengineering

The University of Utah

December 2013

## The University of Utah Graduate School

## STATEMENT OF DISSERTATION APPROVAL

The dissertation of Christopher C. Gibson

has been approved by the following supervisory committee members:

| | | |
|---|---|---|
| Dean Y. Li | , Chair | 10/30/2013<br>Date Approved |
| Yan-Ting E. Shiu | , Co-Chair | 10/30/2013<br>Date Approved |
| Vladimir Hlady | , Member | 10/30/2013<br>Date Approved |
| Richard D. Rabbitt | , Member | 10/30/2013<br>Date Approved |
| Andrew S. Weyrich | , Member | 10/30/2013<br>Date Approved |

and by Patrick A. Tresco , Chair of

the Department of Bioengineering

and by David B. Kieda, Dean of The Graduate School.

ABSTRACT

Destabilization of the endothelial monolayer lining blood vessels has profound consequences on organismal homeostasis. Vascular instability plays a well-known role in the pathophysiology of diseases from sepsis to stroke. A variety of factors are known to influence endothelial function, including the extracellular milieu, biomechanical factors, various molecular pathways, as well as genetic elements. Many factors promoting vascular instability have been described; however, far fewer studies have identified factors promoting stability. No overarching theory of vascular stability has yet been proposed that takes into account extracellular, biomechanical, molecular, and genetic variables.

In this dissertation, I detail studies of extracellular matrix cues, molecular pathways, and genetic factors in an attempt to identify commonalities associated with regulation of vascular stability. I first show that the extracellular matrix protein elastin normalizes endothelial cell function. Next, I demonstrate a critical role of the small GTPase ARF6 in mediating cytokine-induced endothelial instability. I also identify a crucial role of ARF6 in mediating transduction of mechanical signals in the endothelium. Finally, I describe a central role of various genes associated with a human disease, Cerebral Cavernous Malformation (CCM), in endothelial stability.

During the course of these studies, I developed and utilized a variety of tools not often found in molecular biology labs. I built new apparatuses and wrote software programs to answer the questions I had, rather than relying on what had already been built by others. Perhaps my largest contribution to the Li laboratory has been to propagate the use of these new systems to molecular biologists who may have a better capability to ask important questions, and who now have the ability to answer their own questions more quickly, more efficiently, and without the inherent bias associated with the standard protocols used in the majority of molecular biology labs.

Finally, during my last two years in the laboratory, I further refined and integrated the tools I developed with new tools available from the Broad Institute to quantitatively evaluate endothelial stability

through measurement of both structural and functional phenotypes. Using quantification of structural and functional phenotypes, I identified multiple drugs that ameliorate *in vitro* CCM models, and found two drugs that significantly reduce the formation of lesions in murine models of CCM disease. Further, I found that one of these compounds was protective against diverse destabilizing cues in the endothelium. These discoveries are important for the study of CCM disease, for patients with CCM disease, and have implications for many other diseases in the future.

Overall, my studies resulted in specific new mechanistic insights into a wide-variety of factors that promote endothelial stability. More important is the development of a multilayered strategy and platform that can be applied to study effects of extracellular, biomechanical, molecular, and genetic cues on the endothelium either alone or in any combination. In the immediate future, this platform will serve as a vehicle for creating an over-arching model of vascular stability. Beyond this application, this same platform can be rapidly scaled to answer broad questions about factors crucial in health and disease across a wide variety of other cell and organ types. I intend to use the approach I developed and describe in my dissertation to try to untangle how all genes, all proteins, all diseases, and all drugs interact – a lofty goal to be sure.

This dissertation is dedicated first to my family, without whose support I would have been lost. Second, this dissertation is dedicated to Carol Ponganis, Dave Corkran, Kirk Thomas, and Dean Li, four mentors who have especially inspired and affected me through their passion for their work.

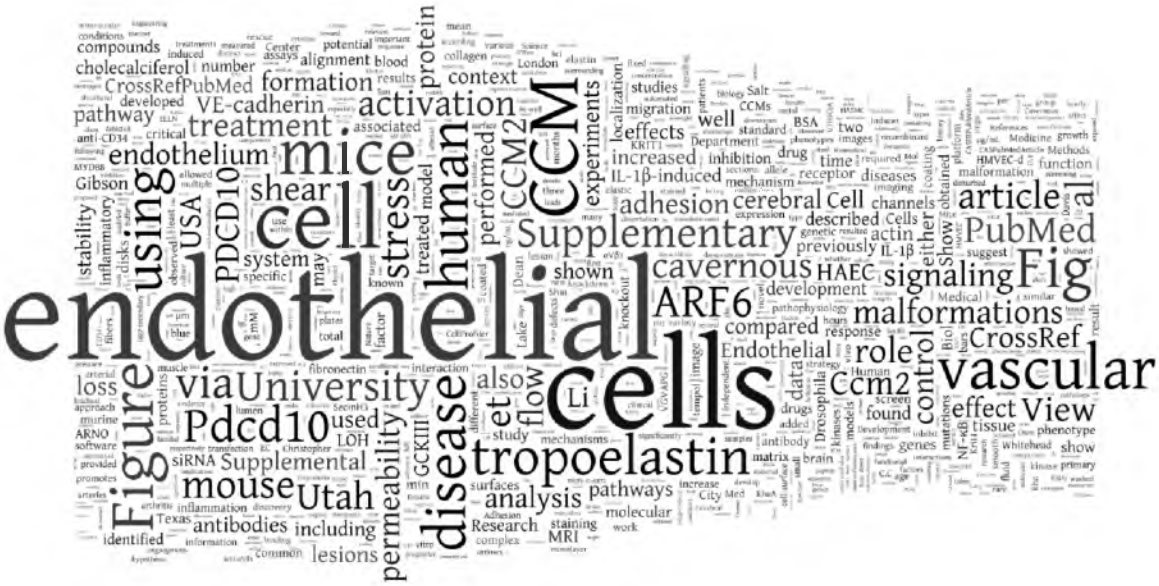
endothelial
cells
CCM
mice
cell
human
tropoelastin
vascular
Figure
disease
Supplementary
activation
using
Fig
PubMed
malformations
signaling
cavernous
ARF6
University
Pdcd10
mouse
Utah
via
treatment
endothelium
shear
stress
protein
flow
permeability
adhesion
cerebral
article
role
CCM2
control
CrossRef
effect
View
tissue
analysis
pathways
molecular
lesions
antibodies
including
Texas
identified
Endothelial
compared
development
HAEC
shown
PDCD10
USA
Gibson
formation
CrossRefPubMed
VE-cadherin
pathway
cholecalciferol
compounds
alignment
blood
context
localization
experiments
performed
CCM2
effects
increased
inhibition
drug
receptor
diseases
IL-1β-induced
mechanism
Cell
channels
actin
described
previously
either
Show
suggest
obtained
function
malformation
HMVEC-d
Methods
Medicine
growth
Platform
Department
BSA
two
images
time
required
standard
CCMs
Salt
studies
migration
well
London
collagen
elastin
number
assays
potential
Greater
treated
model
factor
known
specific
system
may
total
blue
plates
knockout
Dean
Shin
Lalie
Cell
Biol
Medical
similar
result
response
hours
pathophysiology
Drosophila
drugs
added
antibody
matrix
brain
genes
found
screen
Development
models
kinases
mutations
phenotype
primary
kinase
fluid
Whitehead
show
NF-κB
Erk1
Erk2
western
blot
Ccm2
data
human
virus
strategy
vivo
Li
et
al
also
study
mechanisms
surfaces
Adhesion
complex
staining
MRI
Research
City
Med
work
increase
significantly
samples
findings
inhibit
Christopher
transfection
Texas
inflammation
discovery
Common
information
binding
engagement
hypothesis
arterial
artery
identified
GCKIII
LOH
siRNA
Supplemental
ARNO
software
murine
approach
loss
fibronectin
interaction
proteins
muscle
lumen
Secin(1)
arterial
inflammatory
stability
disks
fibers
blue
pink
platen
factor
Cell/Matrix
Lalie
Dean
Shin
knockout
two-dimensional
Scaled
shown
expression
genetic
results
Cells
IL-1β
suggest
showed
Medicine
Methods
HMVEC-d
malformation
function
channels
Cell
diseases
receptor
mechanism
IL-1β-induced
inhibition
drug
time
required
Department
BSA
two
images
standard
CCMs
Salt
studies
migration
well
London
collagen
elastin
number
assays
potential
Greater
treated
model
factor
known
specific
system
may
total
blue
plates
knockout
Dean
Shin
Lalie
Cell
Biol
Medical
similar
result
response
hours
pathophysiology
Drosophila
drugs
added
antibody
matrix
brain
genes
found
screen
Development
models
kinases
mutations
phenotype
primary
kinase
fluid
Whitehead
show
NF-κB
Erk1
Erk2
western
blot
Ccm2
data
human
virus
strategy
vivo
Li
et
al
also
study
mechanisms
surfaces
Adhesion
complex
staining
MRI
Research
City
Med
work
increase
significantly
samples
findings
inhibit
Christopher
transfection
Texas
inflammation
discovery
Common
information
binding
engagement
hypothesis
arterial
artery
identified
GCKIII
LOH
siRNA
Supplemental
ARNO
software
murine
approach
loss
fibronectin
interaction
proteins
muscle
lumen
Secin(1)
arterial
inflammatory
stability
disks
fibers
blue
pink
platen
factor
Cell/Matrix
Lalie
Dean
Shin
knockout
two-dimensional
Scaled
shown
expression
genetic
results
Cells
IL-1β
suggest
showed

TABLE OF CONTENTS

ACKNOWLEDGEMENTS

I wish to thank the many people who contributed to this work. These include members of the Li Lab, especially Dean Li, Kirk Thomas, Jing Ling, Aubrey Chan, Matthew Smith, Weiquan Zhu, Chadwick Davis, Jay Bowman-Kirigin, Stavros Drakos, Nikolaos Diakos, Shannon Odelberg, Allie Grossmann, Kevin Whitehead, Nyall London, Amy Lim, Tara Mleynek, and Lise Sorensen; my trainees, including Jay Bowman-Kirigan, Joy Hui, and Alex Ho; members of my thesis committee, including Vladimir Hlady, Richard Rabbitt, and Yan-Ting E. Shiu; Anthony Donato, Lisa Lesniewski, and members of their lab, especially Ashley Walker; Andrew Weyrich, Guy Zimmerman, and other members of their lab, especially Robert Campbell; the core facility's staffs, especially Osama Abdullah, Betsy Manos, and Chris Rodesch; the MD/PhD program, who so kindly welcomed me from Texas, especially Jerry Kaplan, Janet Basset, and Alana Welm; and our fantastic administrative support, including Linn Steele, Tatia Forsgren, Julia Pili, Kaycee Howell, and Susan Kazaryan; and various students, faculty, and scientists who provided such helpful feedback on this work, especially Kirill Ostanin and Alan Mueller.

# INTRODUCTION

The endothelium acts as the gatekeeper between the vascular space and the tissue in each organ of the body. Further, the endothelium serves critical roles as both an organ of hemostasis and of immune response. Activation of various pathways within the cells of the endothelium can lead to alterations in the transport of compounds across the endothelium, provocation or inhibition of hemostasis, or an immune response that is either too minimal or so strong that it leads to unnecessary tissue destruction. A wide-variety of cues, both chemical and physical, informs the state of the endothelium.

First, the extracellular milieu, especially the components of the extracellular matrix, can have a profound role in shaping endothelial function. The various extracellular matrix components are secreted by the endothelium and by its neighbors. Extracellular matrix components affect the endothelium through direct receptor-mediated action and by modulating the biophysical environment in which the cells reside. In this dissertation, I illustrate the roles of one such matrix protein, elastin, in promoting endothelial stability.

A variety of different signaling pathways play a well-describe role in endothelial stability such as sphingosine-1P via its canonical receptor or angiopoietin through Tie-2. The endothelial-specific receptor ROBO4 has been shown to play a role in modulation of an activated state in the endothelium, ostensibly through actions on the small GTPase ARF6. I show in this dissertation that activation of ARF6 tends to move the endothelium toward an activated state, while inhibition of ARF6 promotes a less-reactive quiescent state.

Another key mediator of endothelial stability is the biophysical environment which consists of cyclic strain on the endothelium, especially in the larger vessels, as well as flow-mediated shear stresses across the endothelium of all vessels large and small. Abnormal magnitudes of shear stress, or oscillation of shear stresses, can result in activation of a variety of pathways that promote an 'activated' endothelial state in which the endothelial monolayer becomes leaky to both protein and fluid, in which the endothelium can become pro-thrombotic, and in which adhesion and diapedesis of inflammatory cells is increased. I describe in this dissertation the role of ARF6 in regulation of the endothelial response to shear stresses.

Lastly, genetics can play a major role in the predisposition of the endothelium toward a more activated or quiescent state. Genetic mutations can play an indirect role, as is the case in familial hypercholesterolemia. Mutations in the gene *LDLR* lead to an increase in lipoproteins in the serum which lead the endothelium down a self-promoting inflammatory path. Other genetic mutations associated with human disease can have a direct effect on endothelial stability such as the role of *ENG* or *ALK1* in hereditary hemorrhagic telangiectasia (HHT). We study loss of function of genes associated with another human disease, cerebral cavernous malformation (CCM), as a highly isolatable model of endothelial instability. In this dissertation, I characterize the role of two genes associated with CCM disease, CCM2 and CCM3, on vascular stability.

As a bioengineer, my approach to studying myriad different vascular stability cues was different from the typical molecular biologist. I developed new assay systems to test the questions at hand. Most importantly, as my studies progressed, I moved assays toward an automated higher-throughput approach. The motivation for this was to reduce bias inherent in everything humans do, and to enable the laboratory to simultaneously ask and answer many more questions. Along with a push toward automation and higher-throughput, I worked to help my colleagues develop automated analysis algorithms to answer their own research questions. Through this concerted effort, I built a library of high throughput assays and tools that have enable the Li Lab and our collaborators to assess many more variables in a rapid and repeatable manner. By optimizing these various assays and identifying and acquiring additional analysis tools from other laboratories, I have made a lasting contribution to the laboratory. As my final project in the laboratory, I amassed and integrated all of these tools to develop a high-throughput platform that enables an unbiased, target-independent, non-hypothesis-driven approach to drug discovery. In this dissertation, I describe this platform and demonstrate its power by identifying two drugs that subsequently rescue CCM disease in mice. Finally, I suggest that this platform has potential for the treatment of diseases on a scale that has not previously been accomplished.

As with any scientific endeavor, the data published here are in many cases the result of work by multiple people. In Chapter 1, I describe the use of tropoelastin as a novel coating for intravascular devices. This paper, of which I am co-first author, was written by me. Additionally, I helped to obtain the data in Figure 1.4, and developed a new assay and new software to obtain all the data in Figure 1.5. In Chapter 2, in which we describe the role of the small GTPase ARF6 in vascular stability, I wrote this paper,

and contributed the original data to multiple figures, including Figure 2.1, Figure 2.4, and Supplementary Figures 2.2, 2.5, 2.7, 2.8, and 2. 9. In Chapter 3, I describe the role of ARF6 in mechanotransduction. I obtained all data shown in this chapter, with the exception of data in Figure 3.3, for which I relied on close collaborators who performed some of the final work without me. In Chapter 4, I describe the development of a mouse model for CCM disease. I played a major role in writing this paper, and also obtained or helped to obtain the original data used in Figures 4.2, 4.3, and 4.7, as well as supplemental Figure 4.9. In Chapter 5, I describe the identification of novel treatments for CCM disease. I obtained all of the data used in this paper, with the exception to any western blots, for which I obtained help from my colleagues in the laboratory. This paper has been submitted, but not yet accepted, for publication as of the time of submission of this dissertation.

# CHAPTER 1

## NOVEL APPROACH FOR ENDOTHELIALIZING VASCULAR DEVICES: UNDERSTANDING AND EXPLOITING ELASTIN-ENDOTHELIAL INTERACTIONS

The following chapter was reprinted with permission from the Annals of Biomedical Engineering. I was co-first author of this paper with Brent D. Wilson. In addition, the other authors were Lise K. Sorensen, Margaret Y. Guilhermier, Melissa Clinger, Linda L. Kelley, Yan-Ting E. Shiu, and Dean Y. Li. This article was originally published in the Annals of Biomedical Engineering, 2011 Jan;39(1):337-346. This manuscript details the stabilizing role of elastin, an extracellular matrix component, on the endothelium.

*Annals of Biomedical Engineering*, Vol. 39, No. 1, January 2011 (© 2010) pp. 337–346
DOI: 10.1007/s10439-010-0142-z

# Novel Approach for Endothelializing Vascular Devices: Understanding and Exploiting Elastin–Endothelial Interactions

BRENT D. WILSON,[1,2,3] CHRISTOPHER C. GIBSON,[3,4] LISE K. SORENSEN,[3] MARGARET YOKLAVICH GUILHERMIER,[6] MELISSA CLINGER,[6] LINDA L. KELLEY,[5] YAN-TING E. SHIU,[2,4] and DEAN Y. LI[1,2,3,7]

[1]Division of Cardiology, University of Utah, Salt Lake City, UT 84112, USA; [2]Department of Internal Medicine, University of Utah, Salt Lake City, UT 84112, USA; [3]Program in Molecular Medicine, University of Utah, Salt Lake City, UT 84112, USA; [4]Department of Bioengineering, University of Utah, Salt Lake City, UT 84112, USA; [5]Division of Hematology, University of Utah, Salt Lake City, UT 84112, USA; [6]OrbusNeich Medical, Incorporated, Fort Lauderdale, FL 33309, USA; and [7]Eccles Institute of Human Genetics, University of Utah, Room 4450, 15 North 2030 East, Salt Lake City, UT 84112, USA

*(Received 31 August 2009; accepted 5 August 2010; published online 25 August 2010)*

Associate Editor Peter McHugh oversaw the review of this article.

**Abstract**—Elastin is an essential component of arteries which provides structural integrity and instructs smooth muscle cells to adopt a quiescent state. Despite interaction of endothelial cells with elastin in the internal elastic lamina, the potential for exploiting this interaction therapeutically has not been explored in detail. In this study, we show that tropoelastin (a precursor of elastin) stimulates endothelial cell migration and adhesion more than smooth muscle cells. The biological activity of tropoelastin on endothelial cells is contained in the VGVAPG domain and in the carboxy-terminal 17-amino acids. We show that the effects of the carboxy-terminal 17 amino acids, but not those of VGVAPG, are mediated by integrin $\alpha_V\beta_3$. We demonstrate that tropoelastin covalently linked to stainless steel disks promotes adhesion of endothelial progenitor cells and endothelial cells to the metal surfaces. The adherent cells on the tropoelastin-coated metal surfaces form monolayers that can withstand and respond to arterial shear stress. Because of the unique effects of tropoelastin on endothelial and smooth muscle cells, coating intravascular devices with tropoelastin may stimulate their endothelialization, inhibit smooth muscle hyperplasia, and improve device performance.

**Keywords**—Arteries, Endothelium, Receptors, Stents, Restenosis.

Address correspondence to Dean Y. Li, Eccles Institute of Human Genetics, University of Utah, Room 4450, 15 North 2030 East, Salt Lake City, UT 84112, USA and Yan-Ting E. Shiu, Department of Internal Medicine, University of Utah, Salt Lake City, UT 84112, USA. Electronic mail: y.shiu@utah.edu, dean.li@hmbg.utah.edu

Brent D. Wilson and Christopher C. Gibson have equally contributed to this study.

Dean Y. Li and Yan-Ting Shiu are co-submitting authors of this paper.

## INTRODUCTION

Complications of intracoronary stent placement include thromboembolic events and neointimal hyperplasia due to smooth muscle cell hyperproliferation, leading to in-stent restenosis. The central role of the vascular endothelium in preventing thrombosis and regulating neointimal hyperplasia has led to restenosis prevention strategies that focus on enhancing endothelialiazation.[2,14,17,23] Novel stent coating strategies include delivery of vascular endothelial growth factor (VEGF) (e.g., VEGF-eluting stents[37]) and the use of antibodies that recognize epitopes specific to endothelial cells (e.g., anti-CD34-coated stents[24]). However, these noncytotoxic approaches are still at the investigational stage and their long-term outcome is unknown. Drug-eluting stents currently on the market, in contrast, release cytotoxic drugs to inhibit neointimal hyperplasia at the expense of delaying endothelialization.[25]

Understanding the molecular details of cell–matrix interactions that are involved in the development and maintenance of patent vessels may facilitate the discovery of novel approaches to improve intracoronary stents. This study aimed to better understand elastin–endothelial interactions and explore the potential of elastin as a coating material for intravascular devices. Elastin is a predominant vascular extracellular matrix protein and plays an important structural and signaling role in the development of patent arteries.[32] Elastin is synthesized from soluble tropoelastin which is organized into elastic fibers with contributions from fibrillin microfibrils[30] and glycoproteins such as fibulin-5.[27,34,39] These fibers form concentric elastic

lamellae around vascular lumens, providing the elasticity necessary to absorb and distribute mechanical stress during the cardiac cycle.

Despite the close proximity of endothelial cells to the internal elastic lamina, there have been only a few conflicting studies investigating the molecular details of elastin–endothelial interactions. Coacervated alpha-elastin has been shown to have a dose-dependent effect on porcine aortic endothelial cell proliferation and migration,[18,19] while studies using human umbilical vein endothelial cells reported that adsorbed tropoelastin on plastic promoted cell adhesion but not cell spreading[40] and covalent immobilization of tropoelastin on plasma-treated metal surfaces promoted cell adhesion and proliferation.[41] The variability in elastin effect in these studies may be due to specific domains of tropoelastin and their corresponding endothelial cell surface receptors, which remain to be explored.[10] At least two cell adhesive sites have been identified on tropoelastin: the hexapeptide VGVAPG sequence, which is located in the middle of tropoelastin, and the carboxyl terminus of tropoelastin. Multiple elastin-binding proteins targeting the VGVAPG sequence have been identified and include a 59-kDa protein,[5] a 67-kDa galactoside-binding protein,[15] a 120-kDa protein called elastonectin,[16] and an unidentified $G_i$-linked G protein-coupled receptor (GPCR).[20] The carboxyl terminus of tropoelastin binds to cell surface glycosaminoglycans[7] and the heterodimeric integrin $\alpha_V\beta_3$.[31,34] Detailed studies of elastin–cell interaction studies have focused on vascular smooth muscle cells, fibroblasts, and cancer cells, but not endothelial cells.

In this study, we compared the stimulating effect of recombinant tropoelastin on migration and adhesion of endothelial and smooth muscle cells. We also investigated whether the biological activity of tropoelastin on endothelial cells is contained in the VGVAPG domain and the carboxy-terminal 17-amino acids, as well as determining the type of receptors which bind each of these domains. Finally, we examined endothelial functionality (reaching confluence; adhesion and retention under flow) on metal surfaces coated with covalently immobilized tropoelastin. Our findings suggest that tropoelastin coating is a promising approach for enhancing endothelialization of intravascular device.

## MATERIALS AND METHODS

### *Materials*

A 48-well Boyden chamber apparatus and 8 $\mu$m-pore polycarbonate membranes for migration experiments were from NeuroProbe (Cabin John, MD, USA). Type I collagen (CN) and fibronectin (FN) were from Biomedical Technologies (Stoughton, MA, USA). Monoclonal anti-integrin antibodies [mouse anti-human $\alpha_V\beta_3$ (clone LM109) and mouse-anti-human $\alpha_2\beta_1$ (clone BHA2.1)] were from Chemicon International (Temecula, CA, USA). Purified whole mouse IgG was purchased from Jackson ImmunoResearch Laboratories (West Grove, PA, USA). Oregon Green 488-conjugated phalloidin and DAPI nuclear counterstain were purchased from Molecular Probes/Invitrogen (Carlsbad, CA, USA) and Vector Labs (Burlingame, CA, USA), respectively. Bovine serum albumin (BSA) and acetylated 1% gelatin from porcine skin was purchased from Sigma (St. Louis, MO, USA). Other chemical reagents and cell culture ware/reagents were purchased from Fisher Scientific (Pittsburgh, PA, USA) and Lonza (Walkersville, MD, USA), respectively, unless otherwise mentioned.

### *Recombinant Human Tropoelastin and Synthesized Elastin Peptides*

The endogenous signal sequence of human tropoelastin (tELN) was removed and replaced with a 10×-histidine tag. This cDNA was cloned into an isopropyl-$\beta$-D-thiogalactoside (IPTG)-inducible construct using the pET System and then expressed in the *Escherichia coli* host strain Rosetta-2 (DE3) pLysS (Novagen/EMD Biosciences, San Diego, CA, USA). LB growth media containing 50 $\mu$g/mL ampicillin and 34 $\mu$g/mL chloramphenicol were inoculated with Rosetta-2 (DE3) pLysS bacteria containing the recombinant tropoelastin plasmid, and the culture was grown at 37 °C until OD at 600 nm = 0.4–0.6. Induction was accomplished by adding IPTG to a final concentration of 1 mM. The culture was incubated at 37 °C for 4 h. The bacterial pellet was harvested by compounding centrifugation and weighed. The pellet was processed in Bugbuster HT + lysozyme (Novagen), and inclusion bodies were purified according to Novagen's protocol. Following the last wash, the inclusion bodies were pelleted and dissolved overnight at 4 °C in 1× Bind Buffer (500 mM NaCl, 20 mM Tris–HCl, 5 mM imidazole) containing 6 M urea, pH 7.9. Insoluble material was then removed by centrifugation. The supernatant was filtered through a 0.45-$\mu$m syringe filter. The sample was then added to His–Mag beads (Novagen) that had been pre-equilibrated to 1× Bind Buffer with 6 M urea. Beads were collected using a Magnatight stand (Novagen) and washed four times with wash buffer (500 mM NaCl, 60 mM imidazole, 20 mM Tris–HCl) containing 6 M urea, pH 7.9. The recombinant tELN protein was eluted from the beads with 500 mM imidazole, 500 mM NaCl, 20 mM

Tris–HCl, 6 M urea, pH 7.9. The sample was dialyzed against HBSS using Slide-A-Lyzer Dialysis Cassettes with 10,000 MWCO (Pierce). Purified protein was analyzed by SDS-PAGE analysis by standard techniques and stored at −80 °C. Elastin-derived peptides [VGVAPG and 1FPGGACLGKACGRKRK (Cterm peptide)] were synthesized at the DNA/Peptide Facility, University of Utah.

### *CD34+ Cell Purification*

Human CD34+ cells were purified from a peripheral blood mononuclear cell preparation collected by an apheresis procedure. The donor was mobilized with 10 μg/kg granulocyte colony-stimulating factor for 4 days prior to the collection procedure, as approved by the Institutional Review Board of the University of Utah. Purification of CD34+ cells was accomplished in a closed and sterile system using an automated cell selection device, CliniMACS (Miltenyi Biotec, Auburn, CA, USA), following manufacturer's instructions. 98% CD34+ cells were obtained by flow cytometry using a FACScan analyzer (Becton–Dickinson, San Jose, CA, USA) and ISHAGE protocol.[36]

### *Endothelial Cells, Routine Cell Culture, and Preparation for Experiments*

Human aortic endothelial cells (HAEC), human coronary artery endothelial cells (HCAEC), human microvascular endothelial cells (HMVEC), and human aortic smooth muscle cells (HASMC) were purchased from Lonza and cultured according to manufacturer's specifications in Endothelial Growth Medium-2 (HAEC), Endothelial Growth Medium-2MV (HCAEC, HMVEC), or Smooth Muscle Growth Medium-2 (HASMC). Low passage cells (2–7) were used in all experiments. Sixteen hours prior to experiments, cultures were serum-starved using basal medium [Endothelial Basal Medium-2 (EBM-2) for EC; Smooth Muscle Basal Medium-2 (SmBM-2) for SMC] and 0.5% fetal calf serum.

### *Migration Assays*

Migration assays were performed as described.[3,28,35] In brief, HAEC were lifted, diluted in buffer (0.5% BSA in EBM-2) to $1.5 \times 10^6$ cells/mL, and recovered in suspension at 37 °C and 5% $CO_2$ for 1 h. For inhibition assays, 25 μg/mL anti-$\alpha_V\beta_3$ antibodies or control IgG were added to the cell suspension during the recovery period. All migration assays were performed in the 48-well Boyden chamber apparatus. 30 μL of recovered cells ($4.5 \times 10^4$ cells total) was added to the bottom chambers, and the wells were overlayed with an 8 μm-pore polycarbonate membrane coated with 1% acetylated gelatin. The apparatus was assembled and inverted for a 2-h period at 37 °C and 5% $CO_2$. The apparatus was then re-inverted, and 52 μL of 0.1% BSA in DMEM (diluent, random migration control) or chemoattractants [10 ng/mL fibronectin (positive control), 10–200 ng/mL tropoelastin, 10 μM VGVAPG, and 10 μM 1FPGGAC LGKACGRKRK Cterm peptide] were added to the upper chambers. Migration was allowed to proceed for 2 h at 37 °C and 5% $CO_2$ in an incubator. Membranes were then removed, fixed in methanol, and stained with Hema 3. Non-migrated cells were removed from the membrane with a moistened swab, and membranes were mounted migrated-side down on glass slides. The number of cells migrating through the membrane per high power field (HPF) on a Zeiss Axiovert 200 inverted microscope equipped with a Zeiss Axiocam digital camera was recorded. Two HPFs were observed for each well and averaged for each independent sextuplicate-well set. Final results were expressed as the average number of cells per HPF from three or more independent experiments.

### *Adhesion Assays on 96-Well Plates*

Adhesion assays were performed as described[8,22] with minor modifications. 96-well plates were coated overnight at 4 °C with 10 μg/mL collagen type I, fibronectin, tropoelastin, or 0.1% BSA, and then blocked for 1 h at 25 °C in 5% BSA. HAEC were lifted from T-75 flasks, diluted in buffer (0.5% BSA in EBM-2), and recovered in suspension at working density ($5 \times 10^5$ cells/mL) at 37 °C and 5% $CO_2$ in an incubator for 1 h. For inhibition assays, 25 μg/mL anti-$\alpha_2\beta_1$ antibodies, anti-$\alpha_V\beta_3$ antibodies, or control IgG were added to the cell suspension during the recovery period. 100 μL of recovered cells ($5 \times 10^4$ cells total) was added to the coated wells, and adhesion was allowed to proceed for 30 min at 37 °C and 5% $CO_2$ in an incubator. Following this incubation, the plates were inverted and washed twice with phosphate buffered saline (PBS) to remove non-adherent cells. Wells were then fixed in Zamboni fixative, stained with Gill 1 hematoxylin, overlayed with 80% glycerol, and imaged at 100× magnification on a Zeiss inverted microscope. The number of adherent cells was averaged for two wells (duplicate) in each independent experiment. Final results were expressed as the average number of cells per well from three or more independent experiments.

### *Adhesion Assays on Stainless Steel Disks*

Adhesion assays using unmodified 6 mm stainless steel disks or disks modified with anti-CD34 antibody,

tropoelastin, or polysaccharide base matrix as vehicle control (provided by OrbusNeich Medical, Fort Lauderdale, FL, USA) were performed as described above with the following modifications: 48-well plates were used, and twice the number/volume of cells ($10^5$ cells in 200 $\mu$L) was added to each well. Adhesion was allowed to proceed for 30 min at 37 °C and 5% $CO_2$. Post-adhesion, the wells were washed in PBS, fixed in 4% neutral buffered formalin, permeabilized in 0.5% Triton X-100 (PBS), blocked in 5% non-fat milk (PBS), and stained for actin fibers with Oregon Green 488-conjugated phalloidin. Disks were mounted on modified microscope slides with Vectashield mounting medium + DAPI (Vector Labs) and imaged using a Zeiss fluorescent microscope. The numbers of adherent cells were counted and final results were expressed as the average number of cells per disk.

### *Spinning Disk Adhesion Strength Assay*

22-mm round glass coverslips were coated with tELN, FN, anti-CD34 antibodies (Santa Cruz), or BSA for 2 h at room temperature in 6-well plates. 3 mL of $5 \times 10^4$ HAEC/mL in EGM2 was then added to each well and cells were allowed to adhere for 6 h at 37 °C and 5% $CO_2$. After 6 h, coverslips were inverted and submerged in HEPES-BSS on a custom holder at 37 °C and spun at 2100 RPM for 5 min as previously described.[12] After 5 min, coverslips were removed and immediately fixed and mounted on slides with Vectashield mounting medium + DAPI and imaged using a BD Pathway 855 microscope. The number of cells/HPF at various distances from the center of the coverslip was counted and expressed as the percentage of cells remaining compared to the center of the disk and normalized to static controls. The shear stress at each measurement location was calculated as described.[12]

### *Fluid Shear Stress Assays*

HAEC were seeded onto 6-mm tropoelastin-coated stainless steel disks or controls (6 mm silicone disks coated with fibronectin) in 48-well plates as described above. Cells were allowed to grow to confluence on the disks for 48 h prior to subjection to flow. The disks were placed in flow chambers and exposed to 24 h of laminar arterial flow of 16 dyn/cm$^2$ or static conditions utilizing a recirculating flow system.[11,33] The disks were fixed and stained for actin using phalloidin as previously described, then mounted with Vectashield mounting medium with DAPI and imaged. Images were processed for actin alignment using a custom Matlab program based on previously described image-processing methods.[42]

### *Data Presentation and Statistical Analysis*

Bar graphs represent the average of three or more independent experiments. Vertical error bars on data points represent the standard error of the mean. The Student *t*-test and analysis of variance were used to determine the significance of differences between two conditions and between more than two conditions, respectively. *p*-Value less than 0.05 was considered statistically significant.

## RESULTS

### *Tropoelastin Stimulates Endothelial Cell Migration*

The entire length of tropoelastin is well conserved among human, bovine, and murine proteins with 82.4% similarity across the length of the entire protein (Supplementary Fig. 1). Purified recombinant tropoelastin has a molecular weight of ~65 kDa and is free from significant contaminating proteins (Supplementary Fig. 2). Using a Boyden chamber apparatus, we performed migration assays with HAEC and various concentrations of full-length recombinant tropoelastin. Compared to the BSA control, there was a significant increase (4.5-fold) in endothelial migration using tropoelastin doses as low as 10 ng/mL (Fig. 1a). At 200 ng/mL there was an eightfold increase that was comparable to the effect of 10 ng/mL VEGF. In order to differentiate chemokinesis versus chemotaxis, we also performed the experiment using equivalent tropoelastin concentrations in the upper and lower Boyden chambers and observed no increased migration compared to control, suggesting chemotaxis rather than chemokinesis (data not shown). Similar results were seen with other endothelial cell types, including HMVEC and HCAEC (data not shown).

### *VGVAPG and the Carboxy Terminus of Tropoelastin Stimulate Endothelial Migration Through Different Mechanisms*

We next compared the effect of another known endothelial chemotaxis stimulant, fibronectin, with the effect of full-length recombinant tropoelastin and the elastin fragments VGVAPG and the Cterm peptide. Because the carboxy terminus of elastin has been shown to bind the integrin $\alpha_V\beta_3$ in solid-phase assays[31] and recently in fibroblasts,[4] we also investigated the involvement of $\alpha_V\beta_3$ in this study using the $\alpha_V\beta_3$ blocking antibody LM609. The isotype-matched control antibody IgG increased the baseline endothelial transwell-migration by twofold, perhaps by blocking the non-specific binding sites between the cells and the transwell membrane.[29] In the presence of IgG, each chemotaxis

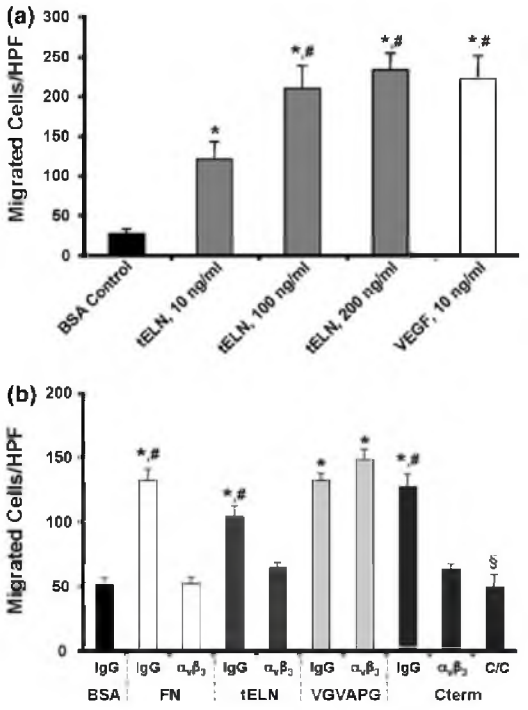


FIGURE 1. Soluble recombinant tropoelastin stimulates migration of HAEC through different mechanisms. (a) HAEC migration toward 0.1% BSA, 10 ng/mL VEGF, or 10–200 ng/mL tELN for 2 h in a 48-well Boyden chamber apparatus. * $p < 0.05$ when compared to the BSA control; # $p < 0.05$ when compared to 10 ng/mL tELN. (b) HAEC pretreated with either nonspecific IgG or anti-$\alpha_V\beta_3$ antibodies were allowed to migrate toward 0.1% BSA, 10 ng/mL FN, 10 ng/mL tELN, 10 $\mu$M VGVAPG, or 10 $\mu$M IFPGGACLGKACGRKRK (Cterm) for 2 h. Migration with the Cterm peptide in the upper and lower chambers of the Boyden apparatus (C/C, last bar) was carried out to differentiate between chemokinesis and chemotaxis. * $p < 0.05$ when compared to the BSA-IgG control; # $p < 0.05$ when compared to respective anti-$\alpha_V\beta_3$ treated samples; § $p < 0.05$ when compared to Cterm-IgG.

stimulants caused a 2 to 2.5-fold increase in endothelial migration when compared to the BSA control (Fig. 1b). The anti-$\alpha_V\beta_3$ antibody almost completely inhibited the stimulating effect of fibronectin, full-length tropoelastin, and the Cterm peptide, as would be expected for processes that involve signaling through $\alpha_V\beta_3$. However, endothelial migration to VGVAPG (which may be mediated by an unknown GPCR[21]) was not affected by the anti-$\alpha_V\beta_3$ antibody. When the Cterm peptide was added to the upper and lower Boyden chambers (Fig. 1b, last bar), there was no increased migration, indicating that this peptide promotes chemotaxis. The anti-$\alpha_V\beta_3$ antibody had the same effect on tropoelastin and the Cterm peptide, suggesting that Cterm is sufficient for recapitulating the migratory response of endothelial cells to tropoelastin.

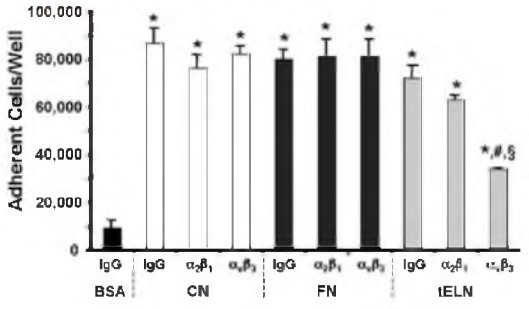


FIGURE 2. Adhesion of HAEC to recombinant tropoelastin-coated plastic surface is mediated by $\alpha_V\beta_3$. Adhesion experiments were carried out using 96-well plates pretreated with 0.1% BSA, 10 $\mu$g/mL collagen (CN), 10 $\mu$g/mL fibronectin (FN), or 10 $\mu$g/mL tELN. HAEC in suspension were pretreated with anti-$\alpha_2\beta_1$ or $\alpha_V\beta_3$ antibodies or non-specific IgG before being allowed to adhere to the protein-coated surfaces for 30 min. * $p < 0.05$ when compared to the BSA-IgG control; # $p < 0.05$ when compared to tELN-IgG; § $p < 0.05$ when compared to tELN-$\alpha_2\beta_1$.

### *Tropoelastin Promotes Endothelial Cell Adhesion Through $\alpha_V\beta_3$*

The adhesion of HAEC to wells pre-coated with 0.1% BSA or with 10 $\mu$g/mL collagen (also an integrin-binding protein), fibronectin, or tropoelastin is quantified and shown in Fig. 2. To determine the involvement of integrin in cell adhesion, HAEC were incubated with either IgG control or anti-$\alpha_2\beta_1$ or anti-$\alpha_V\beta_3$ blocking antibodies prior to being exposed to the coated surfaces. In the presence of the IgG antibody, tropoelastin coating resulted in an approximately eightfold increase in endothelial adhesion compared to BSA coating; this amount of increased endothelial adhesion is similar in magnitude to the effect of collagen or fibronectin coating. Preincubation with anti-$\alpha_2\beta_1$ or anti-$\alpha_V\beta_3$ antibodies did not significantly decrease HAEC adhesion to fibronectin or collagen. This is likely explained by the fact that endothelial cells express multiple integrins that bind collagen or fibronectin.[29] However, endothelial adhesion to tropoelastin was blocked by more than 50% by the anti-$\alpha_V\beta_3$ blocking antibody. This suggests that binding of tropoelastin to the integrin $\alpha_V\beta_3$ is the predominant mechanism for endothelial adhesion to tropoelastin-coated surfaces.

### *Tropoelastin Promotes Adhesion and Migration of Endothelial and Smooth Muscle Cells to Different Degrees*

Tropoelastin promotes the migration and spreading of mouse aortic smooth muscle cells through a

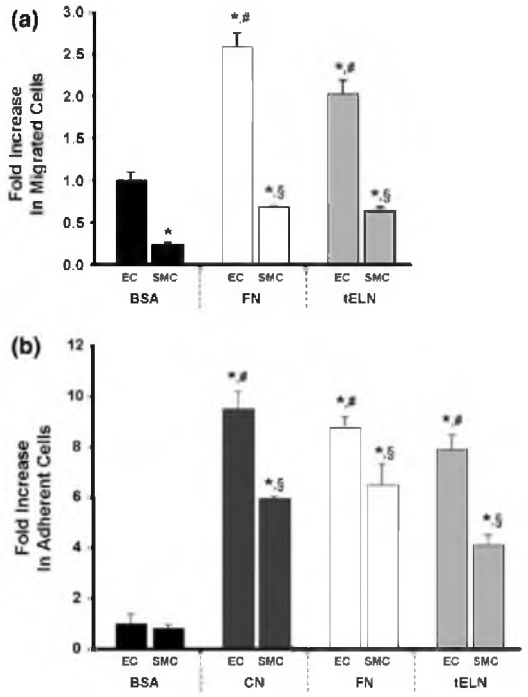


**FIGURE 3.** Effects of recombinant tropoelastin on stimulating migration and adhesion of HAEC and HASMC. (a) HAEC and HASMC were allowed to migrate toward 0.1% BSA, 10 ng/mL FN, or 10 ng/mL tELN for 2 h in a Boyden chamber apparatus. The number of migrated cells was normalized to the 0.1% BSA-EC control. * $p < 0.05$ when compared to the BSA-EC control; # $p < 0.05$ when compared to respective SMC samples; § $p < 0.05$ when compared to the BSA-SMC samples. (b) Adhesion experiments were carried out using 96-well plates that were pretreated with 0.1% BSA, 10 $\mu$g/mL CN, 10 $\mu$g/mL FN, or 10 $\mu$g/mL tELN overnight. HAEC and HASMC in suspension were allowed to adhere to the protein-coated surfaces for 30 min. The number of adherent cells was normalized to the 0.1% BSA-EC control. * $p < 0.05$ when compared to the BSA-EC control; # $p < 0.05$ when compared to respective SMC samples; § $p < 0.05$ when compared to the BSA-SMC samples.

non-integrin, G-protein-coupled signaling pathway.[20] In this study, we were interested in direct comparison of the stimulating effect of tropoelastin on the migration and adhesion of HAEC and HASMC. As shown in Fig. 3a, the baseline motility of HAEC is fivefold higher than that of HASMC. Both fibronectin and tropoelastin increased the motility of HAEC and HASMC, but the motility of HAEC remained significantly higher than HASMC. As shown in Fig. 3b, the baseline adhesion of HAEC was comparable to that of HASMC. While collagen, fibronectin, and tropoelastin promoted the adhesion of both cell types, their stimulating effects for HAEC were significantly stronger than for HASMC.

### *Tropoelastin Covalently Linked to Stainless Steel Promotes Adhesion and Spreading of Endothelial Cells*

The above results suggest that soluble tropoelastin promotes HAEC migration and that tropoelastin coating of plastic surfaces by adsorption promotes HAEC adhesion to those surfaces. *In vivo* endothelialization of intravascular devices presumably occurs through adhesion of circulating endothelial cells and/or their progenitors, and through invasion of endothelial cells from the borders of the coated surface and/or from the vasa vasorum.[9] To examine the effects of tropoelastin on adhesion and spreading of endothelial cells on stainless steel, tropoelastin was covalently immobilized to 6-mm diameter stainless steel disks (Fig. 4a) that were pre-treated with a stable polysaccharide base matrix (Ssens BV, Hengelo, The Netherlands). Other disks were coated with anti-CD34 antibodies or with polysaccharide vehicle alone. Coronary stents coated with immobilized anti-CD34 antibodies (Genous Bio-engineered R stent™) accelerate endothelialization by promoting the capture of circulating endothelial cells and endothelial progenitor cells.[1] Adhesion experiments using human CD34+ endothelial progenitor cells, HAEC, and HMVEC (Fig. 4b) demonstrated a greater than ninefold increase in endothelial adhesion to disks coated with anti-CD34 antibodies or tropoelastin over the vehicle control. Additionally, the tropoelastin coating increased the number of adherent HAEC and HMVEC, but not CD34+ cells, compared to the CD34 antibody-coated disks.

We next examined cell spreading on the coated metal surfaces by staining adherent cells with phalloidin to highlight the actin cytoskeleton and DAPI to mark cell nuclei. Both CD34-antibody and tropoelastin coating enhanced the adhesion of human CD34+ cells and HAEC to the metal disks, though these cells did not spread well on either coating within 30 min of adhesion (Fig. 4c, left and middle panels). In contrast, HMVEC adherent to tropoelastin-coated metal disks were well spread and demonstrated an organized actin cytoskeleton within 30 min of adhesion (Fig. 4c, lower right panel). HAEC formed confluent monolayers on tropoelastin-coated metal disks when allowed to adhere for hours rather than minutes (Fig. 5b, left panel). Overall, these studies demonstrate that modifying foreign surfaces with tropoelastin may stimulate endothelial spreading in addition to adhesion.

### *Cells Remain Adherent to Tropoelastin-Coated Surfaces Under Fluid Shear Stress*

Intravascular devices modified with tropoelastin would be exposed to physiological fluid shearing forces.

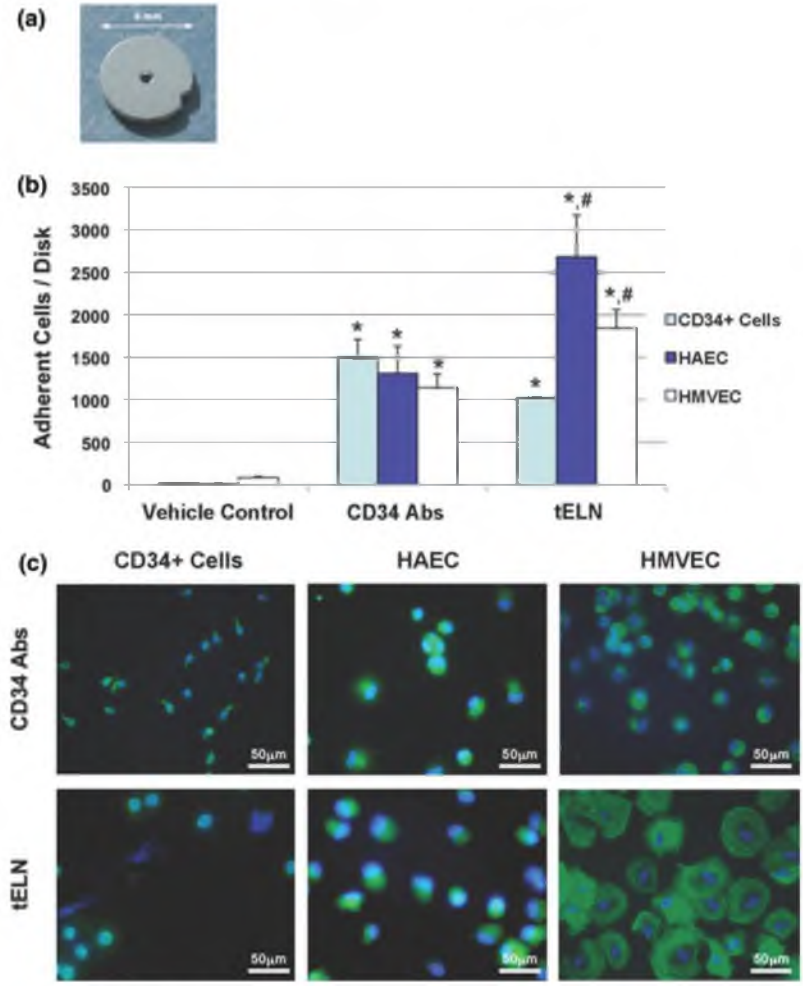


**FIGURE 4. Adhesion of endothelial cells and CD34+ endothelial progenitor cells to stainless steel disks modified with anti-CD34 antibodies or tropoelastin. (a) 6-mm stainless steel disks were modified with base polysaccharide (vehicle control), anti-CD34 antibodies (CD34 Abs), or tELN. (b) CD34+ endothelial progenitor cells (CD34+ Cells), HAEC, and HMVEC were allowed to adhere to disks for 30 min. * $p<0.05$ when compared to the vehicle controls regardless of cell types; # $p<0.05$ when compared to the corresponding cell type on CD34 Abs-coated disks. (c) CD34+ cells, HAEC, and HMVEC adherent on modified disks were stained with phalloidin (green) and DAPI (blue). Each panel depicts a representative fluorescent microscopic image.**

To assess whether cells attaching to tropoelastin-modified surfaces would persist through such conditions, the effects of shear stress were examined. A majority of HAEC seeded onto tropoelastin-coated coverslips remained adhered through short (5 min) exposures to shear stresses up to 250 dyne/cm$^2$ (Fig. 5a). Our data show that all four types of coating (tropoelastin, fibronectin, BSA, and anti-CD34 antibodies) resulted in similar cell retention when shear stress was 150 dyn/cm$^2$ or lower. At higher shear stress, however, cell retention on tropoelastin and fibronectin was higher than on BSA and anti-CD34 antibodies. In particular, cell retention on tropoelastin was twofold higher than on anti-CD34 antibodies at the largest shear stress tested (250 dyn/cm$^2$). These data suggest that tropoelastin coating may provide superior cell retention to anti-CD34 antibody coating in high shear stress conditions, as might be expected in and around the complex architecture of an intravascular device.[26] HAEC seeded onto covalently modified stainless steel disks and exposed to arterial shear stresses (16 dyne/cm$^2$) showed continued adhesion after 24 h of flow (Fig. 5b, right panel). Further, HAEC actin filaments were more ordered and tended

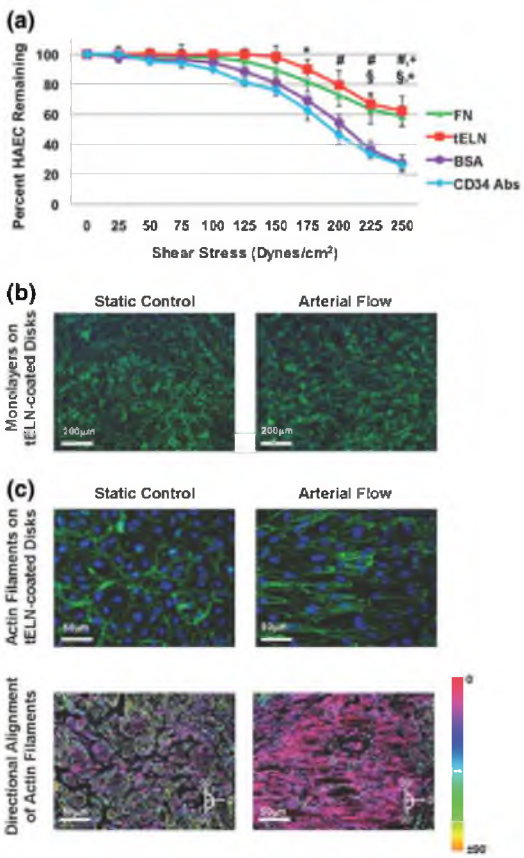


**FIGURE 5.** Adherence of endothelial cells to coated surfaces under conditions of flow. (a) HAEC adhered to FN, tELN, BSA, or anti-CD34 antibodies (CD34 Abs) coated coverslips were exposed to shear stress. $^{+}$ $p < 0.05$ when comparing FN and BSA coatings; $^{\S}$ $p < 0.05$ when comparing tELN and BSA coatings; $^{\#}$ $p < 0.05$ when comparing FN and anti-CD34 Abs coatings; $^{*}$ $p < 0.05$ when comparing tELN and anti-CD34 Abs coatings. (b) HAEC grown on tELN-coated disks were stained with phalloidin (green) and DAPI (blue). Each panel depicts a representative fluorescent microscopic image. (c) Upper panels: Each panel depicts a representative HPF fluorescent microscopic image of actin cytoskeleton (green) and nuclei (blue). Lower panels: The directional alignment of actin fibers is shown using a ColorMap to represent the local angle of each fiber. Cells under arterial flow show an ordered and aligned cytoskeleton, as demonstrated by more uniform fiber coloration (higher levels of blue and purple). In contrast, cells under static conditions show similar levels of all colors, indicating random alignment.

to align unidirectionally under arterial flow, as compared to the random alignment of the static samples (Fig. 5c). The same effect was observed in the HAEC monolayers on fibronectin-coated silicone disks (data not shown). This suggests that cells that attach to tropoelastin-coated intravascular devices remodel in response to flow, in addition to withstanding physiological flow conditions.

## DISCUSSION

Here, we propose a biomimetic approach for enhancing endothelial recovery: mimic the internal elastic lamina by coating intravascular devices with tropoelastin. This approach capitalizes on the biological properties of tropoelastin and does not require faithfully recreating the complex physical properties of elastic fibers. Thus, the need for protein production in mammalian expression systems or the use of elastic fibers extracted from animals is avoided.

We confirm that the biological activity of tropoelastin on endothelial cells is contained in the VGVAPG domain and the carboxy-terminal 17-amino acids, and we provide evidence that the activity of the carboxy terminus is mediated via $\alpha_V\beta_3$ and appears distinct from the effect of the hexapeptide VGVAPG. We demonstrate that recombinant tropoelastin stimulates endothelial cell migration and adhesion, and the effect is stronger for endothelial cells than smooth muscle cells. Further, we show that tropoelastin coatings on metal surfaces (by covalent immobilization) enhances adhesion of endothelial progenitor cells and several endothelial cell types to the metal surfaces, and that endothelial cells can form confluent monolayers on the metal surface which resist and respond to arterial shear stresses. It is possible that the alignment of endothelial cells on tropoelastin may be mediated by $\alpha_V\beta_3$, which has been shown to mediate the effect of shear stress on endothelial cytoskeleton reorganization on fibronectin.[13,38]

Tropoelastin has several potential advantages when compared to two other novel intravascular device coatings, VEGF and anti-CD34 antibodies. The endothelial chemotaxis stimulating effect of tropoelastin at 1.5 nM was comparable to the effect of VEGF at 0.5 nM. Thus, tropoelastin is similarly effective in attracting endothelial cells but does not have the potent vascular permeability enhancing effects of VEGF which result in several well-documented adverse effects.[6] We also show that tropoelastin, while not as specific as anti-CD34 antibodies in its adhesive effects, has a strong pro-adhesive effect on endothelial cells, and preferentially promotes the adhesion of endothelial cells over non-endothelial cell types. Additionally, we show that the endothelial cells adherent to tropoelastin spread their cytoplasm and intracellular actin network to a greater degree than on anti-CD34 antibodies, as they might after adhesion to an intact internal elastic lamina *in vivo*. Cell spreading is critical as it is required for the effective coverage of the foreign surface and for the cells to withstand fluid shearing forces. Thus, a potential advantage of tropoelastin coating is enhanced cell spreading, which is not expected or observed in strategies that aim to

capture endothelial cells using antibodies to cell surface markers. Indeed, our data show that cell retention under high fluid shear stress is better on tropoelastin than on anti-CD34 antibody-coated surfaces.

Stainless steel is a very common material in the construction of intravascular devices, and therefore is the focus of this study. It should be noted, however, that our experiments also included tissue culture plastic surfaces and silicone sheets, and tropoelastin performed similar to the results we described on stainless steel, suggesting that tropoelastin coating could be applicable as an intravascular device coating on any number of other device materials in use now or in the future. This study suggests that tropoelastin coating is a promising approach for enhancing endothelialization of intravascular device, but further exploration is needed to determine the promise and practicality of accelerating endothelialization by immobilizing tropoelastin to the surfaces of vascular devices either alone or in combination with other drug eluting or coating strategies.

## ELECTRONIC SUPPLEMENTARY MATERIAL

The online version of this article (doi:10.1007/s10439-010-0142-z) contains supplementary material, which is available to authorized users.

## ACKNOWLEDGMENTS

B.D.W. was supported by an American College of Cardiology Foundation/Pfizer Fellow in Cardiovascular Medicine. C.C.G is supported by a grant from the NHLBI. M.Y. and M.C. are the employees of OrbusNeich Medical, Incorporated. L.L.K. is supported by grants from the NIH. Y.E.S. is supported by grants from the NIH and American Heart Association. D.Y.L is funded by grants from the OrbusNeich, NHLBI, Juvenile Diabetes Research Foundation, HA, and Edna Benning Foundation, National Center for Research Resources Public Health Services Research Grant UL1-RR025764, and the Department of Defense. D.Y.L. is a Burroughs Wellcome Foundation Clinical Scientist in Translational Research and an Established Investigator of the American Heart Association.

## REFERENCES

[1]Aoki, J., P. W. Serruys, H. van Beusekom, A. T. Ong, E. P. McFadden, G. Sianos, W. J. van der Giessen, E. Regar, P. J. de Feyter, H. R. Davis, S. Rowland, and M. J. Kutryk. Endothelial progenitor cell capture by stents coated with antibody against CD34: the HEALING-FIM (Healthy Endothelial Accelerated Lining Inhibits Neointimal Growth-First In Man) Registry. *J. Am. Coll. Cardiol.* 45:1574–1579, 2005.

[2]Asai, J., H. Takenaka, K. F. Kusano, M. Ii, C. Luedemann, C. Curry, E. Eaton, A. Iwakura, Y. Tsutsumi, H. Hamada, S. Kishimoto, T. Thorne, R. Kishore, and D. W. Losordo. Topical sonic hedgehog gene therapy accelerates wound healing in diabetes by enhancing endothelial progenitor cell-mediated microvascular remodeling. *Circulation* 113:2413–2424, 2006.

[3]Aznavoorian, S., M. L. Stracke, J. Parsons, J. McClanahan, and L. A. Liotta. Integrin alphavbeta3 mediates chemotactic and haptotactic motility in human melanoma cells through different signaling pathways. *J. Biol. Chem.* 271:3247–3254, 1996.

[4]Bax, D. V., U. R. Rodgers, M. M. Bilek, and A. S. Weiss. Cell adhesion to tropoelastin is mediated via the C-terminal GRKRK motif and integrin alphaVbeta3. *J. Biol. Chem.* 284:2816–2823, 2009.

[5]Blood, C. H., J. Sasse, P. Brodt, and B. R. Zetter. Identification of a tumor cell receptor for VGVAPG, an elastin-derived chemotactic peptide. *J. Cell. Biol.* 107:1987–1993, 1988.

[6]Bose, D., F. Meric-Bernstam, W. Hofstetter, D. A. Reardon, K. T. Flaherty, and L. M. Ellis. Vascular endothelial growth factor targeted therapy in the perioperative setting: implications for patient care. *Lancet Oncol.* 11:373–382, 2010.

[7]Broekelmann, T. J., B. A. Kozel, H. Ishibashi, C. C. Werneck, F. W. Keeley, L. Zhang, and R. P. Mecham. Tropoelastin interacts with cell-surface glycosaminoglycans via its COOH-terminal domain. *J. Biol. Chem.* 280:40939–40947, 2005.

[8]Cheresh, D. A., and R. C. Spiro. Biosynthetic and functional properties of an Arg-Gly-Asp-directed receptor involved in human melanoma cell attachment to vitronectin, fibrinogen, and von Willebrand factor. *J. Biol. Chem.* 262:17703–17711, 1987.

[9]Conway, E. M., D. Collen, and P. Carmeliet. Molecular mechanisms of blood vessel growth. *Cardiovasc. Res.* 49:507–521, 2001.

[10]Daamen, W. F., J. H. Veerkamp, J. C. van Hest, and T. H. van Kuppevelt. Elastin as a biomaterial for tissue engineering. *Biomaterials* 28:4378–4398, 2007.

[11]Frangos, J. A., S. G. Eskin, L. V. McIntire, and C. L. Ives. Flow effects on prostacyclin production by cultured human endothelial cells. *Science* 227:1477–1479, 1985.

[12]Gallant, N. D., and A. J. Garcia. Quantitative analyses of cell adhesion strength. *Methods Mol. Biol.* 370:83–96, 2007.

[13]Girard, P. R., and R. M. Nerem. Shear stress modulates endothelial cell morphology and F-actin organization through the regulation of focal adhesion-associated proteins. *J. Cell. Physiol.* 163:179–193, 1995.

[14]Hedman, M., J. Hartikainen, M. Syvanne, J. Stjernvall, A. Hedman, A. Kivela, E. Vanninen, H. Mussalo, E. Kauppila, S. Simula, O. Narvanen, A. Rantala, K. Peuhkurinen, M. S. Nieminen, M. Laakso, and S. Yla-Herttuala. Safety and feasibility of catheter-based local intracoronary vascular endothelial growth factor gene transfer in the prevention of postangioplasty and in-stent restenosis and in the treatment of chronic myocardial ischemia: phase II results of the Kuopio Angiogenesis Trial (KAT). *Circulation* 107:2677–2683, 2003.

[15]Hinek, A., D. S. Wrenn, R. P. Mecham, and S. H. Barondes. The elastin receptor: a galactoside-binding protein. *Science* 239:1539–1541, 1988.

[16]Hornebeck, W., J. M. Tixier, and L. Robert. Inducible adhesion of mesenchymal cells to elastic fibers: elastonectin. *Proc. Natl Acad. Sci. USA* 83:5517–5520, 1986.

[17]Ii, M., H. Nishimura, A. Iwakura, A. Wecker, E. Eaton, T. Asahara, and D. W. Losordo. Endothelial progenitor cells are rapidly recruited to myocardium and mediate protective effect of ischemic preconditioning via "imported" nitric oxide synthase activity. *Circulation* 111:1114–1120, 2005.

[18]Ito, S., S. Ishimaru, and S. E. Wilson. Application of coacervated alpha-elastin to arterial prostheses for inhibition of anastomotic intimal hyperplasia. *ASAIO J.* 44:M501–M505, 1998.

[19]Ito, S., S. Ishimaru, and S. E. Wilson. Effect of coacervated alpha-elastin on proliferation of vascular smooth muscle and endothelial cells. *Angiology* 49:289–297, 1998.

[20]Karnik, S. K., B. S. Brooke, A. Bayes-Genis, L. Sorensen, J. D. Wythe, R. S. Schwartz, M. T. Keating, and D. Y. Li. A critical role for elastin signaling in vascular morphogenesis and disease. *Development* 130:411–423, 2003.

[21]Karnik, S. K., J. D. Wythe, L. Sorensen, B. S. Brooke, L. D. Urness, and D. Y. Li. Elastin induces myofibrillogenesis via a specific domain, VGVAPG. *Matrix Biol.* 22:409–425, 2003.

[22]Kikkawa, Y., N. Sanzen, H. Fujiwara, A. Sonnenberg, and K. Sekiguchi. Integrin binding specificity of laminin-10/11: laminin-10/11 are recognized by alpha 3 beta 1, alpha 6 beta 1 and alpha 6 beta 4 integrins. *J. Cell Sci.* 113(Pt 5): 869–876, 2000.

[23]Kipshidze, N., G. Dangas, M. Tsapenko, J. Moses, M. B. Leon, M. Kutryk, and P. Serruys. Role of the endothelium in modulating neointimal formation: vasculoprotective approaches to attenuate restenosis after percutaneous coronary interventions. *J. Am. Coll. Cardiol.* 44:733–739, 2004.

[24]Klomp, M., M. A. Beijk, and R. J. de Winter. Genous endothelial progenitor cell-capturing stent system: a novel stent technology. *Expert Rev. Med. Dev.* 6:365–375, 2009.

[25]McFadden, E. P., E. Stabile, E. Regar, E. Cheneau, A. T. Ong, T. Kinnaird, W. O. Suddath, N. J. Weissman, R. Torguson, K. M. Kent, A. D. Pichard, L. F. Satler, R. Waksman, and P. W. Serruys. Late thrombosis in drug-eluting coronary stents after discontinuation of antiplatelet therapy. *Lancet* 364:1519–1521, 2004.

[26]Mejia, J., B. Ruzzeh, R. Mongrain, R. Leask, and O. F. Bertrand. Evaluation of the effect of stent strut profile on shear stress distribution using statistical moments. *Biomed. Eng. Online* 8:8, 2009.

[27]Nonaka, R., S. Onoue, H. Wachi, F. Sato, Z. Urban, B. C. Starcher, and Y. Seyama. DANCE/fibulin-5 promotes elastic fiber formation in a tropoelastin isoform-dependent manner. *Clin. Biochem.* 42:713–721, 2009.

[28]Park, C. C., J. C. Morel, M. A. Amin, M. A. Connors, L. A. Harlow, and A. E. Koch. Evidence of IL-18 as a novel angiogenic mediator. *J. Immunol.* 167:1644–1653, 2001.

[29]Plow, E. F., T. A. Haas, L. Zhang, J. Loftus, and J. W. Smith. Ligand binding to integrins. *J. Biol. Chem.* 275:21785–21788, 2000.

[30]Ramirez, F., and H. C. Dietz. Extracellular microfibrils in vertebrate development and disease processes. *J. Biol. Chem.* 284:14677–14681, 2009.

[31]Rodgers, U. R., and A. S. Weiss. Integrin alpha v beta 3 binds a unique non-RGD site near the C-terminus of human tropoelastin. *Biochimie* 86:173–178, 2004.

[32]Rosenbloom, J., W. R. Abrams, and R. Mecham. Extracellular matrix 4: the elastic fiber. *FASEB J.* 7:1208–1218, 1993.

[33]Shiu, Y. T., S. Li, W. A. Marganski, S. Usami, M. A. Schwartz, Y. L. Wang, M. Dembo, and S. Chien. Rho mediates the shear-enhancement of endothelial cell migration and traction force generation. *Biophys. J.* 86: 2558–2565, 2004.

[34]Spencer, J. A., S. L. Hacker, E. C. Davis, R. P. Mecham, R. H. Knutsen, D. Y. Li, R. D. Gerard, J. A. Richardson, E. N. Olson, and H. Yanagisawa. Altered vascular remodeling in fibulin-5-deficient mice reveals a role of fibulin-5 in smooth muscle cell proliferation and migration. *Proc. Natl Acad. Sci. USA* 102:2946–2951, 2005.

[35]Stracke, M. L., J. D. Engel, L. W. Wilson, M. M. Reehler, L. A. Liotta, and E. Schiffmann. The type I insulin-like growth factor receptor is a motility receptor in human melanoma cells. *J. Biol. Chem.* 264:21544–21549, 1989.

[36]Sutherland, D. R., L. Anderson, M. Keeney, R. Nayar, and I. Chin-Yee. The ISHAGE guidelines for CD34+ cell determination by flow cytometry. International Society of Hematotherapy and Graft Engineering. *J. Hematother.* 5:213–226, 1996.

[37]Swanson, N., K. Hogrefe, Q. Javed, N. Malik, and A. H. Gershlick. Vascular endothelial growth factor (VEGF)-eluting stents: in vivo effects on thrombosis, endothelialization and intimal hyperplasia. *J. Invasive Cardiol.* 15:688–692, 2003.

[38]Tzima, E., M. A. del Pozo, S. J. Shattil, S. Chien, and M. A. Schwartz. Activation of integrins in endothelial cells by fluid shear stress mediates Rho-dependent cytoskeletal alignment. *EMBO J.* 20:4639–4647, 2001.

[39]Wachi, H., R. Nonaka, F. Sato, K. Shibata-Sato, M. Ishida, S. Iketani, I. Maeda, K. Okamoto, Z. Urban, S. Onoue, and Y. Seyama. Characterization of the molecular interaction between tropoelastin and DANCE/fibulin-5. *J. Biochem.* 143:633–639, 2008.

[40]Williamson, M. R., A. Shuttleworth, A. E. Canfield, R. A. Black, and C. M. Kielty. The role of endothelial cell attachment to elastic fibre molecules in the enhancement of monolayer formation and retention, and the inhibition of smooth muscle cell recruitment. *Biomaterials* 28:5307–5318, 2007.

[41]Yin, Y., S. G. Wise, N. J. Nosworthy, A. Waterhouse, D. V. Bax, H. Youssef, M. J. Byrom, M. M. Bilek, D. R. McKenzie, A. S. Weiss, and M. K. Ng. Covalent immobilisation of tropoelastin on a plasma deposited interface for enhancement of endothelialisation on metal surfaces. *Biomaterials* 30:1675–1681, 2009.

[42]Yoshigi, M., E. B. Clark, and H. J. Yost. Quantification of stretch-induced cytoskeletal remodeling in vascular endothelial cells by image processing. *Cytometry A* 55:109–118, 2003.

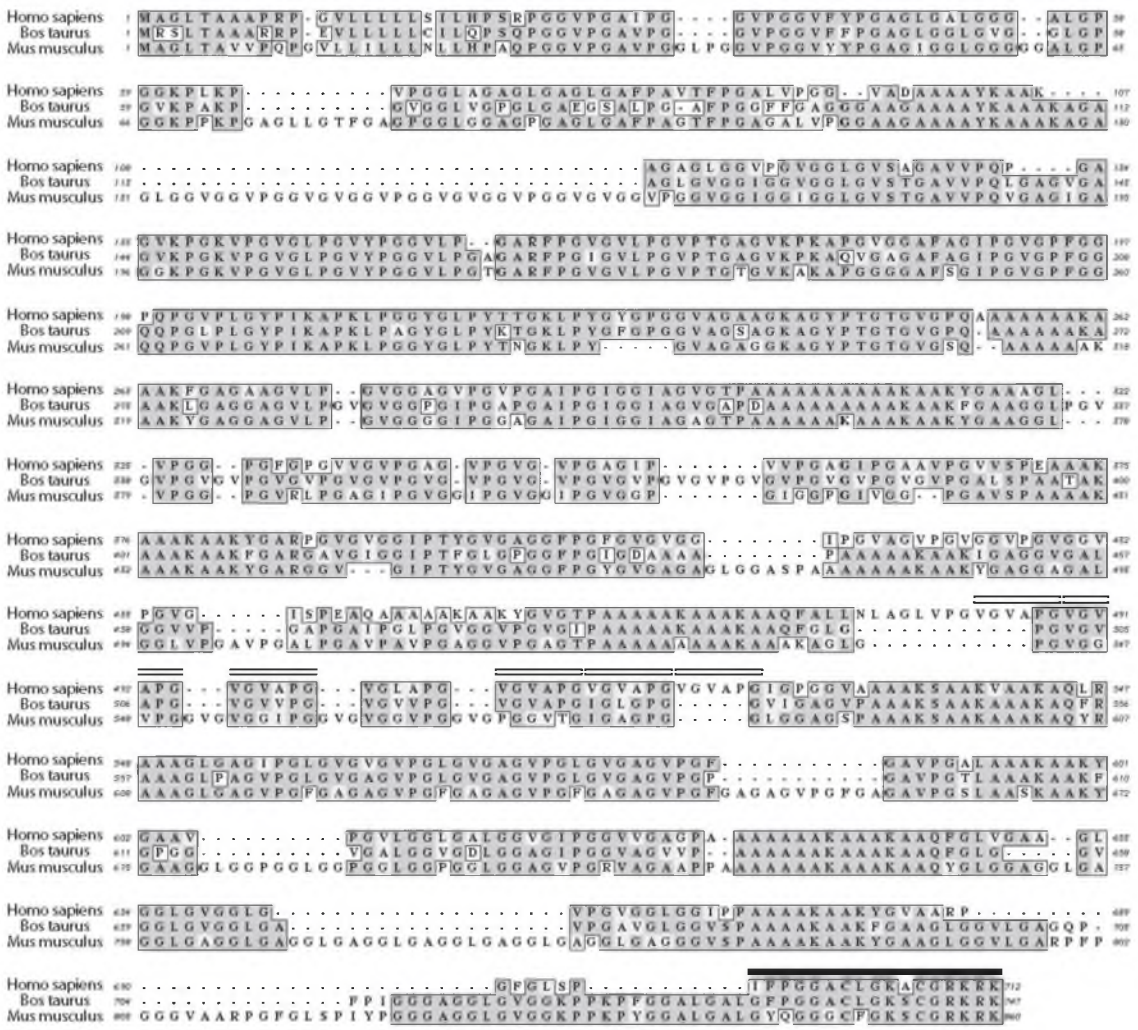


**Supplementary Figure 1. Alignment of human, bovine, and murine tropoelastin amino acid sequences.** The hexapeptide VGVAPG is repeated 6 times (open boxes) near the mid-portion of human tropoelastin. The 17-carboxy-terminal amino acids (black box) of tropoelastin are well conserved in all three species (82.4% similarity). This carboxy-terminal region appears to mediate signaling through the integrin $\alpha_V\beta_3$.

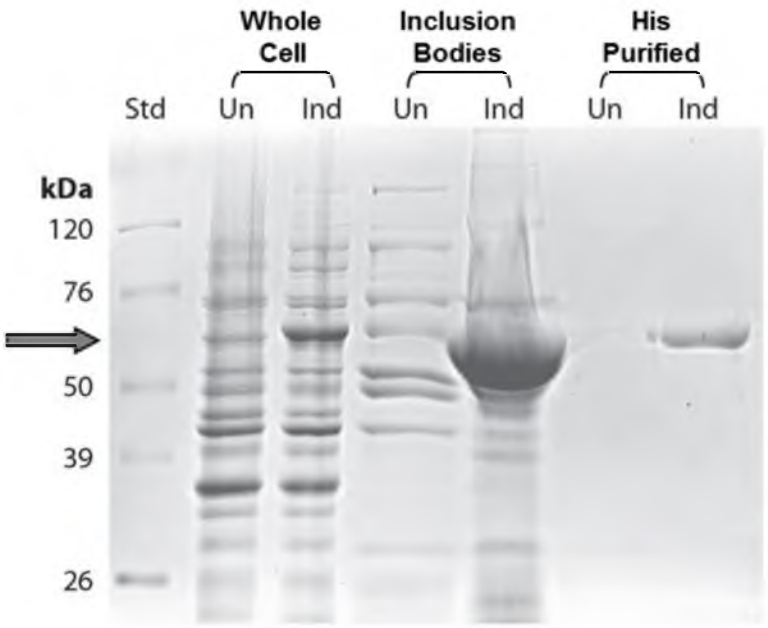


**Supplementary Figure 2. SDS-PAGE analysis of purified recombinant human tropoelastin produced in bacteria.** Following IPTG induction, whole cell lysates were prepared and electrophoresed on a 10% polyacrylamide gel, where the first column shows the standard protein markers (Std). In induced whole cell extracts (Ind), a band of expected molecular weight (arrow, ~65 kDa) was observed that was not seen in uninduced controls (Un). Isolation of bacterial inclusion bodies resulted in significant enrichment of recombinant protein. The last column shows that His-tagged human tropoelastin was purified to near homogeneity using nickel matrix binding and elution with imidazole.

# CHAPTER 2

## INTERLEUKIN RECEPTOR ACTIVATES A MYD88-ARNO-ARF6 CASCADE TO DISRUPT VASCULAR STABILITY

The following chapter was reprinted with permission from Macmillian Publishers Limited. I was co-first author of this paper with Weiquan Zhu and Nyall R. London. In addition, the other authors were Chadwick T. Davis, Zongzhong Tong, Lise K. Sorensen, Dallas S. Shi, Jinping Guo, Matthew C.P. Smith, Allie H. Grossmann, Kirk R. Thomas, and Dean Y. Li. This article was originally published in Nature, 2012 Dec;492:252-255. This manuscript details the role of ARF6, a small GTPase, in stabilization of the endothelium to an inflammatory cue, interleukin 1-β.

LETTER

doi:10.1038/nature11603

# Interleukin receptor activates a MYD88–ARNO–ARF6 cascade to disrupt vascular stability

Weiquan Zhu[1,2]*, Nyall R. London[1,2,3]*, Christopher C. Gibson[2,4]*, Chadwick T. Davis[2,5], Zongzhong Tong[6], Lise K. Sorensen[2], Dallas S. Shi[2,5], Jinping Guo[1,2,7], Matthew C. P. Smith[1,2,3], Allie H. Grossmann[2,8], Kirk R. Thomas[1,2] & Dean Y. Li[1,2,3,9,10]

**The innate immune response is essential for combating infectious disease. Macrophages and other cells respond to infection by releasing cytokines, such as interleukin-1β (IL-1β), which in turn activate a well-described, myeloid-differentiation factor 88 (MYD88)-mediated, nuclear factor-κB (NF-κB)-dependent transcriptional pathway that results in inflammatory-cell activation and recruitment[1–4]. Endothelial cells, which usually serve as a barrier to the movement of inflammatory cells out of the blood and into tissue, are also critical mediators of the inflammatory response[5,6]. Paradoxically, the cytokines vital to a successful immune defence also have disruptive effects on endothelial cell–cell interactions and can trigger degradation of barrier function and dissociation of tissue architecture[7–9]. The mechanism of this barrier dissolution and its relationship to the canonical NF-κB pathway remain poorly defined. Here we show that the direct, immediate and disruptive effects of IL-1β on endothelial stability in a human *in vitro* cell model are NF-κB independent and are instead the result of signalling through the small GTPase ADP-ribosylation factor 6 (ARF6) and its activator ARF nucleotide binding site opener (ARNO; also known as CYTH2). Moreover, we show that ARNO binds directly to the adaptor protein MYD88, and thus propose MYD88–ARNO–ARF6 as a proximal IL-1β signalling pathway distinct from that mediated by NF-κB. Finally, we show that SecinH3, an inhibitor of ARF guanine nucleotide-exchange factors such as ARNO, enhances vascular stability and significantly improves outcomes in animal models of inflammatory arthritis and acute inflammation.**

A defining characteristic of the cytokine-induced inflammatory response is the destabilization of endothelial barriers resulting in vascular permeability[7–9]. To dissect the pathway(s) involved in this tissue disruption, we treated cultured monolayers of human dermal microvascular endothelial cells (HMVEC-d) with IL-1β, and detected an increase in endothelial permeability within 15 min (Fig. 1a). The canonical IL-1β pathway involves ligand-stimulated activation of interleukin-1 receptor (IL-1R), which recruits MYD88 to its cytoplasmic tail[10]. The subsequent signalling cascade through IRAK1 results in the phosphorylation of IκB-α by the IκB kinase (IKK) complex, leading to translocation of NF-κB to the nucleus and the eventual transcription of target genes that promote inflammatory-cell responses[3,4] (Supplementary Fig. 1). To test the involvement of this pathway in IL-1β-induced vascular permeability, cells were treated with the IKK inhibitor SC-514 (ref. 11). Although SC-514 prevented IL-1β-induced nuclear localization of NF-κB, it was unable to rescue either IL-1β-induced permeability or disruption of vascular endothelial (VE)-cadherin surface localization (Fig. 1b, c and Supplementary Fig. 2a–c). We also wondered whether IL-1β-induced vascular permeability required other known MYD88-mediated downstream signalling mechanisms, including ERK1/2, p38 and JNK (also known as MAPK3/MAPK1, MAPK14 and MAPK8, respectively)[12,13]. Although ERK1/2, p38 and JNK were activated by IL-1β stimulation of endothelial cells, small-molecule inhibitors of each of these pathways were unable to prevent IL-1β-induced vascular permeability or IL-1β-induced disruption of VE-cadherin cell-surface localization (Supplementary Fig. 2d–h). Although specific NF-κB targets, such as VEGFA, COX-2 (also known as PTGS2) and the COX-2 product prostaglandin $E_2$ are modulated by IL-1β, their activation had no effect on IL-1β-induced endothelial permeability[3,14,15] (Supplementary Fig. 3a–e). Finally, treatment with actinomycin D or cycloheximide effectively inhibited transcription or translation, respectively, of NF-κB targets, but did not blunt IL-1β-induced permeability (Fig. 1d and Supplementary Fig. 3f, g). These data strongly support a role for the immediate and destabilizing effects of IL-1β on endothelial stability through signalling pathways independent of NF-κB, transcription and translation.

IL-1β can disrupt VE-cadherin cell-surface localization by promoting endocytic internalization[9]. We proposed that IL-1β might use ARF6, a known regulator of adherens protein localization[16,17]. Indeed, IL-1β activated ARF6 in HMVEC-d within 1 min, a response accompanied by increased endocytosis of VE-cadherin within 5 min and an increase in monolayer permeability within 15 min (Fig. 1a, e and Supplementary Fig. 4a, b). IL-1β treatment did not affect total VE-cadherin messenger RNA or protein levels (Supplementary Fig. 4c, d). Adenoviral-mediated overexpression of constitutively active ARF6 (ARF6(Q67L))[16] elicited a dose-dependent increase in endothelial permeability, as well as a disruption of VE-cadherin cell-surface localization (Fig. 1f, g and Supplementary Fig. 4e, f). A similar dose-dependent loss of total VE-cadherin was also observed, probably through internalization and subsequent degradation (Supplementary Fig. 4g). Interestingly, at lower doses of adenovirus at which permeability was still induced, loss of total VE-cadherin was not observed, but a dose-dependent loss of cell-surface VE-cadherin occurred (Fig. 1f–h and Supplementary Fig. 4g). Moreover, short interfering RNA (siRNA) knockdown of *ARF6* enhanced VE-cadherin cell-surface localization and prevented both IL-1β-induced disruption of VE-cadherin and IL-1β-induced endothelial permeability (Fig. 1i–k and Supplementary Fig. 4h, i). Collectively, these data link ARF6 as a critical regulator of VE-cadherin trafficking by controlling cell-surface localization and the immediate and disruptive effects of IL-1β-induced vascular permeability.

The ARF6 activation state is decreased through interaction with GTPase-activating proteins (GAPs) and increased through interaction with guanine nucleotide-exchange factors (GEFs). Consistent with this, treatment of endothelial cells with the ARF-GAP inhibitor QS11 evoked an increase in ARF6–GTP, a decrease in VE-cadherin cell-surface localization and increased permeability (Fig. 2a–d and

[1]Department of Medicine, University of Utah, Salt Lake City, Utah 84112, USA. [2]Program in Molecular Medicine, University of Utah, Salt Lake City, Utah 84112, USA. [3]Department of Oncological Sciences, University of Utah, Salt Lake City, Utah 84112, USA. [4]Department of Bioengineering, University of Utah, Salt Lake City, Utah 84112, USA. [5]Department of Human Genetics, University of Utah, Salt Lake City, Utah 84112, USA. [6]Navigen Inc, Salt Lake City, Utah 84112, USA. [7]Department of Anatomy, Second Military Medical University, Shanghai 200433, China. [8]Department of Pathology, University of Utah, Salt Lake City, Utah 84112, USA. [9]Cardiology Section, VA Salt Lake City Health Care System, Salt Lake City, Utah 84112, USA. [10]The Key Laboratory for Human Disease Gene Study of Sichuan Province, Institute of Laboratory Medicine, Sichuan Academy of Medical Sciences & Sichuan Provincial People's Hospital, Chengdu, Sichuan 610072, China.
*These authors contributed equally to this work.

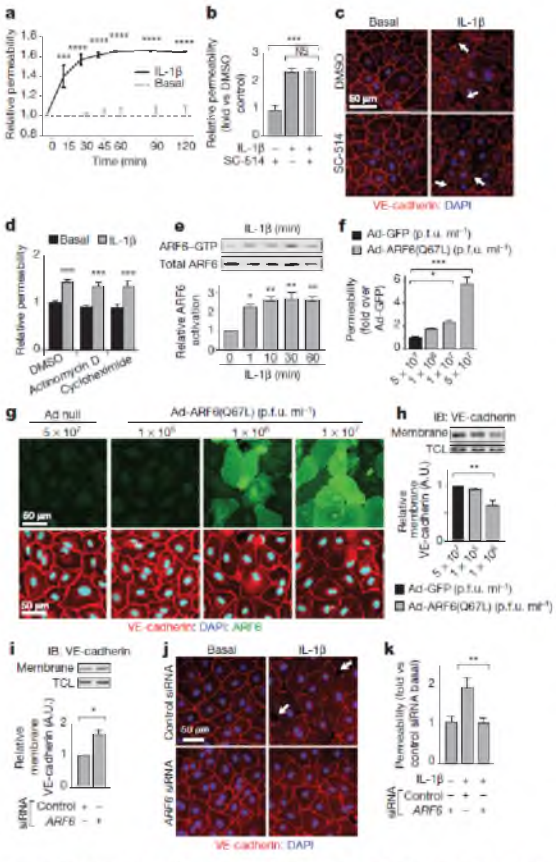

**Figure 1 | Immediate effects of IL-1β are NF-κB independent and ARF6 dependent.** a–d, Monolayers of HMVEC-d stimulated with IL-1β and assayed for permeability to horseradish peroxidase (HRP) over time (a), permeability to HRP following 2-h treatment with SC-514 (b), immunofluorescent localization of VE-cadherin (c) and permeability to HRP after 30-min treatment with actinomycin D or cycloheximide (d). e, IL-1β-stimulated HMVEC-d lysates were precipitated with glutathione *S*-transferase (GST)–GGA3 and immunoblotted for ARF6. f–i, HMVEC-d monolayers infected with adenovirus (Ad) containing empty vector (null), green fluorescent protein (GFP) or ARF6(Q67L), showing permeability (f) and VE-cadherin localization (g) (green denotes ARF6 expression). Membrane fractions from adenoviral-vector-infected (h) or *ARF6*-siRNA-treated (i) HMVEC-d were immunoblotted for VE-cadherin. j, k, *ARF6*-siRNA-treated HMVEC-d stimulated with IL-1β, showing VE-cadherin localization (j) (arrows denote disrupted VE-cadherin cell-surface localization) and permeability (k). A.U., arbitrary unit; DMSO, dimethylsulphoxide; IB, immunoblot; TCL, total cell lysate. $n \geq 3$; error bars denote s.e.m. $^{*}P < 0.05$, $^{**}P < 0.01$, $^{***}P < 0.001$, $^{****}P < 0.0001$.

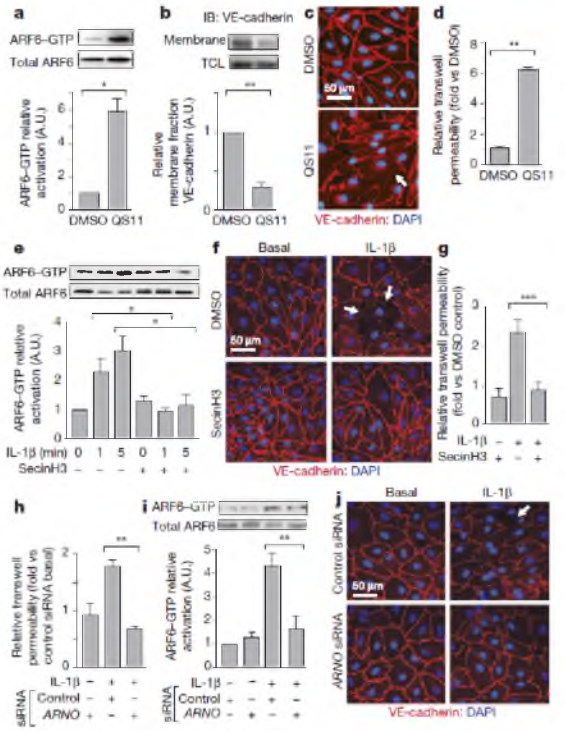

**Figure 2 | Inhibition of ARF-GAPs and ARF-GEFs affect ARF6 activation and VE-cadherin localization.** a–d, HMVEC-d treated with QS11, showing whole-cell lysates precipitated with GST–GGA3 and immunoblotted for ARF6 (a), membrane fractions immunoblotted for VE-cadherin (b), immunofluorescence for VE-cadherin (red) (c) and permeability to HRP (d). e–g, HMVEC-d treated with IL-1β and SecinH3, showing immunoblotting for ARF6 (e), immunofluorescence for VE-cadherin (f) and permeability to HRP (g). h–j, HMVEC-d treated with anti-*ARNO* siRNA and stimulated with IL-1β, showing permeability to HRP (h), GST–GGA3 precipitation and ARF6 immunoblotting (i) and immunofluorescence of VE-cadherin (j). Arrow denotes less cell-surface VE-cadherin. $n \geq 3$; error bars denote s.e.m. $^{*}P < 0.05$, $^{**}P < 0.01$, $^{***}P < 0.001$.

Supplementary Fig. 5a, b)[19]. We noted that a class of ARF-GEFs, the cytohesins, is highly expressed in multiple types of endothelial cells (Supplementary Fig. 5c). Accordingly, treatment of HMVEC-d with SecinH3, a cytohesin inhibitor, significantly increased endothelial cell-surface localization of VE-cadherin (Supplementary Fig. 5d–f)[20]. Notably, SecinH3 inhibited IL-1β-induced ARF6–GTP, as well as IL-1β-induced disruption of VE-cadherin cell-surface localization and endothelial permeability (Fig. 2e–g and Supplementary Fig. 5g, h). To determine which GEF might be uniquely involved, we used siRNA to knockdown *CYTH1*, *ARNO* and *CYTH3* (coding for cytohesins 1, 2 and 3, respectively) and *GEP100* (also known as *IQSEC1*) (Supplementary Fig. 6a), and found that only siRNA targeting *ARNO* completely blocked IL-1β-induced endothelial permeability and phenocopied the knockdown of *ARF6* (Fig. 2h and Supplementary Fig. 6b). Furthermore, *ARNO* siRNA inhibited IL-1β-induced ARF6–GTP formation, IL-1β-induced disruption of VE-cadherin cell–cell contacts and IL-1β-induced internalization of surface VE-cadherin (Fig. 2i, j and Supplementary Fig. 6c, g); all of these effects were rescued by the expression of siRNA-resistant *ARNO* (Supplementary Fig. 6d–g). In cells treated with *ARNO* siRNA, viral expression of siRNA-resistant *ARNO*, but not viral expression of siRNA-resistant *ARNO(E156K)* (carrying a mutation in the Sec7 domain), rescued the disruption of IL-1β-induced ARF6–GTP formation and permeability[21] (Supplementary Fig. 6d, e). These data demonstrate that ARNO is a critical ARF-GEF necessary for IL-1β-induced activation of ARF6 and subsequent induction of vascular permeability, but does not rule out the role of other GEF family members in similar responses in different cell types or in response to different cytokines.

The signalling components in the NF-κB pathway downstream of IL-1β-induced activation of IL-1R are well characterized (Supplementary Fig. 1). Although the inhibition of the NF-κB pathway at the level of IRAK1 by siRNA did not inhibit IL-1β-induced ARF6 activation, siRNA knockdown of *MYD88* inhibited both IL-1β-induced permeability and ARF6–GTP activation, suggesting a bifurcation of

IL-1β-induced signalling at the point of MYD88 (Fig. 3a–c and Supplementary Fig. 7a, b). The proposed bifurcation was further verified by the pharmacological uncoupling of the two pathway arms: although SecinH3 blunted IL-1β-induced permeability, it did not significantly inhibit IL-1β-induced NF-κB nuclear localization or NF-κB-dependent expression or localization of cell-surface adhesion molecules (Fig. 3d and Supplementary Fig. 7c, d). Furthermore, SecinH3 was unable to inhibit IL-1β-induced polymorphonuclear leukocyte rolling and adherence under shear stress on an endothelial monolayer (Supplementary Fig. 7e). Mechanistic support for this novel signalling arm was provided by the demonstration of an interaction between MYD88 and ARNO by co-immunoprecipitation in both overexpression and endogenous settings (Fig. 3e, f). Our hypothesis that ARNO is the critical GEF in IL-1β-induced permeability in endothelial cells was further strengthened by our inability to detect an interaction between MYD88 and other potentially relevant ARF-GEFs including CYTH1, CYTH3 and GEP100 (Supplementary Fig. 7f, g).

An effective therapeutic strategy to combat numerous inflammatory conditions is to target pro-inflammatory cytokines proximal to the NF-κB pathway. However, this strategy can result in undesired pleiotropic effects. We wanted to know whether targeting a single arm in this pathway—the one mediated by ARNO–ARF6—could inhibit acute or chronic inflammation *in vivo* in two animal models of inflammation. The first model we tested was rheumatoid arthritis, a disease characterized by a dysregulated cytokine response causing excessive inflammation and tissue damage and treated therapeutically in humans with the anti-cytokine tumour necrosis factor receptor (TNFR)–Fc fusion protein etanercept (Enbrel)[22–25]. A standard animal model of arthritis through which a TNFR fusion approach has been proven effective is collagen-induced arthritis (CIA)[24–26]. Exposure of animals to the cytohesin inhibitor SecinH3 after the onset of CIA reduced vascular permeability in the joints, but had no effect on global cytokine levels at 24 h after treatment initiation (Fig. 4a and Supplementary Fig. 8a, b). In addition, a significant inhibition in the increase in arthritic index, comparable to that achieved by treatment with Enbrel, was observed. The arthritic index is a scoring system determined by the number of digits or joints that are oedematous or erythematous. The significance of our findings was verified by histologic scoring of inflammation, pannus development, cartilage damage and bone damage (Fig. 4c, d). A similar effect of SecinH3 was confirmed in a second model of inflammation, the carrageenan air-pouch model. Six hours after an inflammatory stimulus, a time at which substantial inflammation was induced in the positive control mice, treatment with SecinH3 decreased exudate volume as well as leukocyte concentration in the exudates (Supplementary Fig. 8c, d). Collectively, these data identify MYD88–ARNO–ARF6 as a valid target for inflammatory conditions confirming a relevant role for manipulation of this pathway *in vivo* to modulate inflammatory processes and in the treatment of disease.

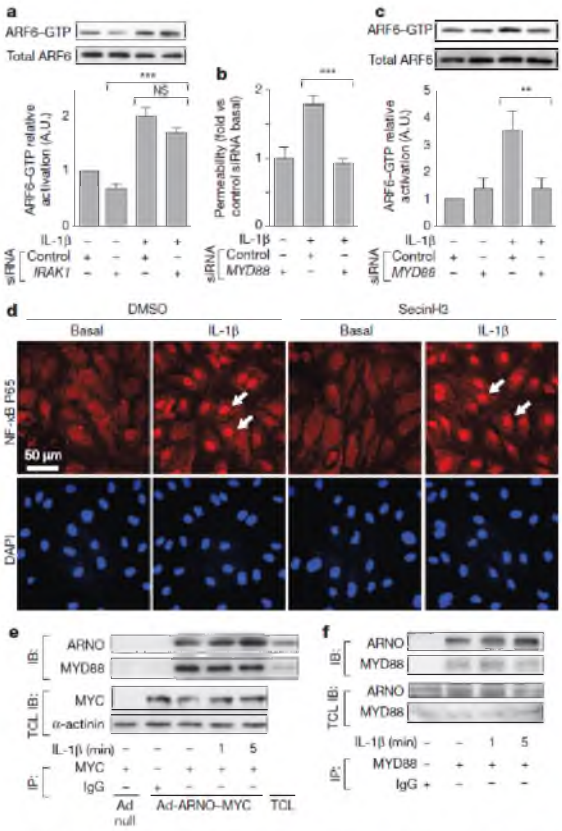


**Figure 3 | The immediate IL-1β-induced permeability pathway diverges at MYD88.** **a**, *IRAK1*-siRNA-treated HMVEC-d, stimulated with IL-1β, subjected to ARF6–GTP pull-down and immunoblotted for ARF6. **b**, **c**, *MYD88*-siRNA-treated HMVEC-d stimulated with IL-1β, showing permeability and ARF6 activation. **d**, NF-κB p65 (also known as RELA) immunofluorescence in HMVEC-d stimulated with IL-1β and SecinH3. Arrows denote nuclear localization. **e**, Cell lysates from Ad-ARNO–MYC-infected HMVEC-d immunoprecipitated (IP) with anti-MYC antibodies and immunoblotted with anti-MYD88 antibodies. **f**, Lysates from HMVEC-d immunoprecipitated with anti-MYD88 antibodies and immunoblotted with anti-ARNO antibodies. $n \geq 3$. Error bars denote s.e.m. $^{*}P < 0.05$, $^{**}P < 0.01$, $^{***}P < 0.001$.

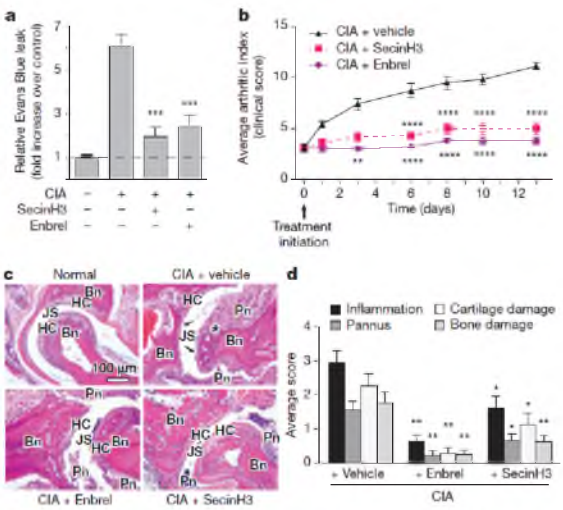


**Figure 4 | Inhibition of ARF-GEFs decreases collagen-induced vascular permeability and arthritis in mice.** **a**, Arthritis-induced vascular permeability in the joint measured by Evans Blue leak 7 days after treatment initiation in the presence of SecinH3 or Enbrel. $n = 14$ per group. **b**, Chronological arthritic assessment. $n = 10$ per group. Significance values are measured against CIA plus vehicle. **c**, Haematoxylin and eosin staining of sections through joints. Bn, bone; HC, hyaline cartilage; JS, joint space; Pn, inflamed pannus. Asterisk denotes cartilage and bone loss; arrows denote eroded cartilage. **d**, Summary of histological changes of inflammation, pannus, cartilage and bone damage of indicated treatment. Control, $n = 5$; Enbrel and SecinH3, $n = 10$. Error bars denote s.e.m. $^{*}P < 0.05$, $^{**}P < 0.01$, $^{***}P < 0.001$, $^{****}P < 0.0001$ versus disease group.

Chronic inflammation causes tissue destruction through dysregulated cytokine release, inflammatory cell recruitment and vascular permeability; yet each of these mechanisms has critical roles in many physiologic processes, including the immune response[5–7]. We have identified a novel pathway that uncouples cytokine effects on vascular stability from other critical functions of the canonical NF-κB transcription program (Supplementary Fig. 1). Our model suggests the potential for inhibition of vascular leak without modulation of immune-cell adhesion or other critical NF-κB-dependent responses.

The activation of many inflammatory cytokine receptors disrupts cell–cell interactions, precipitating tissue oedema and destruction[5,7,9,27]. Toll-like receptors and the interleukin receptor also use MYD88, and the mechanism described here may well apply[3,10]. Interestingly, TNFR1 (also known as TNFRSF1A) does not use MYD88 yet still activates ARF6–GTP after stimulation (Supplementary Fig. 9). Whether ARNO or another ARF-GEF binds directly to TNFR1 or its adaptor protein TRADD is unknown, as is the possibility that ARF-GEF–ARF6–cadherin serves as a common signalling module exploited by multiple cytokines. Although this study focused on the endothelium, the concept of cytokine receptor–ARF–cadherin may also apply to the epithelial barrier, which expresses these constituents and is also compromised by cytokines including IL-1β[16].

Inhibition of this novel vascular-stability pathway, which is aimed at enhancing the resilience of the host to the cytokine response, shows effects commensurate to those of class-leading drugs that target cytokines upstream of NF-κB and seek to blunt the cytokine response of the immune system outright. This approach may be particularly useful in arthritis, as the current medical therapy can render a patient immunocompromised and susceptible to reactivation of infectious disease such as tuberculosis[28]. Application of these findings to other diseases characterized by excessive acute or chronic inflammatory states, including sepsis, Crohn's disease, ulcerative colitis, scleroderma and psoriasis, should also be considered[9,29,30].

## METHODS SUMMARY

**Transwell permeability.** HMVEC-d cells were seeded on 1.0-μm Costar transwell inserts coated with fibronectin. Cells were grown to confluency and treated with SecinH3 for 3 h or MAPK/NF-κB/transcription/translation inhibitors for 30 min followed by treatment with 10 ng ml$^{-1}$ IL-1β. Alternatively, cells were infected with Ad-GFP or Ad-ARF6(Q67L) for 48 h. siRNA knockdown was performed as described in Supplementary Methods, and cells were treated with IL-1β 72 h after the second siRNA transfection. Two hours later, HRP was added to the top chamber at a final concentration of 100 μg ml$^{-1}$. Medium was removed after 60 min from the lower chamber. For time-course transwell assays and transcription/translation-inhibitor experiments (Fig. 1a, c, d), HRP was added to the insert at the same time as IL-1β. Transwell inserts were moved to fresh wells after each time point, and the concentration of HRP in the bottom chamber was measured for monolayer permeability. HRP was assessed using media samples obtained from the lower chamber incubated with 0.5 mM of guaiacol and 0.6 mM $H_2O_2$. Spectrophotometric analysis of absorbance at 490 nm provided a quantitative evaluation of the amount of HRP that crossed the membrane. Data are presented as mean ± s.e.m. of at least three independent experiments performed in quadruplicate.

A detailed description of all methods is provided in Supplementary Information.

**Received 9 December 2011; accepted 19 September 2012.**

**Published online 11 November 2012.**

1. Li, Q. & Verma, I. M. NF-κB regulation in the immune system. *Nature Rev. Immunol.* **2,** 725–734 (2002).
2. Collins, T. *et al.* Transcriptional regulation of endothelial cell adhesion molecules: NF-κB and cytokine-inducible enhancers. *FASEB J.* **9,** 899–909 (1995).
3. Liu, S. F. & Malik, A. B. NF-κB activation as a pathological mechanism of septic shock and inflammation. *Am. J. Physiol. Lung Cell. Mol. Physiol.* **290,** L622–L645 (2006).
4. Rothwarf, D. M. & Karin, M. The NF-κB activation pathway: a paradigm in information transfer from membrane to nucleus. *Sci. STKE* **1999,** RE1 (1999).
5. Pober, J. S. & Sessa, W. C. Evolving functions of endothelial cells in inflammation. *Nature Rev. Immunol.* **7,** 803–815 (2007).
6. Muller, W. A. Leukocyte–endothelial cell interactions in the inflammatory response. *Lab. Invest.* **82,** 521–533 (2002).
7. Royall, J. A. *et al.* Tumor necrosis factor and interleukin 1 alpha increase vascular endothelial permeability. *Am. J. Physiol. Lung Cell. Mol. Physiol.* **257,** L399–L410 (1989).
8. West, X. Z. *et al.* Oxidative stress induces angiogenesis by activating TLR2 with novel endogenous ligands. *Nature* **467,** 972–976 (2010).
9. London, N. R. *et al.* Targeting Robo4-dependent Slit signaling to survive the cytokine storm in sepsis and influenza. *Sci. Transl. Med.* **2,** 23ra19 (2010).
10. Zhu, J. & Mohan, C. Toll-like receptor signaling pathways–therapeutic opportunities. *Mediators Inflamm.* **2010,** 781235 (2010).
11. Kishore, N. *et al.* A selective IKK-2 inhibitor blocks NF-κB-dependent gene expression in interleukin-1β-stimulated synovial fibroblasts. *J. Biol. Chem.* **278,** 32861–32871 (2003).
12. Matthews, J. S. & O'Neill, L. A. Distinct roles for p42/p44 and p38 mitogen-activated protein kinases in the induction of IL-2 by IL-1. *Cytokine* **11,** 643–655 (1999).
13. Martin, M. U. & Wesche, H. Summary and comparison of the signaling mechanisms of the Toll/interleukin-1 receptor family. *Biochim. Biophys. Acta* **1592,** 265–280 (2002).
14. Kaltschmidt, B., Linker, R. A., Deng, J. & Kaltschmidt, C. Cyclooxygenase-2 is a neuronal target gene of NF-κB. *BMC Mol. Biol.* **3,** 16 (2002).
15. Funk, C. D. Prostaglandins and leukotrienes: advances in eicosanoid biology. *Science* **294,** 1871–1875 (2001).
16. Palacios, F., Price, L., Schweitzer, J., Collard, J. G. & D'Souza-Schorey, C. An essential role for ARF6-regulated membrane traffic in adherens junction turnover and epithelial cell migration. *EMBO J.* **20,** 4973–4986 (2001).
17. D'Souza-Schorey, C., Li, G., Colombo, M. I. & Stahl, P. D. A regulatory role for ARF6 in receptor-mediated endocytosis. *Science* **267,** 1175–1178 (1995).
18. Riley, K. N., Maldonado, A. E., Tellier, P., D'Souza-Schorey, C. & Herman, I. M. Betacap73–ARF6 interactions modulate cell shape and motility after injury *in vitro*. *Mol. Biol. Cell* **14,** 4155–4161 (2003).
19. Zhang, Q. *et al.* Small-molecule synergist of the Wnt/β-catenin signaling pathway. *Proc. Natl Acad. Sci. USA* **104,** 7444–7448 (2007).
20. Hafner, M. *et al.* Inhibition of cytohesins by SecinH3 leads to hepatic insulin resistance. *Nature* **444,** 941–944 (2006).
21. Béraud-Dufour, S. *et al.* A glutamic finger in the guanine nucleotide exchange factor ARNO displaces $Mg^{2+}$ and the β-phosphate to destabilize GDP on ARF1. *EMBO J.* **17,** 3651–3659 (1998).
22. Arend, W. P. Cytokine imbalance in the pathogenesis of rheumatoid arthritis: the role of interleukin-1 receptor antagonist. *Semin. Arthritis Rheum.* **30,** 1–6 (2001).
23. Szekanecz, Z. & Koch, A. E. Vascular involvement in rheumatic diseases: 'vascular rheumatology'. *Arthritis Res. Ther.* **10,** 224 (2008).
24. van den Berg, W. B., Joosten, L. A., Helsen, M. & van de Loo, F. A. Amelioration of established murine collagen-induced arthritis with anti-IL-1 treatment. *Clin. Exp. Immunol.* **95,** 237–243 (1994).
25. Joosten, L. A., Helsen, M. M., van de Loo, F. A. & van den Berg, W. B. Anticytokine treatment of established type II collagen-induced arthritis in DBA/1 mice. A comparative study using anti-TNFα, anti-IL-1α/β, and IL-1Ra. *Arthritis Rheum.* **39,** 797–809 (1996).
26. Wooley, P. H., Dutcher, J., Widmer, M. B. & Gillis, S. Influence of a recombinant human soluble tumor necrosis factor receptor FC fusion protein on type II collagen-induced arthritis in mice. *J. Immunol.* **151,** 6602–6607 (1993).
27. London, N. R., Whitehead, K. J. & Li, D. Y. Endogenous endothelial cell signaling systems maintain vascular stability. *Angiogenesis* **12,** 149–158 (2009).
28. Keane, J. *et al.* Tuberculosis associated with infliximab, a tumor necrosis factor α-neutralizing agent. *N. Engl. J. Med.* **345,** 1098–1104 (2001).
29. Lee, W. L. & Slutsky, A. S. Sepsis and endothelial permeability. *N. Engl. J. Med.* **363,** 689–691 (2010).
30. Silva, L. C., Ortigosa, L. C. & Benard, G. Anti-TNF-α agents in the treatment of immune-mediated inflammatory diseases: mechanisms of action and pitfalls. *Immunotherapy* **2,** 817–833 (2010).

**Supplementary Information** is available in the online version of the paper.

**Acknowledgements** We thank D. Lim and T. Mleynek for graphical assistance, G. Zimmerman and J. Kaplan for reading the manuscript, S. Odelberg for reading the manuscript and statistical analysis, J. Ling for help with immunostaining, R. Campbell and A. Weyrich for providing primary human blood cells, C. Rodesch and the University of Utah Cell Imaging/Fluorescence Facility as well as the University of Utah Flow Cytometry Facility, and M. P. Revelo for help with pathology. D.Y.L. and his laboratory were funded by grants from the National Heart, Lung, and Blood Institute; Burroughs Wellcome Fund; Juvenile Diabetes Research Foundation; NIAID Rocky Mountain Regional Center of Excellence in Biodefense and Emerging Infectious Disease; the American Asthma Foundation; and the Department of Defense. D.Y.L. is the HA and Edna Benning Endowed Professor of Medicine and Cardiology.

**Author Contributions** W.Z., N.R.L., C.C.G. and D.Y.L. were responsible for project conceptualization, experimental design, data analysis and manuscript preparation. W.Z., C.C.G., C.T.D., Z.T., L.K.S., D.S.S. and J.G. performed and collected data for *in vitro* experiments. N.R.L. collected data for *in vivo* experiments. C.C.G. developed software techniques for immunofluorescence analysis. M.C.P.S. performed flow cytometry experiments. Z.T. and K.R.T. made constructs and adenoviruses. A.H.G. provided histology and pathology expertise. D.Y.L. was responsible for funding the project.

**Author Information** Reprints and permissions information is available at www.nature.com/reprints. The authors declare competing financial interests: details are available in the online version of the paper. Readers are welcome to comment on the online version of the paper. Correspondence and requests for materials should be addressed to D.Y.L. (dean.li@u2m2.utah.edu).

SUPPLEMENTARY INFORMATION doi:10.1038/nature11603

**Correction notice**

# Interleukin receptor activates a MYD88–ARNO–ARF6 cascade to disrupt vascular stability

Weiquan Zhu, Nyall R. London, Christopher C. Gibson, Chadwick T. Davis, Zongzhong Tong, Lise K. Sorensen, Dallas S. Shi, Jinping Guo, Matthew C. P. Smith, Allie H. Grossmann, Kirk R. Thomas & Dean Y. Li

*Nature* doi:10.1038/nature11603 (11 November 2012)

In the version of the Supplementary Information originally posted online, two images in Supplementary Fig. 4a were incorrect. These have been replaced in the new version of the Supplementary Information; see Supplementary Information Table of Contents for details.

SUPPLEMENTARY INFORMATION
doi:10.1038/nature11603

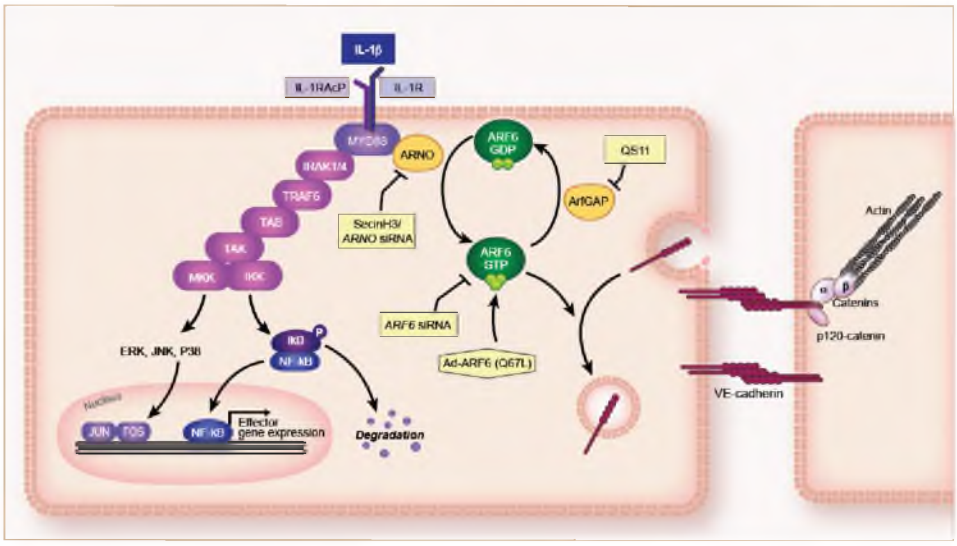


**Supplementary Figure 1. Proposed IL-1β signaling pathways.**
IL-1β activates NF-κB through a MYD88-IRAK-IκB-dependent pathway. MYD88 also binds to ARNO, and through a divergent pathway enhances ARF6-GTP, and decreases VE-cadherin cell surface localization.

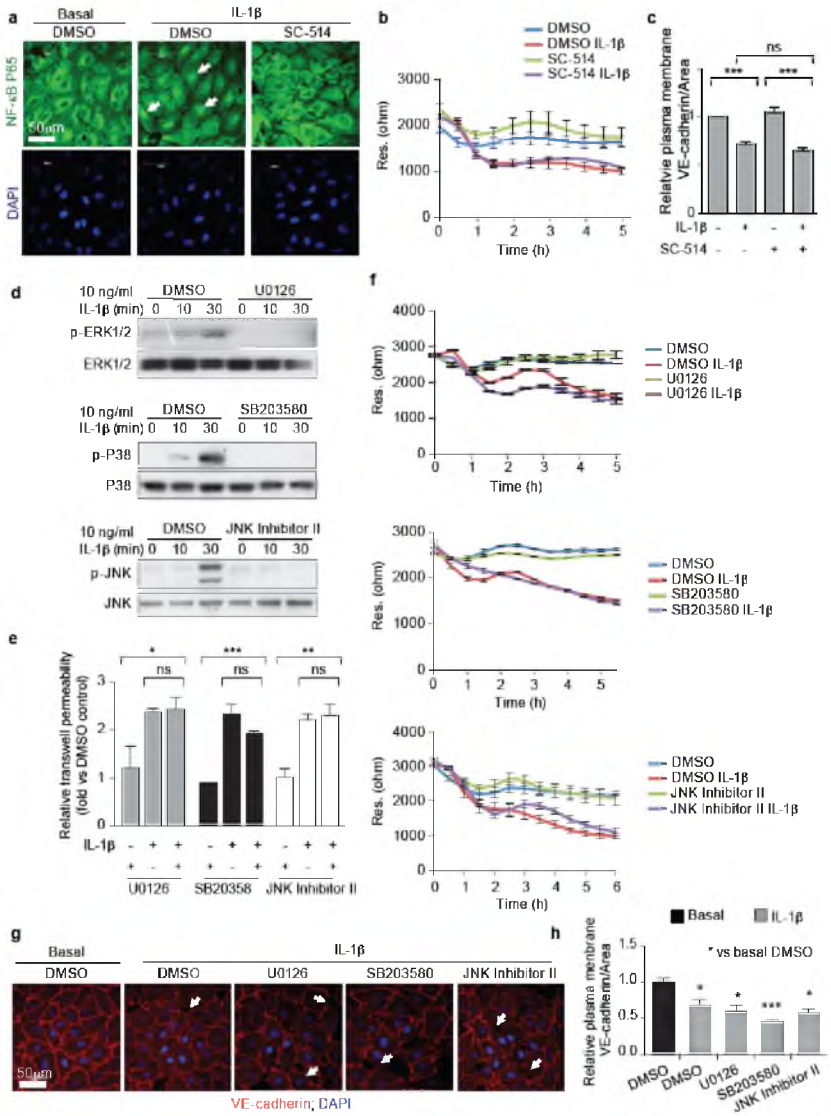


**Supplementary Figure 2. IL-1β-induced permeability is independent of NF-κB, ERK1/2, JNK, and p38.** **(a)** HMVEC-D cells were stimulated with IL-1β in the presence of DMSO or SC-514 and subjected to immunofluorescence for NF-κB (green). White arrows indicate nuclear NF-κB. **(b)** HMVEC-D cells were stimulated with IL-1β in the presence of DMSO or the NF-κB inhibitor, SC-514. Transendothelial resistance was measured by Electric Cell-substrate Impedance Sensing (ECIS). **(c)** Quantification of IL-1β-induced disruption of plasma membrane VE-cadherin treated with DMSO and SC-514 as shown in Figure 1c. **(d)** Lysates from HMVEC-D cells stimulated with IL-1β in the presence of DMSO, U0126, SB203580 or JNK Inhibitor II were subjected to immunoblotting for p-ERK1/2, p-P38, or p-JNK. **(e)** Transwell permeability of HMVEC-D cells stimulated with IL-1β in the presence of inhibitors of ERK1/2 (U0126), P38 (SB203580), and JNK (JNK Inhibitor II). **(f)** Transendothelial resistance was measured by ECIS in HMVEC-D cells treated with IL-1β in the presence of DMSO, ERK1/2 inhibitor U0126, P38 inhibitor SB203580, or JNK Inhibitor II in EGM2-MV complete media. **(g)** VE-cadherin immunofluorescence of HMVEC-D cells treated with IL-1β in the presence of DMSO, U0126, SB203580, or JNK Inhibitor II. White arrows indicate areas of reduced VE-cadherin surface localization. **(h)** Quantification of (g). For all experiments, N ≥ 3 and error bars represent SEM. * p<0.05, ** p<0.01, *** p<0.001.

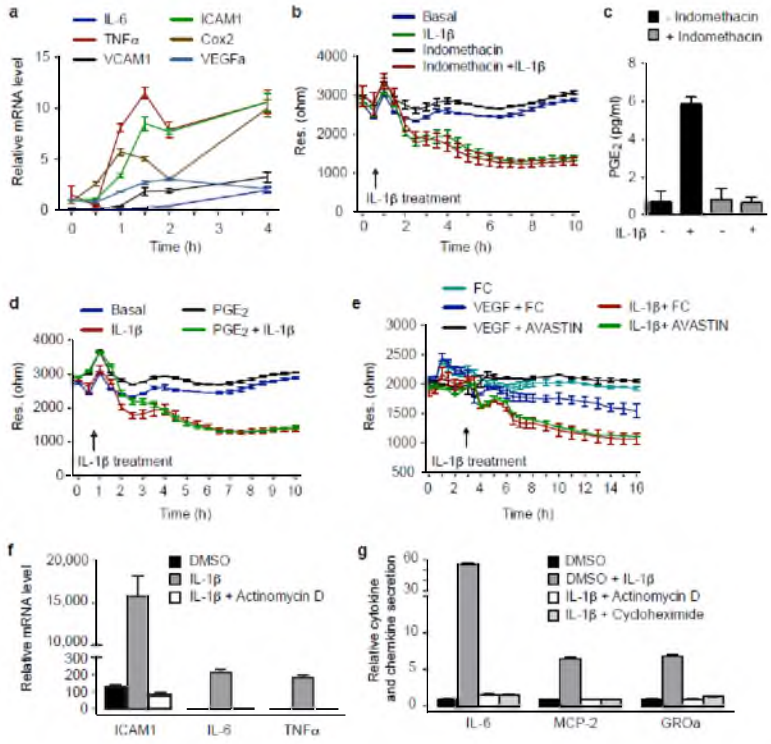


**Supplementary Figure 3. IL-1β induced permeability is independent of NF-κB-transcription and its targets.** **(a)** HMVEC-D cells treated with IL-1β for 0.5, 1, 1.5, 2 or 4 hours were subjected to quantitative RT-PCR to assess NF-κB target gene mRNA levels. **(b)** Transendothelial resistance was measured by ECIS in HMVEC-D cells treated with IL-1β in the presence or absence of a Cox inhibitor, Indomethacin. **(c)** Conditional media from HMVEC-D cells treated with IL-1β in the presence or absence of Indomethacin were subjected to ELISA for $PGE_2$. **(d)** Transendothelial resistance was measured by ECIS in HMVEC-D cells treated with IL-1β in the presence of $PGE_2$. **(e)** Transendothelial resistance was measured by ECIS in HMVEC-D cells treated with IL-1β or VEGF in the presence of anti-VEGF antibody (AVASTIN) or an IgG FC control. **(f)** NF-κB transcriptional targets ICAM1, IL-6 and TNFα mRNA levels were checked by quantitative RT-PCR in HMVEC-D cells treated with IL-1β in the presence or absence of Actinomycin-D. **(g)** NF-κB transcriptional targets IL-6, MCP-2 and GROa protein levels were checked in the conditioned media from HMVEC-D cells treated with IL-1β in the presence or absence of Actinomycin-D and Cycloheximide by ELISA.

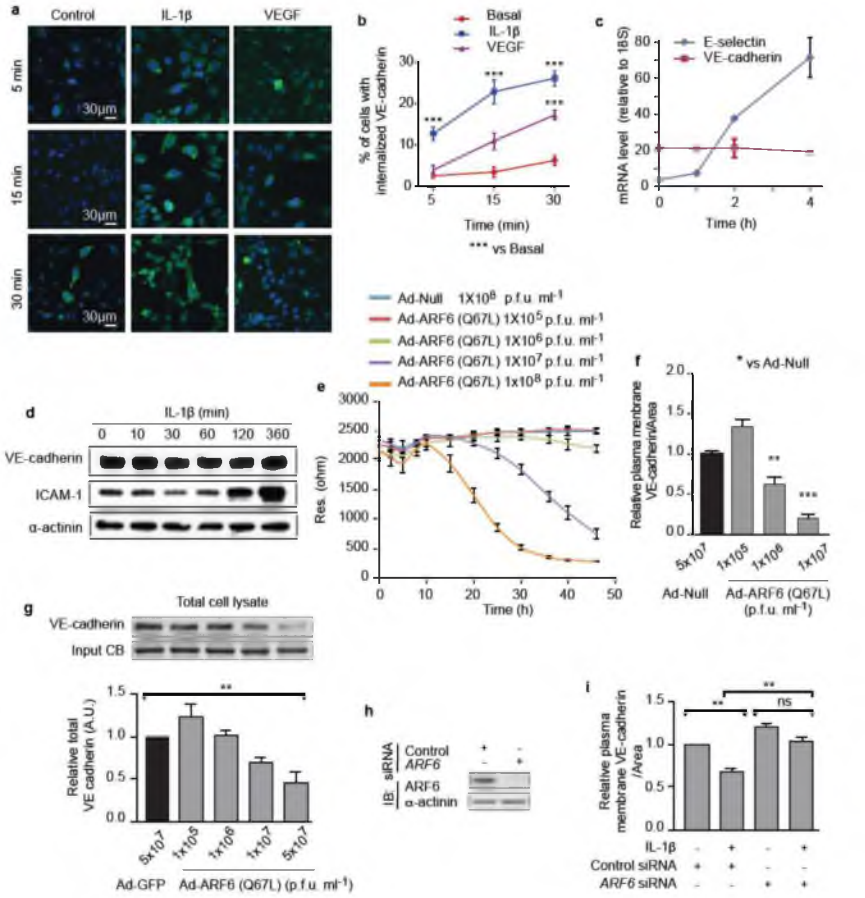


**Supplementary Figure 4. ARF6 constitutive activation enhances vascular permeability.**
**(a)** Immunofluorescence of internalized VE-cadherin (green) in IL-1β and VEGF stimulated HMVEC-D cells after 5, 15, and 30 minutes. **(b)** Quantification of VE-cadherin internalization in IL-1β and VEGF stimulated HMVEC-D cells after 5, 15, and 30 minutes. Induction of VE-cadherin internalization by IL-1 β is more rapid than that induced by VEGF. **(c)** VE-cadherin and E-selectin mRNA levels in IL-1β-stimulated HMVEC-D cells. **(d)** Lysates from IL-1β-stimulated HMVEC-D were immunoblotted with antibodies against VE-Cadherin and ICAM-1 at various time points. **(e)** HMVEC-D cells infected with Ad-Null or Ad-ARF6 (Q67L) adenovirus were assessed for transendothelial resistance by ECIS. **(f)** Quantification of Figure 2e. **(g)** Immunoblotting for VE-cadherin of cell lysates or from ARF6 (Q67L) adenoviral-vector infected HMVEC-D. **(h)** Lysates from HMVEC-D cells transfected with *ARF6* or control siRNA were immunoblotted for ARF6. **(i)** Quantification of Figure 1j. For all experiments, N ≥ 3, and error bars represent SEM. * p<0.05, ** p<0.01, *** p<0.001, **** p<0.0001.

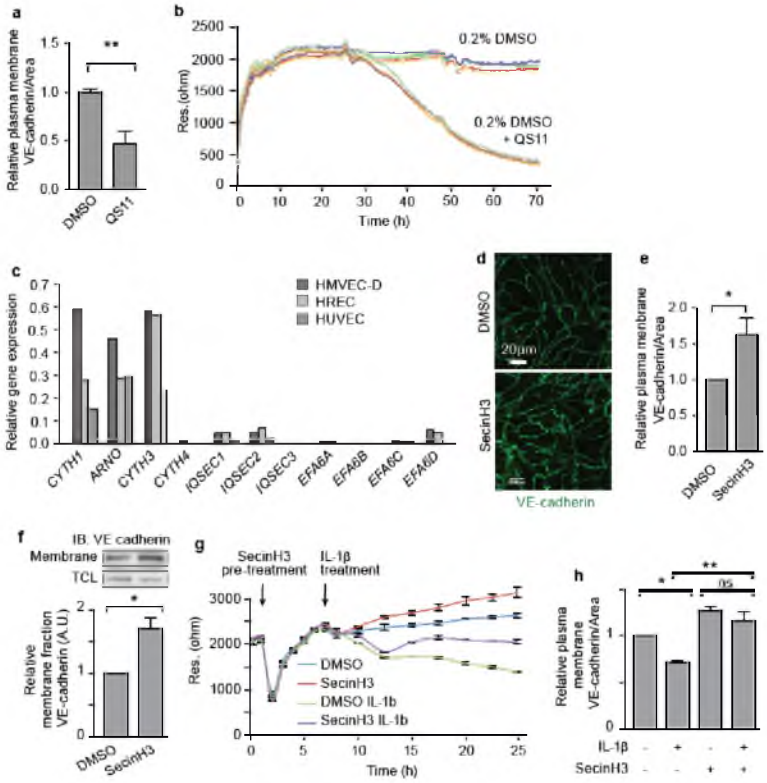


**Supplementary Figure 5. Inhibition of ARF-GAPS or ARF-GEFs with small molecules decreases or increases VE-cadherin cell-surface localization respectively.**

**(a)** Quantification of plasma membrane VE-cadherin as shown in Figure 3c. **(b)** Transendothelial resistance was measured by ECIS in HMVEC-D cells treated with DMSO or QS11. **(c)** HMVEC-D, Human retinal endothelial cells (HREC), and Human umbilical vein endothelial cells (HUVEC) were analyzed by quantitative RT-PCR for ARF-GEF, CYTH, IQSEC and EFA6 family gene expression. **(d)** HMVEC-D cells stimulated with DMSO or SecinH3 were subjected to immunofluorescence for VE-cadherin (green). **(e)** Quantification of (d). **(f)** VE-cadherin membrane fraction after treatment with SecinH3 or DMSO control. **(g)** Transendothelial resistance was measured in HMVEC-D cells stimulated with IL-1β in the presence of DMSO or SecinH3 by ECIS. **(h)** Quantification of Figure 2g. For all experiments, N ≥ 3, and error bars represent SEM. * p<0.05, ** p<0.01, *** p<0.001, **** p<0.0001.

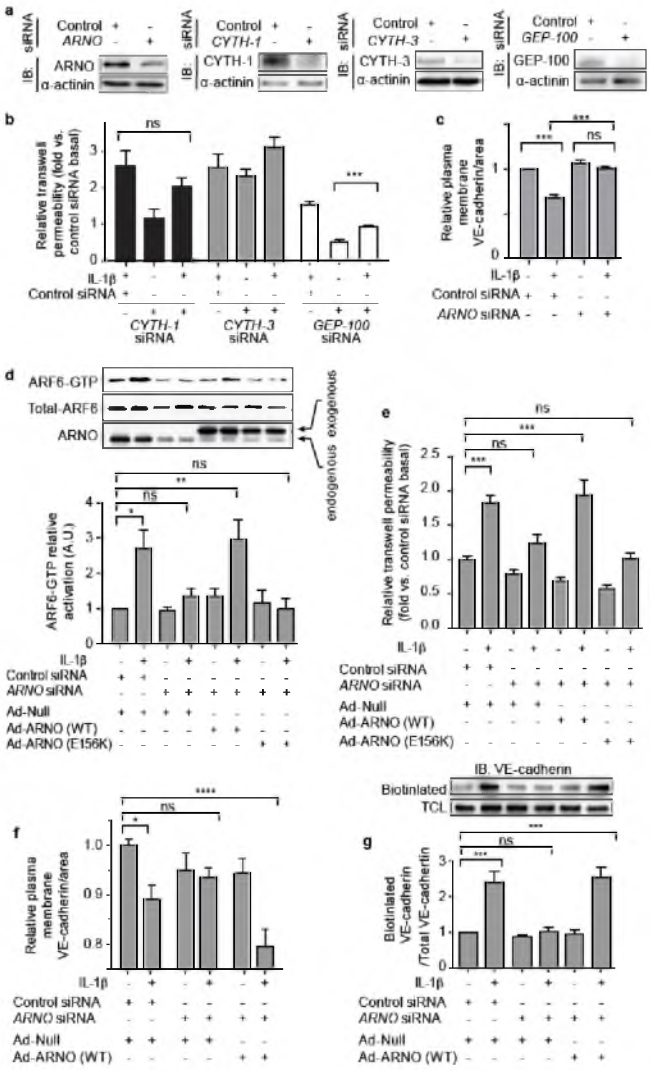


**Supplementary Figure 6. The ARF-GEF ARNO/Cytohesin-2 is critical for modulating IL-1β-induced VE-cadherin localization.**

**(a)** Lysates from HMVEC-D cells transfected with *Cytohesin-1, ARNO, Cytohesin-3, GEP-100* or control siRNA were immunoblotted for Cytohesin-1, ARNO, Cytohesin-3, or GEP-100. **(b)** Transwell permeability of *Cytohesin-1, Cytohesin-3, GEP-100* or control siRNA treated HMVEC-D stimulated with IL-1β for 2 hours. We show that loss of cytohesin-1 or cyothesin-3 have no effect in IL-1β induced permeability. Additionally, while loss of GEP-100 decreases baseline permeability, there is no effect on the fold increase in IL-1β induced permeability, suggesting that GEP-100 is regulating permeability independent of an IL-1β pathway. **(c)** Quantification of Figure 2k. **(d)** HMVEC-D treated with *ARNO* or control siRNA were stimulated with IL-1β in the presence or absence of Ad-ARNO-MYC or Ad-Null then assayed by GTP-ARF6 pulldown and immunoblotted with ARF6 antibodies. **(e)** HMVEC-D treated with *ARNO* or control siRNA were infected with Ad-Null or *ARNO* siRNA resistant Ad-ARNO-MYC, then stimulated with IL-1β and assayed by transwell permeability assay. **(f)** Quantification of cell-surface VE-cadherin in HMVEC-D treated with *ARNO* or control siRNA and infected with Ad-Null or *ARNO* siRNA resistant Ad-ARNO-MYC, then stimulated with IL-1β as in (e). **(g)** Immunoblot for biotin-labeled internalized VE-cadherin after IL-1β stimulation in conditions described in (e) and (f). For all experiments, N ≥ 3, and error bars represent SEM. * p<0.05, ** p<0.01, *** p<0.001, **** p<0.0001.

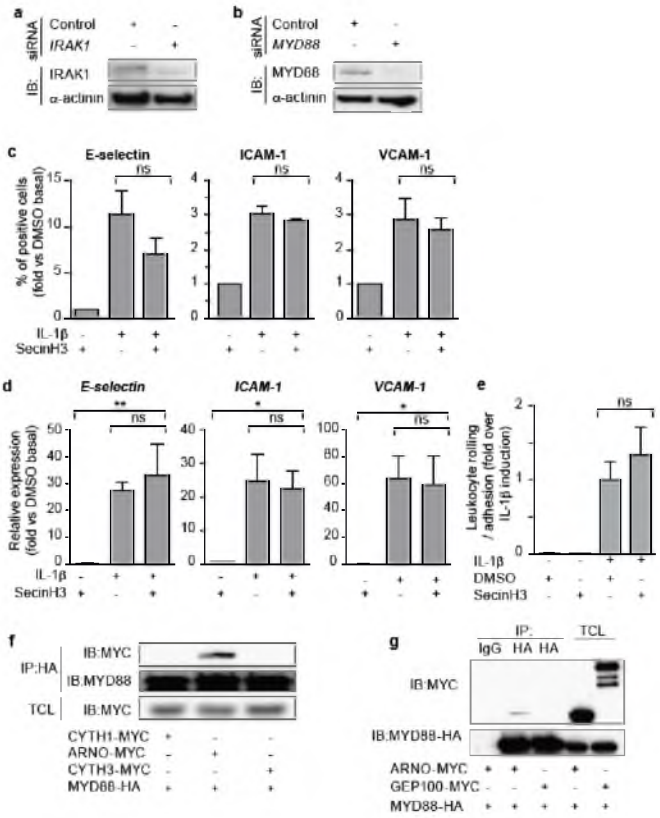


**Supplementary Figure 7. The IL-1β-induced permeability pathway diverges from the canonical NF-κB pathway at MYD88.**

**(a)** Lysates from HMVEC-D cells transfected with *IRAK1* or control siRNA were immunoblotted for IRAK1. **(b)** Lysates from HMVEC-D cells transfected with *MYD88* or control siRNA were immunoblotted for MYD88. **(c)** Fluorescence-activated cell sorting for E-selectin, ICAM-1 and VCAM-1 cell surface localization of HMVEC-D stimulated with IL-1β in the presence of DMSO or SecinH3. **(d)** Quantitative RT-PCR for *E-selectin*, *ICAM-1* and *VCAM-1* of HMVEC-D stimulated with IL-1β in the presence of DMSO or SecinH3. **(e)** Quantification of human polymorphonuclear leukocyte rolling and adherence to a HMVEC-D monolayer under shear stress conditions. **(f)**, **(g)** Lysates from HEK 293T cells expressing MYD88-HA and the indicated ARF-GEF-MYC constructs were immunoprecipitated with anti-HA antibodies and immunoblotted with anti-MYC antibodies. For all experiments, $N \geq 3$, and error bars represent SEM. * $p<0.05$, ** $p<0.01$, *** $p<0.001$, **** $p<0.0001$.

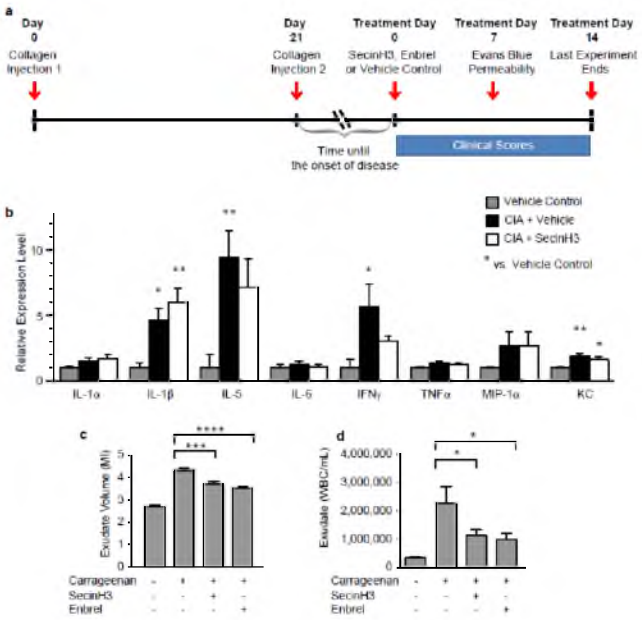


**Supplementary Figure 8. The effects of SecinH3 treatment in the collagen-induced arthritis and air-pouch models.**

**(a)** Timeline of the collagen-induced arthritis assay. Arthritis was induced by two collagen injections 21 days apart. Mice were segregated into pools and treatment with SecinH3, Enbrel, or Vehicle Control was initiated after the onset of disease. Evans Blue experiments were performed seven days after treatment initiation. Clinical scores were recorded daily from the day of treatment initiation until the experiment ended 14 days later. **(b)** Measurement of cytokine levels within arthritic joints 24 hours post treatment initiation. In an air-pouch model of acute inflammation, exudate volume **(c)**, as well as the white blood cell concentration **(d)** in the exudates was measured in the vehicle, SecinH3, or Enbrel-treated mouse six hours after inflammatory stimulus. Error bars represent SEM for 6-8 mice per group. * $p<0.05$, ** $p<0.01$, *** $p<0.001$, **** $p<0.0001$.

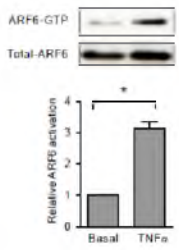


**Supplementary Figure 9. TNFα activates ARF6 in endothelial cells.**
HMVEC-D cells stimulated with TNFα were assayed by ARF6-GTP pull down assay and then immunoblotted with anti-ARF6 antibodies. Experiments, N=3, and error bars represent SEM. * $p<0.05$.

## METHODS

### Reagents

Human dermal microvascular endothelial cells (HMVEC-D) were purchased at passage 0 from Lonza and used at passages 2-6. SecinH3, ERK1/2 signal pathway inhibitor (U0126), P38 signal pathway inhibitor (SB203580), JNK signal pathway inhibitor (JNK Inhibitor II), and NF-κB signal pathway inhibitor (SC-514) were from Calbiochem. QS11 was from Sigma. Rabbit anti-VE-cadherin antibody, rabbit anti-MYD88 antibody (#3699 for western blot, #4283 for immunoprecipitation), rabbit anti-IRAK1 antibody, rabbit anti-p-ERK1/2, rabbit anti-p-P38, rabbit anti-p-JNK antibody, rabbit anti-ERK1/2, rabbit anti-P38 antibody, rabbit anti-JNK antibody and rabbit anti-NF-κB P65 antibody were from Cell Signaling. Mouse anti-ARF6 antibody was from Millipore. Mouse anti-ARNO antibody was from Abnova. *ARF6* siRNA, *ARNO* siRNA, *MYD88* siRNA and *IRAK1* siRNA were from Qiagen.

### Transfection and siRNAs

siRNAs were diluted in 12.5% HiPerFect Transfection Reagent (Qiagen) in Optimem (Invitrogen) and incubated 10-20 minutes at room temperature. As siRNAs were sitting, passage 3-4 HMVEC-D cells were passaged and resuspended in EGM2-MV (Endothelial Cell Basal medium-2 supplied with EGM®-2 MV SingleQuots®, Lonza) and combined with siRNAs such that the final concentration of siRNA was 30nM (all targets). The cells were plated, allowed to grow overnight and then the growth media was replaced. Three days after the initial transfection, the cells were transfected a second time using the same HiPerFect/siRNA concentrations as above.

The following is a table of all siRNAs used, their catalogue numbers, sequence, the location within the gene the siRNA targets, and average knockdown observed by western blot.

| Gene | Catalogue Number | Target sequence (5'-3') | Region | Mean knockdown |
|---|---|---|---|---|
| *ARF6* | SI02757286 | CAACGTGGAGACGGTGACTTA | exon | 77% |
| *ARNO* | SI00061299 | CACGCTGTTGGTAATCTTATT | 3' UTR | 63% |
| *Cytohesin-1* | SI04217185 | CGGGACAGAGGTTCCGGATAA | 3' UTR | 93% |
| *Cytohesin-3* | SI00061257 | CAGCATGTTGTGCTCGGACAA | 3' UTR | 99% |
| *MYD88* | SI00300909 | AACTGGAACAGACAAACTATC | exon | 87% |
| *IRAK1* | SI00605262 | CCGGGCAATTCAGTTTCTACA | exon | 83% |

**Protein expression constructs**

The coding sequence of full-length *MYD88* (BC023589), *ARNO* (BC038713), *CYTH-1* (BC038385), *CYTH-3* (BC028717) and *GEP100* (BC010267) were amplified by PCR from IMAGE cDNA clones and ligated into a **pcDNA3.1** vector after enzyme digestion. The ARNO, CYTH-1, CYTH-3 and GEP100 constructs contained both MYC and HIS epitopes, while the MYD88 construct contained an HA epitope.

**Subcellular fractionation**

Subcellular fractionation was performed as previously described[9]. Briefly, HMVEC-D cells were infected with adenovirus for 48 hours, stimulated with QS11 for 3 hours, or stimulated with SecinH3 for 2 hours. Alternatively, cells were transfected with siRNA as described above. The monolayer was washed two times with ice-cold phosphate-buffered saline (PBS) containing $Ca^{2+}$ and $Mg^{2+}$, and then washed a third time with HLB buffer [Tris-HCl 10mM at pH 7.4, KCl 5mM,

protease inhibitors (Roche) and phosphatase inhibitors (Sigma), and dithiothreitol 1mM]. After the third wash, cells were homogenized in a Dounce homogenizer using 20 strokes. The homogenate was then centrifuged at 400g for 10 minutes at 4°C. The supernatant was subjected to centrifugation again at 16,000g for 30 minutes at 4°C. The pellet was washed with HLB buffer and resuspended in radioimmunoprecipitation assay (RIPA) buffer for 30 minutes at 4°C. The resuspended pellet was centrifuged at 16,000g for 15 minutes at 4°C, and the supernatant was saved as a soluble membrane fraction. To obtain the total cell lysate, an aliquot of cellular material was set aside before Dounce homogenization. RIPA buffer was added to this aliquot and then the mixture was centrifuged at 13,000g for 10 minutes at 4°C. The resulting supernatant was saved for use as total cell lysate. Densitometry was performed on at least three independent experiments and data are presented as mean ± SEM.

**ARNO Rescue Experiment**

Cells ($1.0\times10^6$ in a 10 cm dish) were first transfected with *ARNO* siRNA (SI00061299, Qiagen) at 30nM and changed to fresh media 24 hours after the transfection. The siRNA was directed against sequences in the 3' UTR of the endogenous *ARNO* mRNA. 48 hours after the media change, cells were harvested and underwent a second transfection with the same siRNA at the same dose. Cells were then infected with either an Ad-ARNO (WT) or Ad-ARNO (E156K) virus ($5\times10^7$ p.f.u.ml$^{-1}$) 36 hours after the second siRNA transfection and incubated for 36 hours[2]. The adenoviral vectors expressing human ARNO (or mutant ARNO) fused to a MYC-epitope tag did not contain a 3'UTR *ARNO* sequence, and was thus predicted to be resistant to the siRNA.

**ARF6-GTP pull down assay**: ARF6-GTP pull-down assays were performed as described[21]. Briefly, HMVEC-D cells were pre-treated with SecinH3 for 3 hours followed by treatment with

10ng/mL IL-1β. Alternatively, cells were transfected with siRNA as described above. Cells were treated with IL-1β 72 hours after the second siRNA transfection for 5 minutes. After treatment, media was aspirated and cells were rinsed with chilled Ultrasaline. Dishes were frozen on dry ice. Following thawing, ARF6 pulldown lysis buffer [Tris-HCl 50mM, NaCl 100mM, $MgCl_2$ 1mM, NP-40 1%, glycerol 10%, protease inhibitors (Roche) and phosphatase inhibitors (Sigma)] were added to cells. Lysates were centrifuged and supernatants were added to GGA3-conjugated beads (Cell Biolabs, sta-40706), and agitated at 4°C for 60 minutes. Beads were washed in ARF6 pulldown lysis buffer and resuspended in 2X Laemmli prior to loading on 15% SDS-PAGE gels. A fraction of the cell lysate was withheld for use as a measure of total ARF6 in each sample. Data are presented as mean ± SEM of at least three independent experiments.

**Quantitative PCR**

Total RNA was extracted from cells using the RNeasy plus mini kit (Qiagen) according to manufacturer's instructions. RNA was converted to cDNA using RETROscript® kit (Ambion). Quantitative RT-PCR was performed using TaqMan probes (*CYTH1*, Hs00245092; *ARNO*, Hs00244669; *CYTH3*, Hs00188456; *CYTH4*, Hs00203581; *IQSEC1*, Hs00208333; *IQSEC2*, Hs00390333; *IQSEC3*, Hs01006522; *EFA6A*, Hs00160539; *EFA6B*, Hs00260268; *EFA6C*, Hs00209633; *EFA6D*,Hs00202892; *VEGFA*, Hs00900055; *ICAM1*, Hs00164932; *VCAM1*, Hs01003372; *IL-6*, Hs9999032; *TNFα*, Hs01113624_g1; *Cox2*, Hs00153133; *VE-cadherin*, Hs00901463; *E-selectin*, Hs00174057_m1) and the ABI Prism 7900 HT Real-Time PCR System (Applied Biosystems). Quantification was performed using a human brain cDNA standard curve and normalized to 18S rRNA. Data are presented as mean ± SEM of four duplicates from at least two independent experiments.

**Immunofluorescence**

10,000 HMVEC-D cells were seeded onto 8 well chamber slides coated with human fibronectin. Cells were pre-treated with small molecule inhibitors of NF-κB or MAPK for 30 minutes or SecinH3 for 3 hours followed by treatment with 10 ng/ml IL-1β for 2 hours. Alternatively, cells were infected with $1\times10^{5}$-$1\times10^{8}$ p.f.u.ml$^{-1}$ of the indicated adenovirus for 48 hours. For siRNA knockdown experiments, cells were harvested 72 hours after the first siRNA transfection, re-transfected with the same siRNA a second time and seeded onto chamber slides. 72 hours after the second siRNA transfection, cells were treated with IL-1β for 2 hours. Cells were fixed, permeabilized, blocked with normal donkey serum and stained for VE-cadherin or NF-κB p65. The only exception to this protocol was for Supplementary Fig. 6f, where permeabilization was not performed in order to increase the signal of cell-surface VE-cadherin. Images are maximum-Z-projections of confocal images acquired at 0.3 μm z-section intervals. Image acquisition settings were identical for all images. Images are representative of at least 3 independent experiments. Quantification was performed using a custom Image-J macro that imported images, applied a threshold to exclude all but intensely-stained areas, and returned this area as an output. Identical threshold and size restriction values were used to analyze all images. Data are presented as mean ± SEM of at least three independent experiments.

**Immunoprecipitation**

Immunopreciptation assays were performed as described[9]. Briefly, HMVEC-D cells were treated with 10 ng/ml IL-1β for 1 and 5 minutes. For Figure 3e, HMVEC-D cells were infected with $1 \times 10^{7}$ p.f.u.ml$^{-1}$ Ad Null or Ad-ARNO-MYC 48 hours before IL-1β treatment. Cells were then washed with ice-cold PBS and lysed with ice-cold lysis buffer (Tris-HCl 50 mM, NaCl

250mM, NP-40 1%, and glycerol 10% with protease inhibitors and phosphatase inhibitors). Cell lysates were centrifuged for 15 minutes at 13,000g and the supernatants saved. A BCA assay (Pierce) was used to determine protein concentrations. Lysates were incubated with 8 mg of the indicated antibody and protein A/G–Sepharose (Santa Cruz Biotechnology) for 1 hour at 4°C. Beads were then washed 5 times in lysis buffer. The immunoprecipitates were assayed by western blot analysis using Peroxidase-conjugated AffiniPure Light Chain Specific secondary antibody for signal detection. Data represents at least 3 independent experiments.

**Biotinylation Assay**

HMVEC-D cells were transfected with *ARNO* siRNA or control siRNA and then infected with Ad null or Ad-ARNO (as described), and grown to 100% confluence on 100-mm dishes. Cells were washed with ice-cold PBS three times and labeled with EZ-link Sulfo-NHS-SS-Biotin (Thermo) at 0.5mg/ml in PBS for 30 minutes on ice. Excess Biotin was removed by washing with glycine in PBS two times on ice. The cells were then incubated with 10 ng/ml IL-1β and 0.6 mM Primaquine (MP Biomedicals) at 37°C for 30 minutes; they were then exposed to GSH buffer (Glutathione 50mM, NaOH 75mM, NaCl 75mM, EDTA 1mM, BSA 0.1%, PH 9.0) on ice for 20 minutes to remove surface biotin. GSH was then quenched by washing with 5 mg/ml iodoacetamide in PBS. After an additional wash with ice-cold PBS, cells were lysed in NP-40 buffer (Tris-HCl 50 mM, NaCl 150 mM, MgCl2 1mM, NP-40 1%, Glycerol 10%) with a protease inhibitor cocktail on ice. Cell lysates were centrifuged at 14,000 rpm for 15 minutes and supernatant was incubated with High Capacity Streptavitin Agarose Resin (Thermo) for 60 minutes at 4°C. Beads were washed with NP-40 lysis buffer three times. Bound proteins were released in 2×Laemmli buffer with 5% β-mercaptoethanol at 95°C and internalized VE-cadherin analyzed by immunoblotting with VE-cadherin antibody.

**Transendothelial resistance**

Transendothelial resistance was measured by Electric Cell-substrate Impedance Sensing (ECIS). An 8W10E+ electrode culture array (Applied Biophysics) was coated with 10 µg/mL human fibronectin. 5 x $10^4$ HMVEC-D per well were seeded in complete media onto the electrode culture array and monitored until a stable monolayer formed. A stable monolayer was indicated by a capacitance <10 nF at 6.4 x $10^4$ Hz and a stable resistance over several hours at 4 x $10^3$ Hz. Cells were pre-treated with SecinH3/Avastin for 3 hours or MAPK/NF-κB inhibitors or Indomethacin or $PGE_2$ for 30 minutes followed by treatment with 10 ng/ml IL-1β (unless otherwise indicated). Alternatively, cells were infected with Ad-GFP or Ad-ARF6 (Q67L) adenoviruses. Resistance across the monolayer using alternating current at a frequency of 4 x $10^3$ Hz was measured by 40 electrodes per well (1000-2000 cells) using the ECIS-Zθ system (Applied Biophysics) and reported in Ohms or normalized to control treatment or initial resistance. Conditioned media was collected from cells undergoing ECIS (Supplemental Figure 2e) at 16 hours after treatment with IL-1β in the presence of DMSO or inhibitors. $PGE_2$ concentration was calculated using the $PGE_2$ Express EIA kit from Cayman Chemical (500141) according to manufacturer's instructions. Data are representative of at least 3 independent experiments or represented as mean ± SEM.

**Transwell permeability**

HMVEC-D cells were seeded on 1.0 µm Costar transwell inserts coated with fibronectin. Cells were grown to confluency and treated with SecinH3 for 3 hours or MAPK/NF-κB/transcription/translation inhibitors for 30 minutes followed by treatment with 10ng/ml IL-1β. Alternatively, cells were infected with Ad-GFP or Ad-ARF6 (Q67L) adenovirus for 48 hours.

siRNA knockdown was performed as described and cells were treated with IL-1β 72 hours after the second siRNA transfection. Two hours later, horseradish peroxidase (HRP) was added to the top chamber at a final concentration of 100μg/ml. Medium was removed after 60 minutes from the lower chamber. For time-course transwell assays and transcription/translation inhibitor experiments (Figure 1a, d), HRP was added to the insert at the same time as IL-1β. Transwell inserts were moved to fresh wells after each timepoint, and the concentration of HRP in the bottom chamber was measured for monolayer permeability. HRP was assessed using media samples obtained from the lower chamber incubated with 0.5 mM of guaiacol and 0.6 mM $H_2O_2$. Spectrophotometric analysis of absorbance at 490 nm provided a quantitative evaluation of the amount of HRP that crossed the membrane. Data are presented as mean ± SEM of at least three independent experiments performed in quadruplicate.

**Fluorescence-Activated Cell Sorting (FACS)**

FACS was performed as decribed[31]. HMVEC-D were pre-treated with SecinH3 for 3 hours and then stimulated with 10 ng/ml IL-1β for 4 hours. Analysis of the cell surface localization of adhesion molecules was performed with one step immunofluorescence staining using anti-hE-selectin-FITC, anti-hICAM1-FITC and anti-hVCAM1-PE antibody (BD). Data are presented as mean ± SEM of at least three independent experiments.

**Leukocyte Rolling and Adherence assay**

3 x $10^4$ HMVEC-D were seeded into each well of a fibronectin-coated parallel plate flow chamber (U-plate 0.4 VI Fibronectin, Ibidi GMBH). Media was changed daily using gentle aspiration until the cells had grown to confluence (approximately 3-5 days). Human polymorphonuclear leukocytes (PMNs) were isolated from whole blood according to previously

described protocols[32,33]. Briefly, human peripheral venous blood (500 mL) from healthy, medication-free, fasting adult subjects was drawn into acid-citrate-dextrose (1.4 mL ACD/8.6 mL blood) through standard venipuncture technique and used immediately upon collection. The University of Utah Institutional Review Board approved this study and all subjects provided informed consent. Blood was centrifuged at 150 x g for 20 minutes at 20°C to separate platelet-rich plasma (PRP) from red and white blood cells (RBC/WBC). The PRP was removed and the remaining RBC/WBC mixture was resuspended in 0.9% sterile saline back to the original volume. A volume equaled to half the original blood volume of 6% Dextran 70 (Sigma-Aldrich, St. Louis, MO) was then added to the RBC/WBC mixture and left for one hour. The leukocyte-rich supernatant was removed and centrifuged at 400 x g for five minutes a 4°C. The supernatant was then removed and the pellet resuspended (in 0.2% NaCl followed by an equal part of 1.6% NaCl), and the cells were centrifuged at 400 x g for five minutes at 4°C. After centrifugation, the cells were resuspended in Hank's Balance Salt Solution (Sigma-Aldrich, St. Louis, MO) with 1% human serum albumin (HBSS/A) (University of Utah Hospital, Salt Lake City, UT) and layered over an equal volume of Ficoll-Paque Plus (GE Healthcare Biosciences, Piscataway, NJ). The layered cells were then centrifuged for 30 minutes at 400 x g at 4°C. After 30 minutes, the mononuclear leukocyte layer was removed, followed by the RBC layer, HBSS/A layer, and Ficoll-Paque layer. The remaining pellet containing greater than 95% PMNs was washed with HBSS/A and resuspended to 1 x $10^6$ $ml^{-1}$ in warmed ultrasaline (Lonza). Endothelial cells in parallel-plate flow chambers were pretreated with IL-1β (10 ng/mL) and/or SecinH3 for 3 hours. A syringe pump (Harvard Apparatus) was used to flow the PMN solution through the parallel plate flow chambers at 1 dynes x $cm^{-1}$ (a typical venous shear stress). Differential Interference contrast microscopy (DIC) images were taken once per second using an Olympus inverted

microscope, and the total number of PMNs rolling and adhered in a 5 minute period were quantified using MetaMorph (Olympus) software. The data is presented as fold over IL-1β induced leukocyte rolling ± SEM and represents three independent experiments, each consisting of at least 3 replicates for each condition.

**Internalization assay**

VE-cadherin internalization assay was performed as previously described[9]. Briefly, HUVEC were transfected with siRNA as described above and seeded onto 8-well chambered coverglass at 5 x $10^4$ cells/coverglass. After 72 hours, the culture was chilled at 4°C for 30 minutes, surface-labeled for 60 minutes on ice with 1 ug/mL dialyzed anti-VE Cadherin antibody (clone BV6, Millipore) in ice-cold labeling buffer (3% BSA in MCDB131 medium, Invitrogen). At the end of 60 minutes, the labeling buffer was removed and the cells were treated with 0.6 mM Primaquine plus vehicle or 10 ng/mL IL-1β, DMSO vehicle or 30 μM SecinH3 or 50 μM SC-514 for 15 minutes at 37°C and 5% CO2. Monolayers were washed 3 times over 10 minutes with ice-cold HBSS (HBSS - Hank's Balanced Salt Solution, Invitrogen) + 50mM Glycine + 3% BSA, pH 2.7 to remove surface VE-cadherin. One well for each condition was washed in a neutral pH solution to retain surface VE-cadherin staining. Subsequently, monolayers were fixed immediately in 3% paraformaldehyde for 10 minutes. The VE-cadherin antibody was detected using an Alexa-Fluor 488 conjugated anti-Mouse IgG antibody and traditional immunofluorescence methods. To image the monolayers, five images per well were randomly selected using the DAPI channel at 600x. Z-series images were taken using a confocal Olympus FV1000IX81 microscope. Each treatment was done in triplicate. The assay score represents the average percentage of total cells in each image/well/treatment containing internalized VE-Cadherin.

**Collagen-induced arthritis**

Collagen-induced arthritis (CIA) studies were conducted by Washington Biotechnology using their standard procedures and DBA/1J mice as previously published[34-38]. All protocols were approved by their IACUC (Institutional Animal Care and Use Committee) prior to initiation of the study. Six to seven week old male DBA/1 mice were used (Jackson Laboratories) with 5-20 animals per group. Bovine type-II collagen (Chondrex) was dissolved in 0.01 M acetic acid, and an emulsion with 50 µl of Complete Freund's Adjuvant was injected at the base of the tail at Day 0. 21 days following the first injection, a booster injection consisting of a 50 µL emulsion of collagen in Incomplete Freund's Adjuvant was injected at the base of the tail. Arthritic index (AI) was scored for each limb of an animal as follows: 0 = no visible effects of arthritis, 1 = edema and erythema of one digit or joint, 2 = edema and erythema of two joints, 3 = edema and erythema of more than 2 joints, 4 = severe arthritis of the entire paw and digits accompanied by deformity of the limb. The score for each limb was summed, with 16 as the highest possible AI score for each animal. Treatments were either vehicle (0.5% DMSO/saline IP BID), SecinH3 (0.1 mg/kg IP BID), or the positive control, Enbrel® (10 mg/kg SC OD). The experiment was repeated multiple times with different endpoints; detailed descriptions of the exact timing for each experiment follow. In all cases, treatment was initiated after mild arthritis was established (therapeutic treatment).

EVAN's BLUE DYE EXTRAVASATION: Treatment was initiated when the average arthritic index for each group was between 3.4 - 3.55 and all mice in each group demonstrated a positive arthritic index. Due to the variation in when each group reached an average arthritic index of 3.4 – 3.55, treatment initiation day varied from study day 28 (seven days after the second collagen injection) to study day 30 (nine days after the second collagen injection). The treatments lasted

for seven days until the mice were sacrificed for the Evan's Blue Dye Assay (described in detail in subsequent methods).

ARTHRITIS PROGRESSION: Treatment was initiated when the average arthritic index for each group was 3.1 and all mice in each group demonstrated a positive arthritic index. Due to the variation in when each group reached an average arthritic index of 3.1, treatment initiation day varied from study day 28 (seven days after the second collagen injection) to study day 29 (eight days after the second collagen injection). The treatments lasted for 13 days in all groups with arthritic index recorded regularly throughout.

HISTOPATHOLOGIC PATTERNS: Treatment was initiated when the average arthritic index for each group was between 3.1-3.2 and all mice in each group demonstrated a positive arthritic index. Due to the variation in when each group reached an average arthritic index of 3.1 - 3.2, treatment initiation day varied from study day 29 (eight days after the second collagen injection) to study day 33 (12 days after the second collagen injection). The treatments lasted for 14 days in all groups before joints were harvested for histology. Limbs were preserved in 10% neutral buffered formalin for histology. Limbs were decalcified in formic acid for 2-3 days, paraffin embedded, and 8 μm sections stained with toluidine blue. Arthritis severity was evaluated for inflammation, pannus, cartilage damage, and bone damage.

CYTOKINE EVALUATION: Treatment was initiated when the average arthritic index for each group was 3.4 and all mice in each group demonstrated a positive arthritic index. All groups reached an average arthritic index of 3.4 on day 34 (13 days after the second collagen injection), and treatment was initiated. The treatments lasted for 1 day, at which time plasma and ankle joints were collected for cytokine analysis (described in detail in subsequent methods).

All selection and later scoring were blinded to treatment. Data are represented as mean ± SEM.

**CIA - Cytokine or chemokine array**

CIA was induced as described. 24 hours after treatment of SecinH3, joints of mice were collected and pulverized using a mortar and pestle filled with liquid nitrogen. Tissue was transferred to 15 ml tubes, resuspended in 1 ml PBS and homogenized using a Polytron tissue homogenizer (*PRO* Scientific Inc. USA) for 20 s. Mouse joint homogenates were centrifuged for 10 minutes at 500 g at 4°C. Supernatants were transferred to 1.5 ml Eppendorf tubes, centrifuged at 15,000 g for 5 minutes and collected for cytokine analysis by Quansys Biosciences. Data are presented as mean ± SEM for 6 mice per condition.

**CIA – Evans Blue permeability**

CIA was induced as described. Seven days after randomization and treatment initiation, mice were given an IV injection of 5 ml/kg of 1% Evans Blue dye. One hour later, mice were bled and plasma collected. Mice were perfused, the hind limbs degloved, and ankle joints homogenized in 0.5 ml saline. 1.5 ml formamide was added and Evans Blue dye eluted overnight at 60°C. Supernatant and plasma samples were read spectrophotometrically and expressed as OD620-OD740 joints divided by OD620-OD740 plasma. Values were normalized to non-CIA-induced mice and expressed as fold increase over control. N=14 per group and data are represented as mean ± SEM.

**Air-Pouch Model**

The Carrageenan-induced Air Pouch Model was performed by Washington Biotechnology as previously described[39-41]. All protocols were approved by their IACUC (Institutional Animal

Care and Use Committee) prior to initiation of the study. Six to seven week old male Swiss-Webster mice were used (Harlan) with 6-8 animals per group. On day 0, the nape of the neck was shaved and six mL of sterile air was injected subcutaneously. On day 3, three mL of sterile air was injected subcutaneously. On days 4 and 5, mice that were to be induced at a later time were injected with either 0.1 mg/kg SecinH3 IP BID, vehicle IP BID, or 10 mg/kg Enbrel® SQ QD. On day 6 an additional injection was administered one hour prior to carrageenan injection. One mL of 3% carrageenan (FLUKA) previously prepared in de-ionized water with heat, or 1mL of saline for the sham group, was then injected into the air pouch. Four hours after carrageenan injection, the mice were anesthetized and 3mL of 10 U/mL heparinized saline was injected into the air pouch. The air pouch was gently massaged, the contents immediately removed, and the exudate volumes recorded. An aliquot of the exudate was transferred to heparin-treated microtainer tubes for differential white blood cell counting. Samples with bloody exudates were discarded from white blood cell counting.

**Statistical analysis**

For the majority of data, one-way ANOVA (analysis of variance) with Tukey's post-hoc test was used to assess statistical significance. A Student's t-test was used when the experiment was only composed of two groups. Two-way ANOVA with Bonferroni post-hoc test was used to assess statistical significance for data shown in Figure 4b. A *P*-value of less than 0.05 was considered statistically significant. Unless otherwise noted, P-values of less than 0.05 are denoted with a single symbol (ie. *); P-values less than 0.01 are denoted with two symbols (ie **); P-values less than 0.001 are denoted with three symbols (ie ***); P-values less than 0.0001 are denoted with four symbols (ie ****), etc.

**Methods References**


31 Jones, C.A. *et al.* Robo4 stabilizes the vascular network by inhibiting pathologic angiogenesis and endothelial hyperpermeability. *Nature Medicine* **14**, 448-453 (2008).

32 Zimmerman, G.A., McIntyre, T.M., & Prescott, S.M. Thrombin stimulates the adherence of neutrophils to human endothelial cells in vitro. *J. Clin Invest* **76**, 2235-2246, (1985)

33 Yost, C.C. *et al.* Activated polymorphonuclear leukocytes rapidly synthesize terinoic acid receptor-alpha: a mechanism for transltional control of transcriptional events. *J Exp Med* **200**, 671-680, (2004).

34 Zimmerman, D.H. *et al.* Cel-2000: A therapeutic vaccine for rheumatoid arthritis arrests disease development and alters serum cytokine/chemokine patterns in the bovine collagen type II induced arthritis in the DBA mouse model. *Int immunopharmacol* **10**. 412-421, (2010).

35 Zalevsky, J. *et al.* Dominant-negative inhibitors of soluble TNF attenuate experimental arthritis without suppressing innate immunity to infection. *J Immunol* **179**, 1872-1883, (2007).

36 Konda, V. R., Desai, A., Darland, G., Bland, J. S. & Tripp, M. L. META060 inhibits osteoclastogenesis and matrix metalloproteinases in vitro and reduces bone and cartilage degradation in a mouse model of rheumatoid arthritis. *Arthritis Rheum* **62**, 1683-1692, (2010).

37 Miner, J. N. *et al.* Antiinflammatory glucocorticoid receptor ligand with reduced side effects exhibits an altered protein-protein interaction profile. *Proceedings of the National Academy of Sciences of the United States of America* **104**, 19244-19249, (2007).

38 Montalban, A. G. *et al.* KR-003048, a potent, orally active inhibitor of p38 mitogen-activated protein kinase. *Eur J Pharmacol* **632**, 93-102, (2010).

39 Colville-Nash, P. & Lawrence, T. Air-pouch models of inflammation and modifications for the study of granuloma-mediated cartilage degradation. *Methods Mol Biol* **225**, 181-189, (2003).

40 Cronstein, B. N., Montesinos, M. C. & Weissmann, G. Salicylates and sulfasalazine, but not glucocorticoids, inhibit leukocyte accumulation by an adenosine-dependent mechanism that is independent of inhibition of prostaglandin synthesis and p105 of NFkappaB. *Proceedings of the National Academy of Sciences of the United States of America* **96**, 6377-6381 (1999).

41 Edwards, J. C., Sedgwick. A. D. & Willoughby, D. A. The formation of a structure with the features of synovial lining by subcutaneous injection of air: an in vivo tissue culture system. *J Pathol* **134**, 147-156, (1981).

# CHAPTER 3

## ARF6 PROMOTES ATHEROSCLEROSIS THROUGH MEDIATION OF ENDOTHELIAL MECHANOTRANSDUCTION

Atherosclerosis is the leading cause of death in developed nations, including the United States[1]. Since the 1980s, research has shown that the rheological properties of the vascular system play an important role in the pathophysiology of atherosclerosis[2]. While a variety of mechanical forces (including hydrostatic pressure and cyclic-stretch) have been shown to affect Endothelial Cell (EC) structure and function, shear stress has the most drastic and well-characterized effect. Laminar blood flow resulting in high net shear stress (blood flowing with little turbulence in a constant direction) has been found to be atheroprotective, while low net shear stress or oscillatory shear stress (blood flowing with rapid changes in direction or turbulence) has been shown to promote atherosclerosis[3]. Mechanosensitive cellular components are specifically activated by large rapid changes in shear stress both *in vitro* and *in vivo* [4]. Disturbed flow has been shown to increase inflammation, cytokine release, and permeability of ECs *in vitro,* as well as inflammation and permeability *in vivo*. The activation or quiescence of the endothelium is thus determined by local shear stress patterns, as shown in Figure 3.1.

ECs sense and respond to shear stress through a variety of effectors, including ion channels [5], integrins [6], membrane-bound G proteins [7], the apical glycocalyx [8], primary cilia [9], and the VEGFR2/VE-Cadherin/PECAM-1 mechanosensory complex [10,11]. While a variety of EC mechanotransduction mechanisms have been proposed, and several molecules have been shown to respond directly to shear stress, a comprehensive understanding of the interaction of each pathway has not been elucidated. Generally, it is proposed that fluid shear stress induces deformation of the apical surface of ECs and/or their glycocalyx, and that this deformation results in either direct activation of apical cell components or the

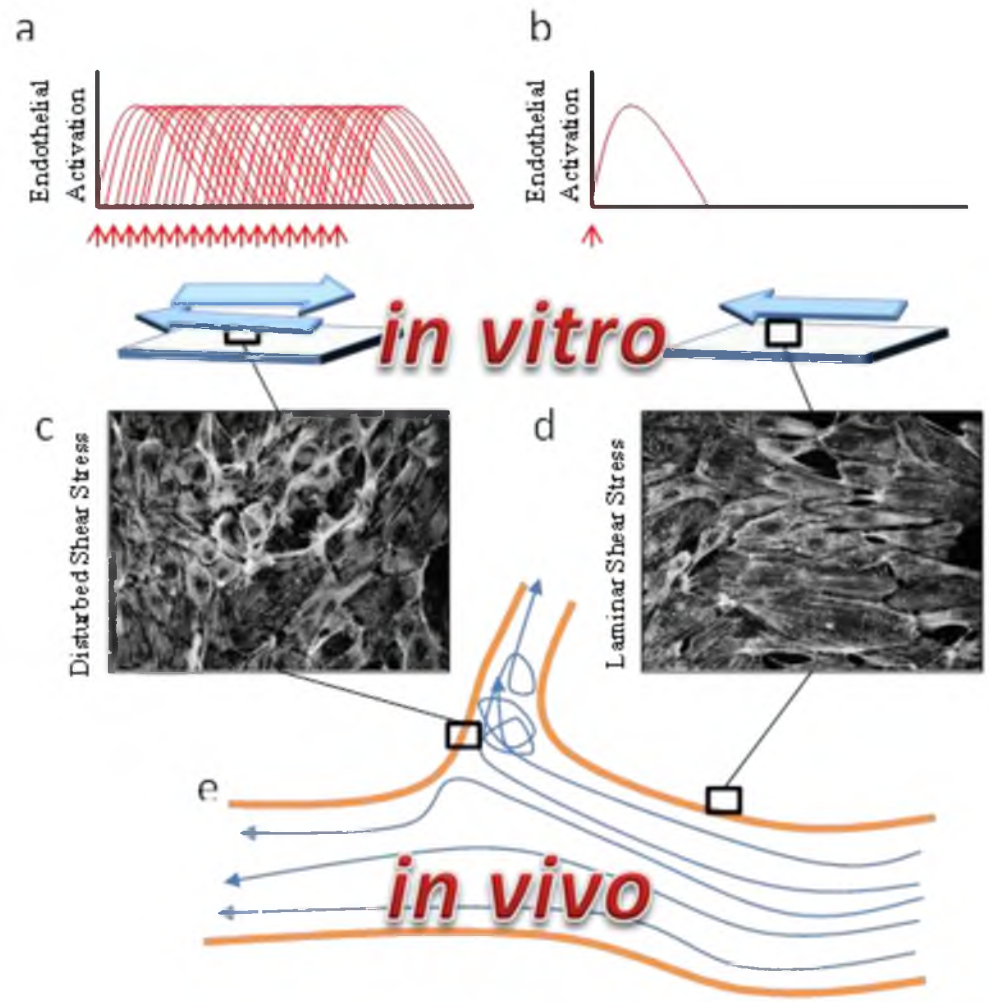


**Figure 3.1.** Rapid changes in fluid shear stress, as shown for oscillatory flow (a) and the onset of laminar flow (b) cause activation of endothelial cells. Endothelial cells exposed *in vitro* to low net-shear stress or rapidly reversing shear stresses do not align to the direction of flow (c) and express a sustained and marked increase in inflammatory and thrombotic markers. In contrast, the onset of steady or pulsatile laminar flow (b) induces transient endothelial activation, but as the cells adapt and align parallel to the direction of flow (d), the expression of inflammatory and thrombotic molecules decreases. *In vivo* (e), arterial regions distinguished by regular laminar flow are associated with a quiescent endothelial cell phenotype and low vessel-wall permeability. On the other hand, regions of disturbed flow show increased inflammation and monolayer permeability which are consistent with a pro-atherosclerotic phenotype and may play a role in the earliest stages of plaque formation.

transduction of force throughout the cell via the cytoskeleton, resulting in the activation of additional components, including integrins on the basal surface. There is widespread agreement that shear stress leads to the downstream activation of a variety of pathways, including Rac, Rho, and MAPK, and further downstream ERK, JNK, NF-kB activation, and actin remodeling [12]. All shear stresses are not equal, however; laminar flow, for example, induces ERK5 and subsequently, kruppel-like factor 2 (KLF2), which is known to establish quiescence in the endothelium[13], while in regions of disturbed flow, constant activation of the MAPK pathways leads to expression of monocyte chemotactic protein-1 (MCP-1) as well as leukocyte adhesion molecules such as intercellular adhesion molecule 1 (ICAM1) [14,15].

ECs of virtually any type will align parallel to constant or pulsatile flow (both whole-cell alignment and alignment of actin fibers) after 16-24 hours of arterial shear stress (10-20 dynes/cm$^2$). Cells cultured under static conditions, however, will show random orientation of actin fibers and no trend in whole-cell alignment. The alignment of cells to fluid shear stress is believed to be an adaptive mechanism to minimize the mechanical forces on the cells[6]. A lack of EC alignment when exposed to constant or pulsatile arterial shear stress indicates a possible modulation of EC mechanotransduction. EC alignment (both actin and whole-cell) parallel to flow is therefore a functional outcome and measure of an intact EC mechanotransduction system.

Despite data characterizing the critical role of disturbed flow on atherosclerosis, little work has been described that seeks to modulate these effects. The presence of regions of disturbed flow cannot be changed, as remodeling or replacement of the entire vascular system is impractical, and the requirement for blood throughout the body necessitates twists, turns, and bifurcations which induce disturbed flow. Therefore, one strategy could be to induce vascular stability by manipulating the ability of ECs to sense and respond to disturbed flow. This has proven to be a viable option, as demonstrated by the lab of Martin Schwartz, which identified PECAM-1 as a component of a mechanosensory complex which promoted vascular destabilization by disturbed flow[6]. By knocking out PECAM-1, the group showed that they had blunted EC mechanotransduction, and subsequently showed a significant decrease in atherosclerotic plaque formation in a PECAM-1$^{-/-}$; Apo-E$^{-/-}$ mouse compared to PECAM-1$^{+/+}$; Apo-E$^{-/-}$ mice [16]. Additionally, they showed that this strategy markedly decreased NF-kB activation both *in vitro* and *in vivo*. This important work highlights the potential for manipulation of EC mechanotransduction as a strategy for combating

atherosclerosis. Despite the promise of this work, PECAM-1 plays a critical role in a variety of physiologic processes, and inhibition could lead to increased susceptibility to certain permeability-related insults[17]. An ideal target in this pathway, therefore, would be a ligand-receptor-mediated pathway that blunts the deleterious effects of EC mechanotransduction while simultaneously supporting general vascular stability.

Slit2 is a repulsive neural guidance cue that has been implicated in a variety of processes in the vascular system, and specifically has been shown to effect vascular stability. While there is increasing data on the role of Slit2, its receptor and mechanism remain highly controversial. Our lab has proposed that Slit2 acts through the Robo4 receptor, a vascular-specific Roundabout receptor, and acts to inhibit Arf6 activity[18-20]. The proposed Slit2/Robo4 pathway includes recruitment of paxillin to Robo4 and inhibition of the downstream pathways of VEGFR2 and integrin activation. Paxillin plays an important role in focal adhesion formation, a process required for EC alignment to flow[21]. VEGFR2 downstream signals are also required for EC responses to fluid shear stress[11]. The core of the Slit2/Robo4 pathway is ARF6, a small GTPase shown to play a prominent role in cytokine-induced inflammation in the previous chapter.

The possibility that both cytokine-induced inflammation and shear stress-induced inflammation and endothelial activation converge through a single node, ARF6, is exciting. Current athersclerosis therapy includes lifestyle modification, cholesterol lowering drugs (such as statins), hypertension medication, antiplatelet and anticoagulant medication (such as aspirin or clopidogrel), and medical treatment of conditions which increase atherosclerotic risk such as diabetes. All of these strategies act indirectly on atherosclerosis. This study seeks to address a risk factor for atherosclerosis which underlies the pathophysiology of plaque formation due to both oscillatory shear stress and inflamation, and is universal to all humans regardless of race or health.

## Results

Using a parallel plate flow-chamber system [22], I have been able to induce alignment of actin filaments and whole-cells to flow in multiple human cell types, including Human Umbilical Vein Endothelial Cells (HUVEC), Human Dermal Micro-Vascular Endothelial Cells (HMVEC-D), and Human Coronary Artery Endothelial Cells (HCAECs). Cells were grown on fibronectin-coated slides and exposed to constant fluid shear stress of 12 dynes/cm$^2$ (a physiologically relevant arterial shear stress) for 16-24

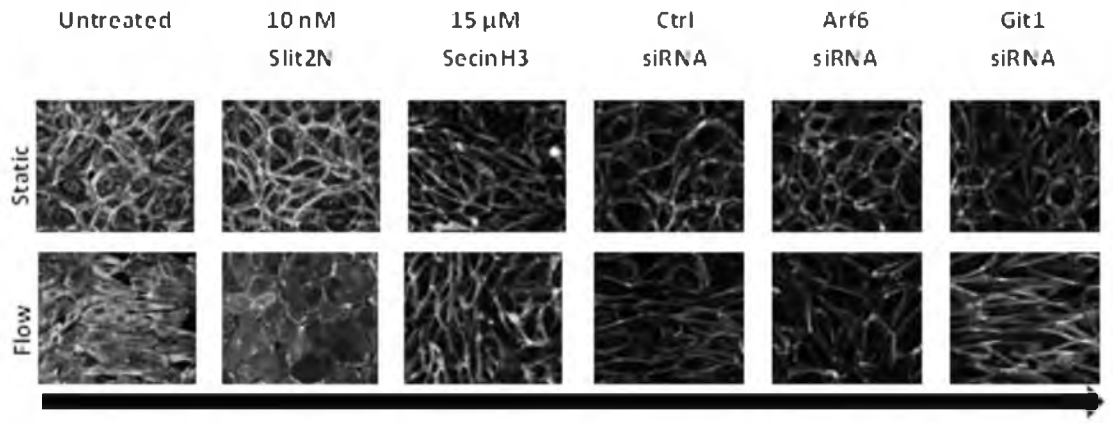


**Figure 3.2.** Effects of various treatments on flow-induced endothelial alignment.

hours. I also have shown random alignment of actin filaments and whole cells similarly prepared but exposed only to static conditions. Whole cell alignment was measured manually, and actin alignment was measured both manually and using a custom software program I developed (detailed in Chapter 1, Figure 1.5).

I wondered what effect modulation of various components of the SLIT/ROBO/ARF pathway would have on the ability of endothelial cells to respond to shear stress by aligning in the direction of flow. To address this question, I first measured the alignment of endothelial cells to flow after treatment with Slit2N. I found that Slit2N decreases both whole cell and actin alignment to constant shear stress in HUVECS (Figure 3.2). Slit2N causes the effect across a dose-response of concentrations and in the context of a range of fibronectin concentrations, indicating that this response is not due to differences in exposed fibronectin concentrations. Further, a knockdown of Robo4 using siRNA partially inhibited the effect of Slit2N on decreasing endothelial alignment, suggesting that Robo4 is necessary for this interaction.

Next, I wondered whether inhibition of ARF6 using RNAi or small molecules would have an effect on endothelial alignment to flow. I found that knockdown of ARF6 or chemical inhibition of ARF6 using SecinH3 reduced the ability of the cells to align to flow. A similar effect was seen for the reduction of the ARF-GEF ARNO via RNAi treatment. Further, inhibition of the ARF-GAP GIT1 using RNAi resulted in enhanced alignment to flow. Taken together, these data suggest that activation of the SLIT/ROBO pathway, leading to inhibition of ARF6, plays a role in limiting the mechanosensation of endothelial cells to fluid shear stress or limits the ability of the cells to respond to mechanosensory cues.

To test whether inhibition of ARF6 plays a physiologically relevant role in atherosclerotic plaque formation, we used a partial carotid ligation model in mice with either both ARF6 alleles or with both ARF6 alleles knocked out in the endothelium. The partial carotid ligation procedure induces highly oscillatory flow in the left carotid artery while maintaining normal flow in the right carotid artery for comparison. All branches of the left carotid (with the exception of the superior thyroid artery) are ligated and the intended flow modulation is confirmed by ultrasound. To encourage lesion formation, mice were fed a high fat for 5 weeks prior to surgery and for 3 weeks after surgery. These mice were subsequently sacrificed, and plaque formation was quantified in both genotypes. We found that loss of endothelial ARF6 reduced plaque formation and neointimal hyperplasia in response to left carotid ligation and subsequent oscillatory flow (Figure 3.3).

## Conclusions

These data strongly suggest that ARF6 plays a role in promoting endothelial activation in response to dynamic shear stress. Whether this effect is through inhibition of mechanotransduction or through inhibition of other inflammatory pathways remains an open question. Additional work is needed to fully validate these results, and studies are ongoing.

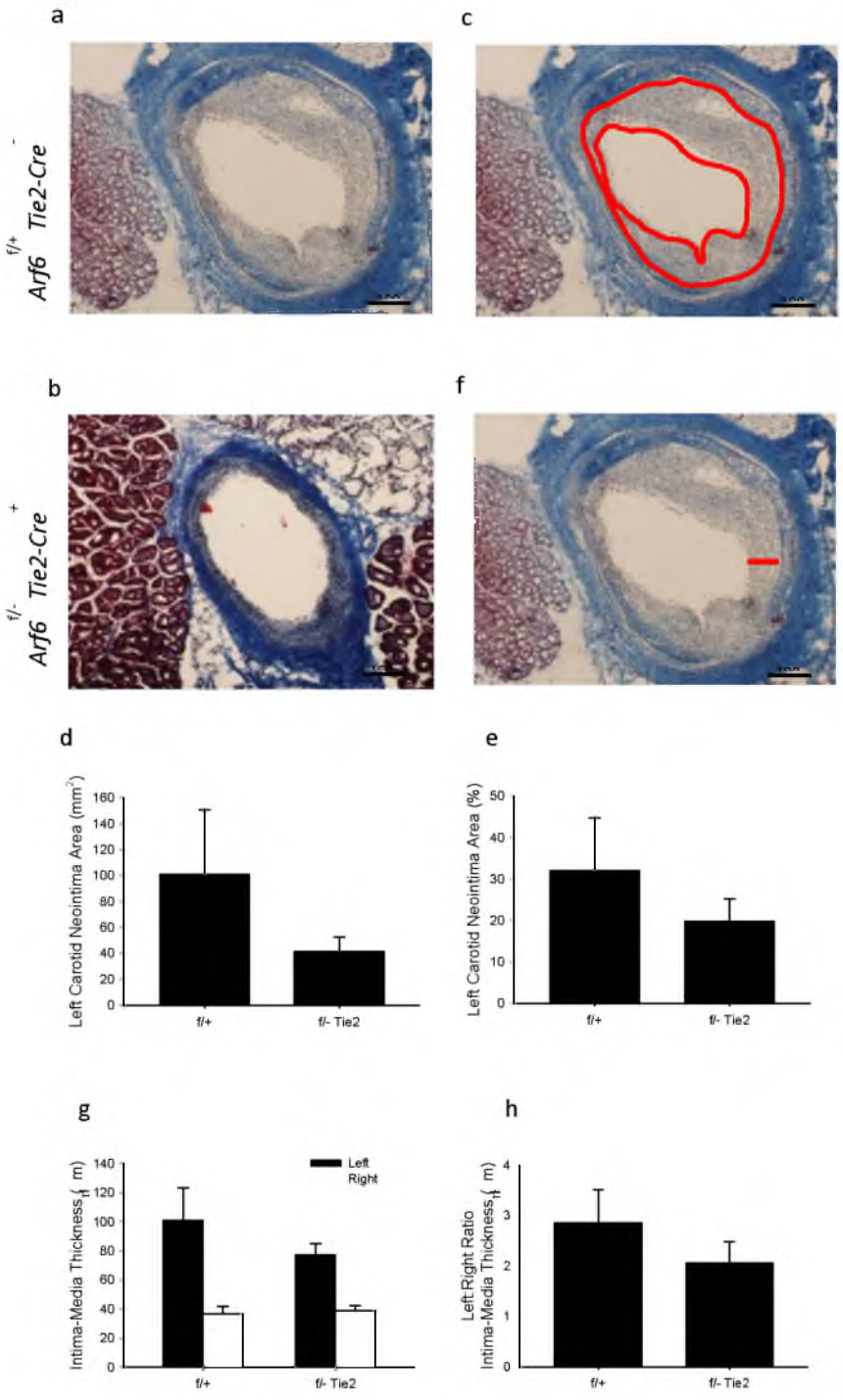


**Figure 3.3.** Representative left carotid artery from (a) wildtype and (b) endothelial-specific Arf6 knockout mice. (c) Method for quantifying neointima area. Comparison of neointima formation by (d) area and by (e) percentage. (f) Method for quantifying neointima thickness. Comparison of neointima thickness by (g) area and (h) ratio to healthy control vessel (right carotid)

# CHAPTER 4

## MUTATIONS IN 2 DISTINCT GENETIC PATHWAYS RESULT IN CEREBRAL CAVERNOUS MALFORMATIONS IN MICE

The following chapter was reprinted with permission from The Journal of Clinical Investigation. I was an author of this paper along with Aubrey C. Chan, Stavros G. Drakos, Oscar E. Ruiz, Alexander C.H. Smith, Jing Ling, Samuel F. Passi, Amber N. Stratman, Anastasia Sacharidou, M. Patricia Revelo, Allie H. Grossmann, Nikolaos A. Diakos, George E. Davis, Mark M. Metzstein, Kevin J. Whitehead, and Dean Y. Li. This article was originally published in The Journal of Clinical Investigation, 2011 May;121(5):1871-1881. This manuscript details the development of mouse models of cerebral cavernous malformation and the identification of these genes as critical in endothelial stability.

Research article

# Mutations in 2 distinct genetic pathways result in cerebral cavernous malformations in mice

Aubrey C. Chan,[1,2] Stavros G. Drakos,[1,3] Oscar E. Ruiz,[4] Alexandra C.H. Smith,[1,4] Christopher C. Gibson,[1,5] Jing Ling,[1] Samuel F. Passi,[1] Amber N. Stratman,[6] Anastasia Sacharidou,[6] M. Patricia Revelo,[7] Allie H. Grossmann,[1,7] Nikolaos A. Diakos,[1] George E. Davis,[6] Mark M. Metzstein,[4] Kevin J. Whitehead,[1,3] and Dean Y. Li[1,2,3,4]

[1]Molecular Medicine Program, [2]Department of Oncological Sciences, [3]Division of Cardiology, Department of Medicine, [4]Department of Human Genetics, and [5]Department of Bioengineering, University of Utah, Salt Lake City, Utah, USA. [6]Department of Medical Pharmacology and Physiology, School of Medicine, University of Missouri School of Medicine, Columbia, Missouri, USA. [7]Division of Anatomic Pathology, Department of Pathology, University of Utah, Salt Lake City, Utah, USA.

**Cerebral cavernous malformations (CCMs) are a common type of vascular malformation in the brain that are a major cause of hemorrhagic stroke. This condition has been independently linked to 3 separate genes: Krev1 interaction trapped (*KRIT1*), Cerebral cavernous malformation 2 (*CCM2*), and Programmed cell death 10 (*PDCD10*). Despite the commonality in disease pathology caused by mutations in these 3 genes, we found that the loss of *Pdcd10* results in significantly different developmental, cell biological, and signaling phenotypes from those seen in the absence of *Ccm2* and *Krit1*. PDCD10 bound to germinal center kinase III (GCKIII) family members, a subset of serine-threonine kinases, and facilitated lumen formation by endothelial cells both in vivo and in vitro. These findings suggest that CCM may be a common tissue manifestation of distinct mechanistic pathways. Nevertheless, loss of heterozygosity (LOH) for either *Pdcd10* or *Ccm2* resulted in CCMs in mice. The murine phenotype induced by loss of either protein reproduced all of the key clinical features observed in human patients with CCM, as determined by direct comparison with genotype-specific human surgical specimens. These results suggest that CCM may be more effectively treated by directing therapies based on the underlying genetic mutation rather than treating the condition as a single clinical entity.**

## Introduction

Cerebral cavernous malformations (CCMs) are common vascular malformations with a prevalence of 1 in 200 to 250 individuals in unselected populations (1, 2). CCMs can lead to focal neurological deficits, seizures, and hemorrhagic stroke, but no pharmacologic therapy currently exists (3). CCMs predominantly occur in the central nervous system and are characterized by subclinical bleeding and consequential hemosiderin deposits that are detected by MRI (4). MRI is the primary clinical modality for detection, diagnosis, and management of CCMs. Hemosiderin deposits give CCMs an MRI appearance of a central mass with a dark perilesional halo, whose appearance is nearly diagnostic (pathognomonic) of cavernous malformation (5). Cavernous malformations are characterized by a complex of vascular channels of varying sizes lined by a single layer of endothelial cells without any abnormally large arteries, arterialized veins, or large venous outflow vessels. Although dense fibrillary neuroglial tissue may penetrate the mass, vascular channels are generally arranged in a back-to-back pattern with little or no intervening brain parenchyma. There is often a peripheral margin of gliotic tissue containing hemosiderin-laden macrophages (6).

CCMs can occur sporadically or be inherited in an autosomal dominant pattern. Familial CCM has been linked to heterozygosity for any of 3 genes: Krev1 interaction trapped (*KRIT1*), Cerebral cavernous malformation 2 (*CCM2*), and Programmed cell death 10 (*PDCD10*) (7). All 3 proteins bind each other in coimmunoprecipitation experiments on cells overexpressing these proteins, leading to the hypothesis that they function as a complex to affect a common signaling mechanism (8). Both Krit1 and Ccm2 are required for proper connection of the developing heart with the aorta to establish circulation in the mouse embryo (9, 10). Mice lacking either Krit1 or Ccm2 fail to form a lumenized first branchial arch artery to link the heart and aorta; as a result, mice lacking either gene die at the same age. The requirement for Ccm2 is endothelial autonomous (9, 11). In the endothelium, both KRIT1 and CCM2 suppress the activity of the small GTPase RhoA (9, 12). Loss of either gene leads to RhoA activation and signaling through Rho kinase (ROCK) resulting in increased actin stress fibers, impaired cell-cell interactions, and increased vascular permeability (9, 12, 13). These defects can be reversed in cell culture and in mice with inhibitors of RhoA including HMG-CoA reductase inhibitors (statins) (9, 12).

A recent report suggested a similar mechanism of Rho activation for PDCD10 (14). However, other studies have suggested a different cell-signaling role for PDCD10. While KRIT1, CCM2, and PDCD10 all occupy the cytoplasmic compartment of the cell, unique subcellular localization for each has been described, including nuclear localization of KRIT1 (15) and Golgi localization of PDCD10 (16). Each protein has also been found to have unique binding partners (17–19). PDCD10's binding partners include members of the germinal center kinase III (GCKIII) subfamily of serine-threonine kinases with homology to yeast sterile-20 (STE20) kinase (16, 20–23). Furthermore, the clinical features of CCM in *KRIT1*, *CCM2*, and *PDCD10* families have important differences (24, 25), with *PDCD10* resulting in the most severe disease (24, 26). It is possible that CCM disease is the common result of multiple unique mechanisms and may require unique therapeutic strategies to target the underlying disturbed cellular and signaling pathways.

**Conflict of interest:** The University of Utah seeks to commercialize this technology and has filed patent applications related to this manuscript.

**Citation for this article:** *J Clin Invest.* 2011;121(5):1871–1881. doi:10.1172/JCI44393.

**Table 1**
Early growth arrest and death in embryos lacking *Pdcd10*

| Cross | *Pdcd10*$^{+/-}$ × *Pdcd10*$^{+/-}$ | | | |
|---|---|---|---|---|
| Genotype | *Pdcd10*$^{+/+}$ | *Pdcd10*$^{+/-}$ | *Pdcd10*$^{-/-}$ | Total litters |
| No. of progeny | | | | |
| E7.5 | 75 | 114 | 52 | 27 |
| E8.0 | 9 | 13 | 0[A] | 4 |
| E8.5 | 27 | 45 | 0[A] | 13 |
| E9.0 | 1 | 5 | 0 | 1 |
| >E9.0 | 7 | 8 | 0 | 3 |

The numbers of normal-appearing and viable offspring by genotype in matings between *Pdcd10*$^{+/-}$ parents are shown. [A]Ages at which growth-arrested embryos could be obtained.

Though the signaling and cellular mechanisms associated with the 3 known CCM proteins may be different, a common genetic mechanism of loss of heterozygosity (LOH) has been suggested for familial CCM disease (27–29). Familial CCM is more aggressive than sporadic disease, with an earlier age of onset, increased risk of hemorrhage and seizure, and an increased number of lesions (3, 30–32). These observations have led to the hypothesis that CCM disease occurs by the Knudson 2-hit mechanism, similar to retinoblastoma (33). There is limited evidence from human pathologic specimens to support an association of LOH with CCM lesions. In a series of challenging experiments, a number of investigators have identified biallelic mutations, 1 somatic and 1 germline, in the endothelium of a subset of patient samples (27, 28, 34). While LOH could not be confirmed for a number of samples, a total of 4 cases have been described for *KRIT1* and 1 case each for *CCM2* and *PDCD10*. Mice heterozygous for *Krit1* or *Ccm2* do not develop cavernous malformations, and no examples of secondary somatic mutations have been reported (35, 36).

To determine whether endothelial LOH is not simply associated with, but is causative for, CCM pathology, requires an animal model with a controlled genetic mutation that can be directed and detected in a tissue-specific manner. In this work, we use drug-inducible, tissue-specific strains of Cre recombinase to target conditional null alleles of the CCM genes to test directly the 2-hit hypothesis for cavernous malformations. We demonstrate that *Pdcd10* differs substantially from *Ccm2* in development, cell biology, and signaling, yet LOH is the common genetic mechanism to cause CCMs in both genotypes. These findings suggest that PDCD10 influences different endothelial signaling pathways from KRIT1/CCM2 to lead to a common histopathology and imply that medical treatment to stabilize familial CCM may need to be developed and evaluated in a genotype-specific manner.

## Results

*Loss of Pdcd10 results in embryonic lethal phenotypes distinct from loss of Krit1 or Ccm2.* To determine the role of *Pdcd10* in development and disease, we developed a conditional null allele, *Pdcd10*$^{flox}$, in which exons 4–8 are flanked with LoxP sites (Supplemental Figure 1; supplemental material available online with this article; doi:10.1172/JCI44393DS1). This strategy also allowed us to generate a constitutive null allele, *Pdcd10*$^{-}$, by crossing mice carrying *Pdcd10*$^{flox}$ with a mouse strain expressing Cre recombinase in the germline (37). To characterize the role of *Pdcd10* in development, we intercrossed *Pdcd10*$^{+/-}$ mice and harvested embryos at varying stages of development. Surprisingly, we found that mice lacking *Pdcd10* died at a much earlier age than those deficient for either *Krit1* or *Ccm2*. Whereas *Krit1* and *Ccm2* mice show growth arrest at E9.0 and die at E11 (9–11), the loss of *Pdcd10* leads to growth arrest at E8.0, after gastrulation, but prior to the onset of circulation or the requirement for cardiovascular function (Table 1 and Supplemental Figure 1).

An earlier requirement for *Pdcd10* than *Krit1* or *Ccm2* in development does not preclude a shared role in the vascular system. Mice with endothelial loss of *Ccm2* phenocopy the constitutive null mutant (9, 11), so we sought to determine whether mice with endothelial loss of *Pdcd10* would also recapitulate the *Ccm2* phenotype. Using the endothelial Tie2-Cre driver, the same Cre driver that we used to ablate *Ccm2* (9), we found that although mice with endothelial loss of *Pdcd10* (*Pdcd10*$^{flox/-}$;*Tie2-Cre*) did not survive to birth, they had patent branchial arch arteries, a developed circulatory system, and were indistinguishable from control littermates at E9.5 (Supplemental Figure 2). Instead, we found that loss of *Pdcd10* in the endothelium leads to progressive enlargement of the cardinal vein and other veins of the rostral embryo at E11.5 (Figure 1). Venous enlargement was not due to abnormal cardiac structure or function (Figure 1 and Supplemental Figure 2), nor were defects observed in arteries of the embryo (Figure 1 and Supplemental Figure 2). Death occurred due to hemorrhage from venous rupture by E13.5 (Table 2). Additionally, mice with loss of *Pdcd10* in neural and glial tissues induced by Nestin-Cre showed no vascular or any other obvious defects and were born alive (Supplemental Figure 2 and Supplemental Table 1). These observations suggest that *Pdcd10* is required in the endothelium for control of venous size and integrity, yet *Pdcd10* differs from *Ccm2* in that it is not required for the establishment of circulation.

*Loss of PDCD10 does not affect RhoA signaling but results in lumen formation defects.* To explore the role of PDCD10 in endothelial cells, we depleted *PDCD10* in human dermal microvascular endothelial cells (HMVEC) with siRNA (Supplemental Figure 3). Whereas the loss of CCM2 leads to an increase in actin stress fibers as a result of RhoA activation (9, 12, 13) and phosphorylation of myosin light chain-2 by Rho kinase (Figure 2), we observed none of these indicators of RhoA activation with the loss of PDCD10 (Figure 2). Thus, the role of PDCD10 in endothelial cell biology and signaling differs from that of CCM2.

Having found that PDCD10's function in development differs from that of CCM2, we sought to identify defects associated with PDCD10 depletion in assays relevant to vascular development. PDCD10-depleted HUVECs showed defective function in a 3D angiogenesis assay. Endothelial cells plated in a collagen matrix spontaneously organize into complex multicellular capillary-like networks with lumens (38), but cells depleted of PDCD10 failed to organize themselves into a lumenized network (Supplemental Figure 4, A and B). We explored potential downstream signaling pathways using this assay. A growing body of evidence suggests that PDCD10 interacts with the GCKIII subfamily of serine-threonine kinases (16, 21–23); we used siRNA to deplete cells of each of the subfamily members (Supplemental Figure 3). We observed no effect on lumen formation with the knockdown of STK25, STK24, or MST4 in HUVECs (Supplemental Figure 4C).

*Pdcd10 functionally associates with GCKIII in lumen formation.* Because the GCKIII family members may be functionally redundant, we sought to validate the importance of the PDCD10-GCKIII interaction in vivo and in a simpler genetic model. We chose the fruit fly, *Drosophila melanogaster*, in which the GCKIII family is represented by

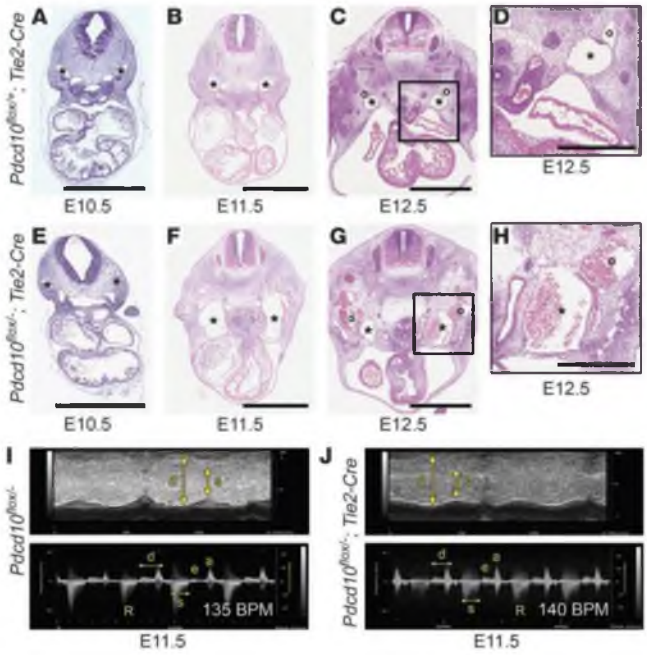


**Figure 1**
Pdcd10 is required in the endothelium for venous integrity. (**A**–**H**) H&E staining of developmental time course of *Pdcd10* endothelial knockout. *Pdcd10*$^{flox/+}$;*Tie2-Cre* is shown in **A**–**D**. *Pdcd10*$^{flox/-}$;*Tie2-Cre* is shown in **E**–**H**. Close-up images of the cardinal vein at E12.5 are shown in **D** and **H**. Asterisks denote the cardinal veins. Circles denote the external jugular veins. (**I** and **J**) Echocardiography of hearts from *Pdcd10*$^{flox/-}$ (**I**) and *Pdcd10*$^{flox/-}$;*Tie2-Cre* (**J**) mice at E11.5. Top panels show M-mode images of hearts contracting over time. Bottom panels show waveforms corresponding to blood flow across the atrioventricular valves. s, systole; d, diastole; e, early filling; a, atrial contraction; R, valvular regurgitation. Scale bars: 1 mm (**A**–**C** and **E**–**G**); 500 μm (**D** and **H**). $n \geq 6$ embryos at each age.

a single protein, GCKIII. This model avoids the complexity of human or mouse, which has 3 GCKIII kinases, or zebrafish, which has 2 orthologs for *Pdcd10*, 2 orthologs for *STK25*, and single orthologs for *STK24* and *MST4* (23). Furthermore, the *Drosophila* genome contains a single ortholog of *PDCD10*, but no orthologs for *KRIT1* or *CCM2*. Thus, *Drosophila* represents a simple model organism for studying Pdcd10-specific biology. To ensure that the biochemical interaction between PDCD10 and GCKIII was conserved in *Drosophila*, we performed immunoprecipitation assays with the *Drosophila* proteins. *Drosophila* Pdcd10 binds to GCKIII (Supplemental Figure 4D) in a manner analogous to that of human, mouse, or zebrafish protein (21, 23). A human disease PDCD10 mutation exists, which deletes 18 amino acids crucial for PDCD10-GCKIII binding (21). Removal of the analogous 18 amino acids from the *Drosophila* Pdcd10 protein abrogated binding to GCKIII (Supplemental Figure 4D).

Whereas *Drosophila* do not develop a vascular system, they do form a branched, lumenized network of tubes in the tracheal (respiratory) system. This epithelial network requires coordinated cell-cell interactions and specialized cell-cell junctions, analogous to the mammalian vascular system (39, 40). To determine the necessity of Pdcd10 in developing fly tracheal tubes, we expressed a dsRNA directed against *Pdcd10* (41) under the control of the tracheal-specific *Breathless* promoter (42) using the GAL4-UAS system (43). We found that tracheal tubes lacking Pdcd10 grow and branch normally, but fail to lumenize and fill with air (Supplemental Figure 5), indicating that Pdcd10 is required for normal lumen formation in fly tracheal tubes as it is in human endothelial tubes. This effect is highly penetrant; nearly all dsRNA-expressing flies show lack of lumenization in multiple tracheal tubes (Supplemental Figure 4E). The specificity of this effect is confirmed, as it could be rescued by coexpression of *Drosophila* Pdcd10 in RNAi-expressing cells (Supplemental Figure 4E). Notably, coexpression of the 18–amino acid deletion form of *Drosophila* Pdcd10, which does not bind to GCKIII, fails to rescue this phenotype (Supplemental Figure 4E). We used the same RNAi strategy to inactivate *GCKIII* (44) in the developing tracheal system. Tracheal tubes lacking GCKIII exhibit failure of lumenization (Supplemental Figure 5), and the phenotype appears very similar to that of Pdcd10-deficient tubes. Thus, Pdcd10 is essential for normal lumen formation in the absence of Krit1 and Ccm2 and in a manner that requires interaction with GCKIII kinases.

Our experiments in *Drosophila* suggested that GCKIII kinases are required for lumen formation but that functional redundancy in mammalian cells may have accounted for the lack of a lumen formation defect when any single kinase was lost. We therefore performed combinatorial knockdown experiments for pairs of the GCKIII kinases. Consistent with our hypothesis, we found that the loss of STK25, if coupled with the loss of either STK24 or MST4, was sufficient to reproduce the lumen formation defects seen with PDCD10 depletion (Supplemental Figure 4). Thus, PDCD10 interaction with GCKIII kinases is critical in lumen formation.

*LOH of either Pdcd10 or Ccm2 causes murine cavernous malformations that phenocopy human CCMs.* Pdcd10 and Ccm2's functions clearly differ in embryonic development, in endothelial cell culture, and in signaling, and Pdcd10 is necessary for lumen formation in a system that lacks Ccm2 or Krit1. The 3 genes, however, are linked

**Table 2**
Loss of *Pdcd10* in the endothelium leads to embryonic death after E12.5

| Cross | *Pdcd10*$^{flox/flox}$ × *Pdcd10*$^{+/-}$;*Tie2-Cre* | | | |
|---|---|---|---|---|
| Genotype | *Pdcd10*$^{flox/+}$ | *Pdcd10*$^{flox/-}$ | *Pdcd10*$^{flox/+}$;*Tie2-Cre* | *Pdcd10*$^{flox/-}$;*Tie2-Cre* |
| No. of progeny | | | | |
| E9.5 | 14 | 14 | 7 | 11 |
| E12.5 | 13 | 28 | 16 | 16 |
| E15.5 | 8 | 8 | 20 | 0 |
| P21 | 26 | 20 | 20 | 0 |

Live offspring by genotype at embryonic and postnatal time points resulting from matings between *Pdcd10*$^{flox/flox}$ and *Pdcd10*$^{+/-}$;*Tie2-Cre* parents.

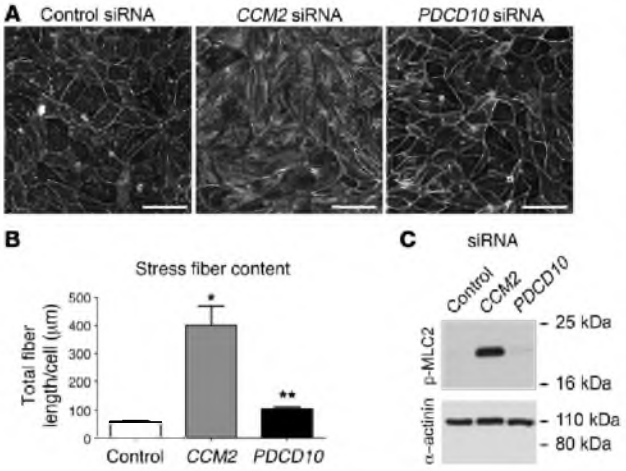


**Figure 2**
PDCD10 differs from CCM2 in downstream signaling. (**A**) Phalloidin staining of human microvascular endothelial cells treated with siRNA directed against *CCM2*, *PDCD10*, or nonsense control. (**B**) Quantification of stress fiber response of HMVEC cells. Stress fiber content is determined by adding the total length of stress fibers divided by the total number of cells. Results indicate mean ± SEM and are representative of at least 3 independent experiments. $^{*}P < 0.001$ versus control or *PDCD10*; $^{**}P$ = NS versus control. (**C**) Immunoblot for phospho-myosin light chain-2 (with α-actinin immunoblot as a loading control). Results are representative of 3 independent experiments. Scale bars: 100 μm.

to the same human disease. Limited human genetics suggested an association between LOH and CCM disease, so we investigated whether *Pdcd10* and *Ccm2* share this genetic mechanism for causing disease. To control the timing of the endothelial "second-hit," we used a drug-inducible Cre strain under the control of the *PDGF-B* promoter. This *PDGFb-iCreER*$^{T2}$ strain expresses a Cre recombinase activated only after administration of the drug tamoxifen. Consistent with the original report describing this recombinase (37), we found that the administration of tamoxifen on the first postnatal day (P1) led to efficient, endothelial-specific recombination throughout the entire brain vasculature (Supplemental Figure 6). The induction of endothelial LOH of either *Pdcd10* or *Ccm2* by this Cre at birth resulted in CCMs in mice as early as 1 month of age (Figure 3). Induction of endothelial LOH of either *Pdcd10* or *Ccm2* resulted in a spectrum of vascular malformations, from capillary telangiectasias, to isolated caverns, to multiple back-to-back caverns with thrombosis, hemorrhage, and formation of secondary channels (Supplemental Figure 7). Loss of protein product via LOH was confirmed by antibody staining (Supplemental Figure 8). The retinal vasculature is another location for human CCMs, and murine cavernous malformations were also observed in mouse retinal vasculature (Supplemental Figure 9). To formally prove LOH in the endothelium of these CCMs, we performed laser capture microdissection to obtain tissue-specific DNA as previously done in human studies of CCM (28). We found that DNA from lesion endothelium had lost the conditional allele for either *Pdcd10* or *Ccm2*, confirming LOH, whereas this allele could still be detected in adjacent neuronal tissue (Figure 3). In contrast, loss of *Ccm2* in neural tissues using Nestin-Cre did not result in the development of vascular malformations (Supplemental Figure 10).

We characterized the histopathologic features of cavernous malformations in mice with induced endothelial loss of either *Pdcd10* (Figure 4) or *Ccm2* (Figure 5). We compared mouse CCMs with surgical specimens from CCM patients with germline mutations of either *PDCD10* (Figure 4) or *CCM2* (Figure 5). Cavernous malformations in these induced mouse models share all of the key histologic features of CCM lesions with human specimens. Furthermore, both *Pdcd10* and *Ccm2* resulted in identical pathologic findings for all of these defining characteristics in both human and mouse (Table 3). Mouse specimens showed numerous

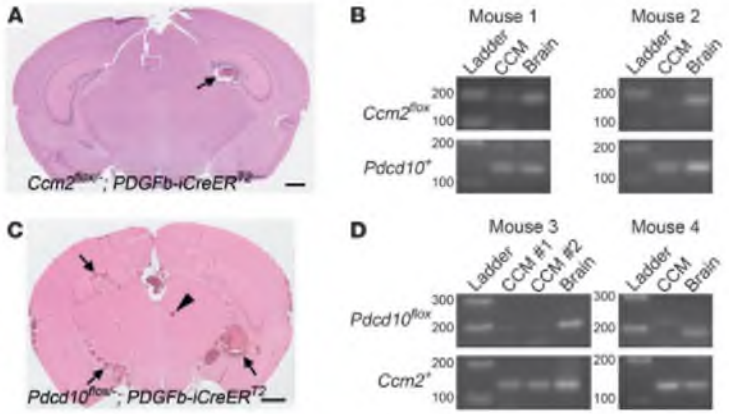


**Figure 3**
Cavernous malformations result from LOH of either *Ccm2* or *Pdcd10*. (**A**) Cavernous malformation (arrow) shown in an H&E-stained section of brain cerebrum from a mouse with induced endothelial knockout of *Ccm2*. (**B**) Confirmation of LOH of *Ccm2* in 2 mice with loss of *Ccm2*$^{flox}$ allele by PCR, compared with *Pdcd10* wild-type allele as a control. (**C**) Cavernous malformations (arrows) and a less complex telangiectasia (arrowhead) shown in an H&E-stained section of brain cerebrum from a mouse with induced endothelial knockout of *Pdcd10*. (**D**) Confirmation of LOH of *Pdcd10* in 2 mice by PCR with loss of *Pdcd10*$^{flox}$ allele compared with *Ccm2* wild-type allele as a control. Samples in **B** and **D** were obtained via laser capture microdissection of sectioned mouse brains. Scale bars: 1 mm.

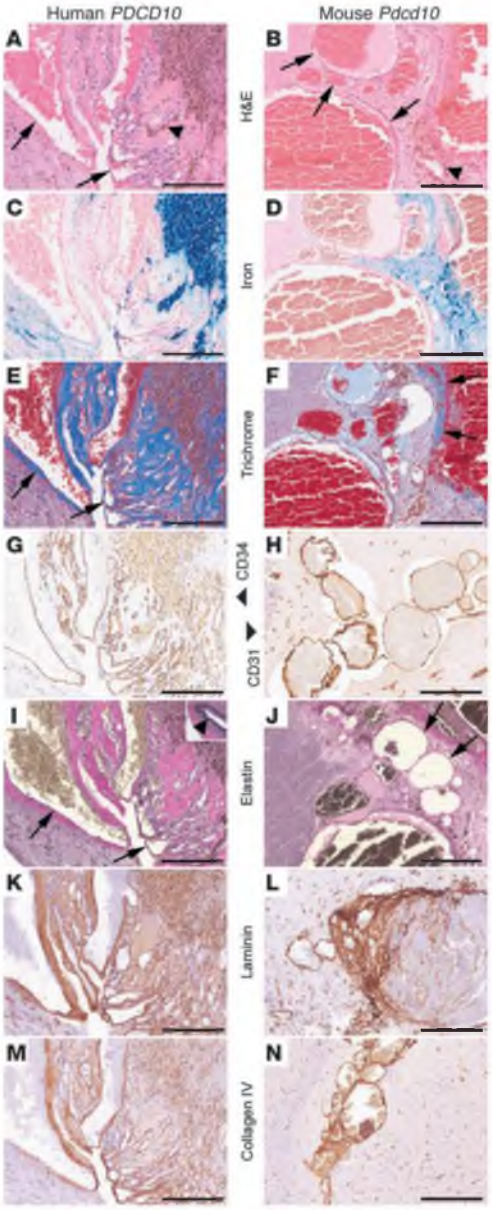


**Figure 4**
Pathologic analysis of mouse and human *PDCD10*-associated CCM. Paired analysis of histologic sections with human tissue on the left and mouse on the right. (**A** and **B**) H&E staining revealing back-to-back vascular channels (arrows) and hemosiderin pigment (arrowheads) in surrounding tissues. (**C** and **D**) Iron (blue) detected by Prussian blue stain highlights hemosiderin deposits in macrophages and surrounding brain tissue. (**E** and **F**) Fibrous matrix deposits (blue) identified by Masson's trichrome staining with fibrous tissue surrounding vascular channels (arrows) and in surrounding gliotic brain. (**G** and **H**) Endothelial staining for CD34 (**G**) or CD31 (**H**) is positive in the cells lining the channels. (**I** and **J**) Elastin staining shows that vascular channels lack elastic laminae (arrows) unlike normal vessels of similar caliber (arrowhead, inset in **I**). The fibrous matrix surrounding channels includes laminin (**K** and **L**) and collagen IV (**M** and **N**). Scale bars: 200 μm.

vascular channels of variable diameter (Figure 4, A and B, and Figure 5, A and B), some of them with organized thrombi. Immunohistochemical stains for endothelium highlighted endothelial cells in the channels, with focal attenuation or loss of endothelial cells in larger channels (Figure 4, G and H, and Figure 5, G and H). Iron stain highlighted the presence of hemosiderin-laden macrophages and hemosiderin in the wall of the channels as well as in the periphery and brain tissue (Figure 4, C and D, and Figure 5, C and D). Additionally, we also examined gliosis, trichrome staining, elastin, laminin, and collagen type IV, and these features were all identical between mouse and human lesions (Figure 4, E and N, Figure 5, E and N, and Table 3).

We also examined mouse lesions at the ultrastructural level using transmission electron microscopy. Murine cavernous malformations showed endothelial cells lining vascular channels with associated basal lamina (Figure 6A). Some of the larger channels showed segmental multilayering (lamellated appearance) of the basal lamina (Figure 6B). The most dilated channels showed focally marked attenuation of the endothelial cells (Figure 6C); however, tight junctions were identified between cells, and definitive gaps were not seen. Connective tissue composed mainly of collagen fibers separated the vascular channels (Figure 6D). Pericytes or astrocytic foot processes were missing, as seen in human lesions. Foci of mononuclear inflammatory cells were also seen (Figure 6E), including hemosiderin-laden macrophages (Figure 6F). Ultrastructural analysis of murine CCM lesions was similar to that described in human CCMs (45), further solidifying the fidelity of the mouse model to the human disease.

*Murine cavernous malformations can be detected and followed noninvasively by MRI.* MRI is used to document the natural history of human cavernous malformations and will be necessary for prospective therapeutic trials in both mice and humans. We thus employed monthly live MRI studies to follow the onset and progression of disease in mice until at least 6 months of age (Figure 7). As in humans (24), mice lacking *Pdcd10* had an earlier onset of disease, with a more severe phenotype than *Ccm2*. All *Pdcd10* mice studied at 1 month of age had lesions, whereas no *Ccm2* mice had yet developed lesions by 2 months of age (Figure 7K). Mice with *Pdcd10* mutations had a greater disease burden when assessed by total lesion burden (Figure 7L) or by number of complex lesions (increased signal intensity within the lesion; Figure 7M). Cavernous malformations were fully penetrant in mice with *Ccm2* LOH at 6 months of age and most had lesions at 4 months, at which time the disparity between the genotypes began to narrow. This parity reflected not only the increased burden of disease in *Ccm2*, but also the onset of death in the most severely affected *Pdcd10* mice. Mice of both genotypes began to die of hemorrhage, but mortality was greater in mice with LOH for *Pdcd10* (Figure 7N), a finding that reflects the reported experience in humans (24).

## Discussion

Although CCM has been associated with mutations in 3 distinct loci, it has been clinically treated as a single pathophysiologic entity. In this manuscript, we describe for what we believe is the first time the pathologic features of CCM in a genotype-specific manner. We

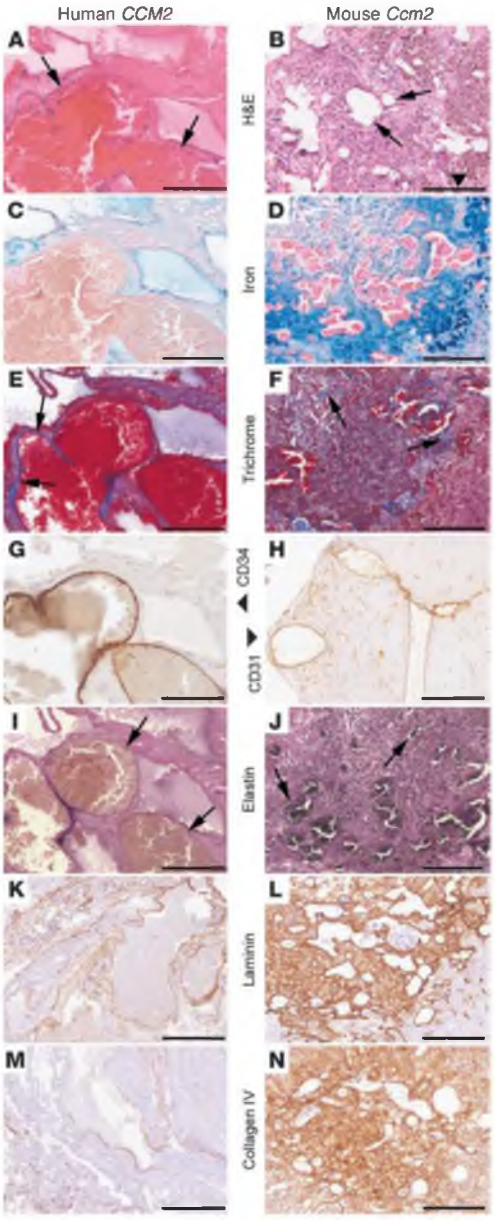


**Figure 5**
Pathologic analysis of mouse and human *CCM2*-associated CCM. Paired analysis of histologic sections with human tissue on the left and mouse on the right. (**A** and **B**) H&E staining revealing back-to-back vascular channels (arrows) and hemosiderin pigment (arrowhead) in surrounding tissues. (**C** and **D**) Iron (blue) detected by Prussian blue stain highlights hemosiderin deposits in macrophages and surrounding brain tissue. (**E** and **F**) Fibrous matrix deposits (blue) identified by Masson's trichrome staining with fibrous tissue surrounding vascular channels (arrows) and in surrounding gliotic brain. (**G** and **H**) Endothelial staining for CD34 (**G**) or CD31 (**H**) is positive in the cells lining the channels. (**I** and **J**) Elastin staining shows that vascular channels lack elastic laminae (arrows). The fibrous matrix surrounding channels includes laminin (**K** and **L**) and collagen IV (**M** and **N**). Scale bars: 200 μm.

find that mutations of both *PDCD10* and *CCM2* result in a common pathologic expression of disease in both humans and mice. Surprisingly, this common disease endpoint does not constitute proof of a common disease mechanism. Whereas our previous work and the work of others found that Ccm2 and Krit1 play similar roles in embryonic development, in vitro cell biology, and cell signaling (9, 10, 12, 13), these roles differ from those we observe with Pdcd10. Unlike Krit1 and Ccm2, Pdcd10 is not required for development of the branchial arch arteries that connect the heart to the aorta. Rather, Pdcd10 has an essential, nonendothelial role in development not shared with Krit1 or Ccm2 as well as an essential function in venous maturation. We further observe differences in cell biology and signaling between PDCD10 and KRIT1 or CCM2; whereas the loss of KRIT1 or CCM2 leads to RhoA activation, increased Rho kinase activity, myosin light chain phosphorylation, and actin stress fiber formation (9, 12, 13), we do not observe activation of this signaling pathway in cells depleted of PDCD10. Instead, we found that PDCD10 signals primarily through the GCKIII family of kinases.

The similarity in human CCM disease caused by mutations in *KRIT1*, *CCM2*, and *PDCD10* have led to an assumption that the proteins encoded by these genes function in a common signaling pathway. This assumption has been supported by experimental evidence showing binding between ectopically expressed, epitope-tagged proteins (7, 8). However, the complexities of signaling pathways and pathophysiology allow for multiple mechanisms to converge on a common disease phenotype (Figure 8A). An example is hypertrophic cardiomyopathy, which was considered 1 disease until molecular genetics revealed that 2 different mechanisms (sarcomere function or metabolism), each affected by distinct genes, both result in pathologic hypertrophy (Figure 8B and ref. 46). We propose that a similar scenario is involved in the pathogenesis of CCM (Figure 8C).

There is controversy concerning the signaling pathways affected by PDCD10. Several reports suggest an essential role for binding GCKIII family serine-threonine kinases (16, 21–23). However, a recent characterization of mice carrying a different conditional allele of *Pdcd10* showed that the loss of Pdcd10 in endothelial cells substantially blocks VEGFR2 signaling and inhibits the earliest stages of developmental angiogenesis (47). The implication of VEGFR2 signaling through MAP kinases agrees with a previous report linking GCKIII kinases and ERK signaling (20). Our data contrast with these reports; we observe that the absence of Pdcd10 in vivo leads to a localized vascular defect at a much later developmental stage, inconsistent with a panendothelial block of VEGF signaling. In cell culture, we have not found any interaction between PDCD10 and VEGF or ERK signaling (Supplemental Figure 11). We suspect that this disparity may be due to a difference in knockout strategy; however, our confidence in our allele is bolstered by our ability to induce CCM disease. Our data support the model that PDCD10 signals through the GCKIII family kinases, as we have observed in human endothelial cells and in *Drosophila* that PDCD10 binds to GCKIII family kinases and both are required for lumen formation. Previous reports have further suggested that GCKIII signals through RhoA to converge



**Table 3**
Pathologic findings in human and murine CCMs

| Genotype | Human *CCM2* | Murine *Ccm2* | Human *PDCD10* | Murine *Pdcd10* |
|---|---|---|---|---|
| Trichrome | + | + | ++ | ++ |
| Iron | + | + | ++ | ++ |
| Elastin | – | – | – | – |
| CD34 | + | NA | + | NA |
| CD31 | NA | + | NA | + |
| Laminin | + | + | + | + |
| Collagen IV | + | + | + | + |

The pathologic findings compared for human and murine CCMs associated with mutations of either *CCM2* or *PDCD10*.

with KRIT1/CCM2 signaling (23). By direct comparison of Ccm2 and Pdcd10 in mouse and cell biology, however, our data suggest that PDCD10 signaling is distinct from the CCM2-RhoA axis.

The nature and severity of disease in familial forms of CCM in comparison with sporadic CCM suggested a genetic mechanism consistent with Knudson's 2-hit hypothesis (33): LOH for a CCM gene induces lesions. Limited evidence to support this theory has come from a few human surgical samples amid multiple cases in which the second genetic hit could not be found (27, 28). Further supportive evidence comes from mice with heterozygous mutations for *Krit1* or *Ccm2* that have been mated into strains with high rates of spontaneous mutations. Mice heterozygous for *Krit1* develop CCM lesions on either a p53- or Msh2-null background, whereas mice heterozygous for *Ccm2* develop lesions only on the p53-, but not the Msh2-null background (35, 36). Whereas these models provide suggestive evidence of LOH and employ stochastic events to induce CCM formation, LOH was not demonstrated at either locus, nor can the LOH hypothesis be supported for all CCM genes, as $Ccm2^{+/-}$;$Msh2^{-/-}$ mice do not develop CCMs. These models also do not rule out a role for mutations in other, non-CCM genes and do not control tissue specificity of mutation. The penetrance of CCMs in these models is incomplete, complicating the use of these models in prospective trials to study therapeutics or natural history of CCM disease. Concurrent development of neoplasms in both the p53- and the Msh2-null backgrounds also adds confounding physiological stressors and increases the mortality of the animals. In contrast, we employ a strategy that allows direct testing of the LOH mechanism in CCM disease. Using an inducible Cre-recombinase, we have targeted gene-specific LOH for both *Pdcd10* and *Ccm2* to the endothelium of mice. In the case of both genes, we have found that LOH is sufficient to cause a fully penetrant CCM phenotype that recapitulates every key pathologic and radiologic hallmark of human disease.

Much work remains to translate the observations and insights regarding disease signaling mechanisms into viable therapeutic strategies in patients. This work underscores the importance of carefully considering disease mechanisms in a genotype-specific manner. The availability of faithful, genotype-specific, and highly penetrant mouse models of CCM disease unlocks the tremendous opportunities to study the natural history of lesion genesis and progression as well as opportunities for preclinical testing of therapeutic interventions. In order for mouse models of CCM disease to be useful in informing human studies, the same tools used to follow patients with CCM need to be developed for serial observation of affected mice. We have demonstrated that noninvasive MRI of live mice, the same modality used to follow CCM in humans, can detect and follow murine CCMs. Although our mouse models share a measurable mortality, as with humans, they are compatible with prolonged survival and serial, noninvasive observation. The ability to follow these mice noninvasively over time is a crucial prerequisite for judging the effectiveness of any preclinical therapeutic strategy in the future and for testing the timing and intensity of LOH required for lesion formation. Our mouse models of CCM phenocopy human disease closely, supplanting previously available surrogate phenotypes, and are a powerful new tool in the armamentarium to decipher and combat CCM disease.

## Methods

*Mouse strains.* The *Ccm2* conditional knockout mice have been previously described (9). A construct for the conditional allele of *Pdcd10* was derived from genomic sequence obtained from a BAC clone (RP22 library; Invitrogen). The construct extended from a SacII site 5′ of exon 4 through an ApaI site 3′ of exon 8. The construct contained inserts as outlined in Supplemental Figure 1, including LoxP sequences at a KasI site just 5′ of exon 4 and at a EcoRI site just 3′ of exon 8. All mice were backcrossed into the C57BL/6J strain. Experiments performed prior to the fifth cross were performed with littermate controls. *LacZ* reporter mice (R26R1), *Tie2-Cre*

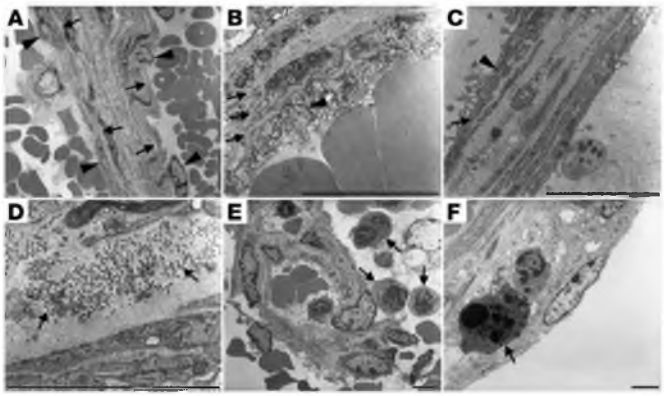


**Figure 6**
Ultrastructural findings in murine cavernous malformations. (**A**) Dilated vascular channels are lined by endothelial cells (arrowheads) with associated basal lamina (arrows). (**B**) Occasional channels have segments with a multilayered appearance (arrows indicate lamellae of endothelium with basal laminae). Tight junctions appear intact (arrowhead). (**C**) Focal areas of endothelial attenuation are observed (arrow) without apparent gaps or disruption of tight junctions (arrowhead indicates a junctional complex). (**D**) Channels are separated by loose connective tissue composed mostly of collagen (arrows). (**E**) Foci of mononuclear inflammatory cells are present (arrows). (**F**) Hemosiderin-laden macrophages (arrow) are among the inflammatory cells observed. Images are representative of 5 lesions from 3 *Pdcd10* mice. Scale bars: 4 μm.

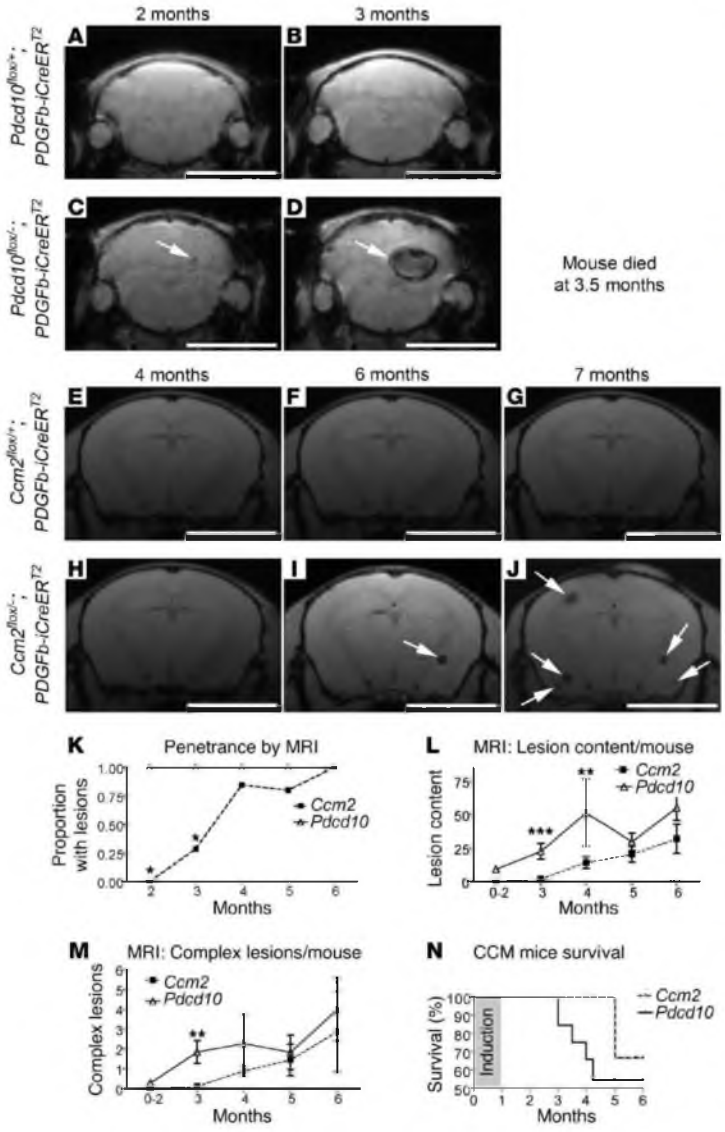


**Figure 7**

Natural history of murine CCM by MRI — *Pdcd10* onsets earlier and is more severe than *Ccm2*. (**A**–**D**) Live MRI scans of the same *Pdcd10*$^{flox/+}$;*PDGFb-iCreER*$^{T2}$ mouse at 2 months and 3 months (**A** and **B**) and its *Pdcd10*$^{flox/-}$;*PDGFb-iCreER*$^{T2}$ littermate (**C** and **D**). Both mice were given tamoxifen at birth. (**E**–**J**) Live MRI scans of the same *Ccm2*$^{flox/+}$;*PDGFb-iCreER*$^{T2}$ mouse (**E**–**G**) and its *Ccm2*$^{flox/-}$;*PDGFb-iCreER*$^{T2}$ littermate (**H**–**J**) at 4, 6, and 7 months. Both mice were given tamoxifen at birth. Arrows indicate CCM lesions. (**K**) Disease penetrance (proportion affected) by age in *Ccm2* and *Pdcd10* induced knockout mice as assessed by live MRI. (**L**) Lesion burden assessed as total number of lesions observed on each tomographic view (slice) of the MRI per mouse. (**M**) Number of complex lesions (lesions with bright cores) per mouse. (**N**) Kaplan-Meier survival curve of *Ccm2* and *Pdcd10* induced knockout mice. For **K**–**N**, $n = 11$ *Ccm2*, $n = 13$ *Pdcd10*. Data in **L** and **M** represent mean ± SEM. $^{*}P < 0.01$; $^{**}P < 0.05$; $^{***}P < 0.001$. Scale bars: 1 mm.

mice, and *PDGFb-iCreER*$^{T2}$ mice were generously provided by Phil Soriano (Fred Hutchinson Cancer Research Center, Seattle, Washington, USA, and Mount Sinai School of Medicine, New York, New York, USA), Masashi Yanagisawa (University of Texas Southwestern Medical Center at Dallas, Dallas, Texas, USA), and Marcus Fruttiger (University College London Institute of Ophthalmology, London, United Kingdom) via Holger Gerhardt (London Research Institute – Cancer Research UK, London, United Kingdom), respectively. *HPRT-Cre*, *Nestin-Cre*, and *Tomato-EGFP* reporter mice were obtained from The Jackson Laboratory. Genotypes were determined by PCR analysis of genomic DNA isolated from either ear biopsies or yolk sac tissues using primers outlined in Supplemental Figure 1. Primer sequences were as follows: primer W: 5′-GCAATCCATCTTGTTCAATGGC-3′, primer X: 5′-CGTAGGTCAGGGTGGTCACG-3′, primer Y: 5′-TGAAAGAGGACATACTGGAGAGGC-3′, primer Z: 5′-AAGGACAAGAAAGCACTGTTGACC-3′. Tamoxifen (Sigma-Aldrich) was resuspended in corn oil (Sigma-Aldrich), and 40 ng was given as an i.p. injection to mouse pups on perinatal day 1.

*MRI of mouse brains.* All MRI experiments were conducted on a 7T Bruker Biospec 70/30 USR scanner (Bruker Biospin MRI Inc.) equipped with a BGA12S gradients set. A combination of volume-transmit-only radio frequency coil (internal diameter: 72 mm) and a quad-surface-receive-only coil (internal diameter: 1.5 cm) were used. For live scans, mice were anesthetized in 2.5% isoflurane and then placed into the scanner on top of circulating heated water. During the scans, mice were monitored for temperature and respiration, with isoflurane concentration and water bath temperature adjusted to maintain a body temperature between 35.8°C and 37.6°C and respiration between 75 and 100 breaths/min. A gradient recalled echo sequence was used to acquire coronal slices spanning the whole brain. Sequence parameters were as follows: repetition time, 328 ms; echo time, 5.4 ms; flip-angle, 40°; 12 averages, in-plane-resolution, 125 μm × 125 μm; and slice thickness, 0.5 mm.

For postmortem specimens, mouse skulls were fixed in 4% formaldehyde for at least 3 days before the brain was imaged with the skull intact. Postmortem MRI scanning allows a high-resolution coverage of the brain at the expense of longer scan time. High-resolution 3D gradient echo was acquired using the same scanner configuration described above, with isotropic voxel size of 78 μm × 78 μm × 78 μm over 9 hours. Other sequence parameters were as follows: repetition time, 250 ms; echo time, 7.5 ms; flip angle, 30°; and 2 averages.

*Histology.* Embryo and mouse CCM lesions were studied with antibodies to PECAM (1:250 dilution, clone MEC13.3; BD Biosciences) and PDCD10 (1:50 dilution, Prestige Antibody; Sigma-Aldrich). Improved visualization on paraffin sections was obtained using a biotinylated tyramide signal

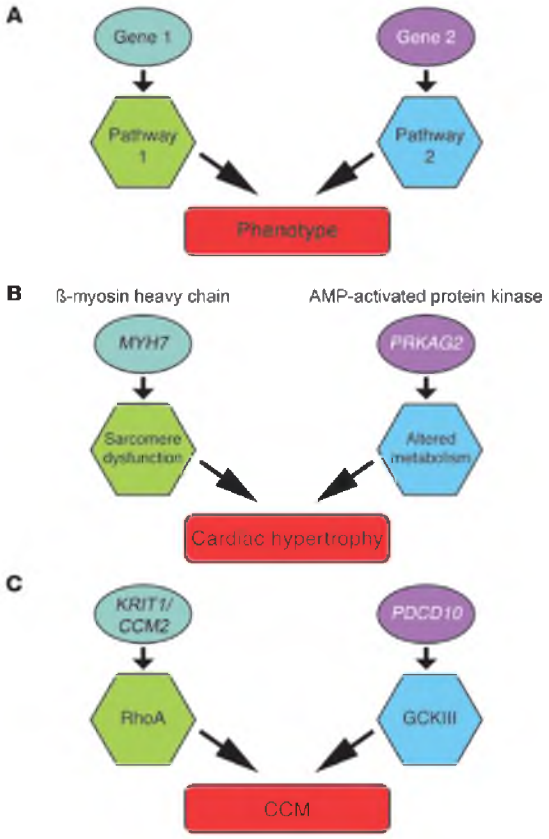


**Figure 8**
Convergence of different mechanistic pathways in common pathology. (**A**) Proposed schema for different genes acting on separate mechanistic pathways, yet ultimately resulting in a common expression of disease. (**B**) Genetic studies of hypertrophic cardiomyopathy highlight genes that can be grouped broadly into 2 separate mechanistic pathways: sarcomeric proteins such as β-myosin heavy chain (MYH7), and metabolic genes including adenosine monophosphate-activated protein kinase (PRKAG2). (**C**) Studies of mouse development, cell biology, and signaling suggest that KRIT1 and CCM2 signal through RhoA GTPase, while PDCD10 signals through GCKIII kinases to lead to cavernous malformations.

amplification (TSA) kit (PerkinElmer) according to the manufacturer's instructions. To demonstrate tissue specificity of *PDFGb-iCreER*$^{T2}$, brains from mice carrying a *LacZ* reporter allele were fixed and then stained with X-gal as previously described (48). Brains from mice carrying the *Tomato-EGFP* reporter allele were fixed and then embedded into OCT (Fisher Scientific) for fluorescent frozen sections. H&E staining of embryos was performed using standard procedures.

For histology of adult mouse brains, mouse skulls were fixed in 4% formaldehyde for at least 3 days or zinc-buffered formalin overnight before the brain was removed and sliced into 4 coronal sections. These sections were embedded into paraffin by standard techniques. Prussian blue staining for iron and Masson's trichrome staining of mouse brain sections were performed using the Artisan system (DAKO) according to manufacturer's instructions. Staining for elastin, laminin, and collagen IV was performed by the Immunohistochemistry Research and Development Lab at ARUP Laboratories. Human CCM samples were stained in the same way as adult mouse brains except for CD34 staining, which was performed by the Central Labs at Intermountain Medical Center (Murray, Utah, USA).

*Fluorescent staining of mouse retinas.* Mice were anesthetized using Avertin (2,2,2-tribromoethanol, 0.4 mg/g; Acros Organics) and perfused with fluorescently conjugated tomato lectin (Vector Labs) as previously described (49) at a dose of 5 μg/g body weight. After 5 minutes, mice were perfused with saline and then with 4% formaldehyde. Retinas were then extracted, stained, and mounted as previously described (50).

*Analysis of mouse embryos.* Confocal immunofluorescence of embryos and fetal ultrasound were performed as previously described (9).

*Transmission electron microscopy.* Samples were fixed in 1% formaldehyde, 2.5% glutaraldehyde in 0.1 M sodium cacodylate buffer with 8 mM $CaCl_2$ and 2.4% sucrose, pH 7.4, for at least 3 days. Samples were then rinsed in 0.1 M cacodylate buffer, postfixed in 2% osmium tetroxide in 0.1 M cacodylate buffer, rinsed in type I water, and then enbloc stained with saturated aqueous uranyl acetate. Samples were dehydrated through a graded series of ethanols, followed with final dehydration in acetone, and then infiltrated and embedded in an epoxy resin.

Thick sections and thin sections were cut on a Leica EM UC6 ultramicrotome (Leica Microsystems). The thick sections were cut with glass and the thin sections were cut with a diatome diamond knife. Thick sections were dried on glass slides and were stained with 1% toluidine blue O in 1% aqueous sodium borate. Thin sections were placed on 135 mesh copper hex grids and stained sequentially with saturated aqueous uranyl acetate and Reynolds lead citrate.

Sections were examined on an FEI Tecnai T-12 transmission electron microscope (FEI) at 80 KV. Images were taken on Kodak 4489 electron microscope film, developed with Kodak D-19 developer, fixed, washed, and dried. The negatives were scanned on an Epson Perfection Photo 4990 flatbed scanner.

*Cell culture.* HUVEC and HMVEC were obtained from Lonza and grown according to the manufacturer's instructions in EGM-2 media (HUVEC) or EGM-2MV media (HMVEC). Human embryonic kidney (HEK 293T) cells (ATCC) were grown in DMEM (Gibco; Invitrogen) with 10% fetal bovine serum (Bio-West) supplemented with antibiotics. EAHY cells were generously provided by Andrew Weyrich (University of Utah) and were grown in DMEM with 10% fetal bovine serum and HAT supplement (Sigma-Aldrich).

*Transfection of ECs with siRNAs.* Human *CCM2* and *PDCD10* siRNAs were obtained from Dharmacon. Luciferase GL2 duplex or nontargeting siRNA (Dharmacon) were used as controls. EC transfection with siRNAs was carried out in growth media with 1% serum. Details of the siRNA transfection protocol have been described previously (51).

*RT-PCR.* Total RNA was extracted from EC vasculogenesis assay at indicated time points or from siRNA-treated ECs using the ToTALLY RNA Isolation Kit (Ambion) according to the manufacturer's instructions. RNA (1 μg) was reverse transcribed using AccuScript High Fidelity 1st strand cDNA synthesis kit (Stratagene; Agilent). RT-PCR amplification used the following primers: forward: 5′-AGACTTCACGGAGTCCCTTC-3′, reverse: 5′-AGAAGGTCTGAAGTATTAAGTTGG-3′. For quantitative real-time PCR, total RNA was extracted from cultured endothelial cells or from embryos using the NucleoSpin RNA II Kit (Clontech) according to the manufacturer's instructions. Reverse transcription was performed with random primers using the RETROScript Kit (Ambion). Quantitative PCR was performed with TaqMan assays (Applied Biosystems) for human *CCM2*, *PDCD10*, *GAPDH*, *STK24*, *STK25*, and *MST4* or mouse *Pdcd10* and *Gapdh*. Quantification was performed by standard curve method, and

*CCM2* and *PDCD10* transcripts were normalized to *GAPDH* for comparisons. RT-PCR primers for embryonic *Pdcd10* transcripts were as follows: primer 4F: 5′-TTCACCGAGTCCCTCCTTCG-3′; primer 7/8R: 5′-GAACACATTTATTGCCTTGCCATC-3′; primer 1F: 5′-AAGTCCGTGCCTCAGTTGCC-3′; and primer EGFP-R: 5′-TCCTCGCCCTTGCTCACC-3′.

*Immunofluorescent cell staining.* Glass chamber slides (Nalge Nunc; Thermo Fisher) were coated with human fibronectin (Biomedical Technologies Inc.), and transfected cells were seeded at 50,000 cells per well. Cells were fixed in 4% formaldehyde and actin cytoskeleton was visualized using fluorescently conjugated phalloidin (Molecular Probes; Invitrogen). Images were obtained with an Olympus FV300 confocal microscope.

*Endothelial cell vasculogenesis in 3D collagen matrices.* This assay was performed as previously described (9, 38).

*Immunoprecipitation and Western blotting.* An expressed sequence tag (EST) for human *PDCD10* (IMAGE: 3050540) was obtained from ATCC and cloned into a pcDNA3.1 Hygro$^+$ plasmid (Invitrogen) modified to encode an N-terminal FLAG tag. ESTs for *Drosophila Pdcd10* and *GCKIII* were obtained from the Drosophila Genomics Resource Center and cloned into a pcDNA3.1 Hygro$^+$ plasmid modified to encode an N-terminal FLAG tag (*Pdcd10*) or HA tag (*GCKIII*). PDCD10Δ18 constructs were made using nested PCR with primers designed to overlap and omit the 54 nucleotides encoding those 18 amino acids. Plasmids were transfected into EAHY or HEK 293T cells using Lipofectamine 2000 (Invitrogen) according to the manufacturer's instructions, with a reduced dosage of DNA and lipofectamine for EAHY cells. Two days after transfection, cells were scraped into lysis buffer (50 mM Tris-HCl at pH 7.5, 100 mM NaCl, 0.5% Triton X-100) supplemented with protease and phosphatase inhibitors and 1 mM DTT. A portion of cell lysate was retained as whole cell lysate and the rest precleared with normal mouse IgG conjugated to agarose beads (Santa Cruz Biotechnology Inc.) at 4°C for 1 hour, then incubated with anti-FLAG resin at 4°C for 2 hours. The beads were washed 3 times with lysis buffer, and bound proteins were eluted using Laemmli sample buffer. Presence of FLAG-tagged PDCD10 proteins was detected using the anti-FLAG M2 antibody (Sigma-Aldrich). Presence of HA-tagged GCKIII was detected using an anti-HA antibody (Santa Cruz Biotechnology Inc.). Near-infrared secondary antibodies (LI-COR Biosciences) were used to probe the blots, which were visualized using the Odyssey system (LI-COR Biosciences).

Rabbit polyclonal antibody against PDCD10 was from Proteintech Group. Rabbit antibodies against phospho-myosin light chain (Thr18/Ser19), phospho-VEGFR2 (Tyr1175), total VEGFR2, phospho-PLCγ (Tyr783), total PLCγ, phospho-ERK1/2 (Thr202/Tyr204), and total ERK1/2 were from Cell Signaling Technology. α-Actinin antibody (clone H-2) was from Santa Cruz Biotechnology Inc. HRP-conjugated secondary antibodies were from Jackson ImmunoResearch. Western blots were developed using the ECL Plus Western blotting reagent (GE Healthcare) and Kodak Biomax MR film.

*Drosophila strains.* The GAL4/UAS system was used for tissue-specific RNAi knockdown (43). The driver used was *btl-GAL4* (42), and RNAi targeting constructs v109453 (against *Pdcd10*) (41), v106841 (against *Pdcd10*) (41), and v49559 (against *GCKIII*) (44) were obtained from the Vienna Drosophila RNAi Center. For rescue experiments, full-length cDNAs for *Drosophila Pdcd10* were cloned into a pUAST transformation vector containing an attb site for site-specific transformation (52) provided by Carl Thummel (University of Utah). Transgenes were injected into docking sites VK00027 (53) and attp0016 (52) by Genetic Services Inc., and homozygous lines were established by standard methods.

For cDNA rescue experiments, flies homozygous for the cDNA rescuing construct on the third chromosome were crossed to a homozygous *btl-GAL4, UAS-GFP* driver line on the second chromosome to generate transheterozygote flies (*btl-GAL4, UAS-GFP*/+; *UAS-Rescue*/+). Males of this genotype were then crossed to virgin females homozygous for the RNAi targeting construct located on the second chromosome. GFP expression indicated the presence of the *btl-GAL4, UAS-GFP* transgenes. All of these larvae contain 1 copy of the RNAi targeting construct, and half also have the cDNA rescue transgene. Results shown used the v109453 line, which targets the 3′ UTR of *Pdcd10*. The v106841 line showed similar results.

*Analysis of tracheal tube formation in Drosophila larvae.* Animals were scored at the prewandering third instar larval stage for tracheal defects. Animals were graded by scoring air filling in primary sprouts emanating from the dorsal trunk. All primary sprouts were scored bilaterally (at least 12 per larva). The animals were categorized as having severe, moderate, or mild defects or wild-type if they had 3 or more of the following defects: (a) severe defects were truncations before the first bifurcation of the primary side branches or immediately after branching; (b) moderate defects represented gaps in air filling with filled tubes on both sides; (c) mild defects were loss of air filling only in the fine terminal tubes. In the event that more than 1 criterion was met, the more severe category was selected. If animals had fewer than 3 branches with a given defect, the less severe category was selected. Only animals with no defects were categorized as wild type.

*Mouse and human experiments.* All mouse experiments were approved by the University of Utah Institutional Animal Care and Use Committee. Human tissue samples were obtained with written informed consent and provided by Connie Lee and Amy Akers (Angioma Alliance, Norfolk, Virginia, USA) and Randy Jensen (University of Utah). Human experiments were approved by the Institutional Review Board of the University of Utah.

*Statistics.* For actin stress fiber content, and for in vitro lumen formation with GCKIII kinases, we performed ANOVA with Tukey's post hoc analysis with an $\alpha$ value of 0.05. For in vitro lumen formation time course for PDCD10, we performed statistical comparisons between treatment groups with a 2-tailed paired-sample *t* test with an $\alpha$ value of 0.05. For the tracheal tube formation rescue experiment, we performed a $\chi^2$ test for independence with an $\alpha$ value of 0.05 (degrees of freedom = 9). For CCM penetrance and lesion content, we performed a 2-tailed *t* test with an $\alpha$ value of 0.05.

## Acknowledgments

We thank N. London, S. Navankasattusas, L. Shi, Y. Xiong, C. Jensen, J. Zhu, D. Zurcher, A. Fang, T. Mleynek, and D. Lim for technical assistance; O. Abdullah and E. Hsu and the University of Utah Small Animal Imaging Facility; C. Rodesch and the University of Utah Cell Imaging/Fluorescence Facility; N. Chandler and the University of Utah Electron Microscopy Facility; S. Tripp and the Immunohistochemistry Research and Development Lab at ARUP Laboratories; J. Hansen at Central Labs at Intermountain Medical Center; K. Thomas and S. Odelberg for critical comments and helpful scientific discussions; and S. Chin for helpful scientific discussions. This work was funded by the US NIH (to G.E. Davis, M.M. Metzstein, K.J. Whitehead, and D.Y. Li), including training grant T32-GM007464 (to A.C. Chan and O.E. Ruiz), the Hellenic Cardiological Society (to N.A. Diakos), the American Heart Association (to K.J. Whitehead and D.Y. Li), the H.A. and Edna Benning Foundation, the Juvenile Diabetes Research Foundation, and the Burroughs Wellcome Fund (to D.Y. Li).

Received for publication July 16, 2010, and accepted in revised form March 2, 2011.

Address correspondence to: Kevin J. Whitehead, Room 4A100, 30 N 1900 East, Salt Lake City, Utah 84132, USA. Phone: 801.581.7715; Fax: 801.581.7735; E-mail: kevin.whitehead@u2m2.utah.edu. Or to: Dean Y. Li, Building 533 Room 4220, 15 N 2030 East, Salt Lake City, Utah 84112, USA. Phone: 801.585.5505; Fax: 801.585.0701; E-mail: dean.li@u2m2.utah.edu.




1. Otten P, Pizzolato GP, Rilliet B, Berney J. A propos de 131 cas d'angiomes caverneux (cavernomes) du S.N.C. reperés par l'analyse rétrospective de 24 535 autopsies. *Neurochirurgie*. 1989;35(2):82–83.
2. Vernooij MW, et al. Incidental findings on brain MRI in the general population. *N Engl J Med*. 2007;357(18):1821–1828.
3. Hasegawa T, McInerney J, Kondziolka D, Lee JY, Flickinger JC, Lunsford LD. Long-term results after stereotactic radiosurgery for patients with cavernous malformations. *Neurosurgery*. 2002;50(6):1190–1197.
4. Chappell PM, Steinberg GK, Marks MP. Clinically documented hemorrhage in cerebral arteriovenous malformations: MR characteristics. *Radiology*. 1992;183(3):719–724.
5. Burger PC, Scheithauer BW. *Tumors of the Central Nervous System*. Washington, DC, USA: American Registry of Pathology; 2007.
6. Wang H, Gujrati M. Pathology of cerebral cavernous malformations. In: Lanzino G, Spetzler RF, eds. *Cavernous Malformations of the Brain and Spinal Cord*. New York, New York, USA: Thieme Medical Publishers, Inc; 2008:22–25.
7. Faurobert E, Albiges-Rizo C. Recent insights into cerebral cavernous malformations: a complex jigsaw puzzle under construction. *FEBS J*. 2010;277(5):1084–1096.
8. Hilder TL, et al. Proteomic identification of the cerebral cavernous malformation signaling complex. *J Proteome Res*. 2007;6(11):4343–4355.
9. Whitehead KJ, et al. The cerebral cavernous malformation signaling pathway promotes vascular integrity via Rho GTPases. *Nat Med*. 2009;15(2):177–184.
10. Whitehead KJ, Plummer NW, Adams JA, Marchuk DA, Li DY. Ccm1 is required for arterial morphogenesis: implications for the etiology of human cavernous malformations. *Development*. 2004;131(6):1437–1448.
11. Boulday G, et al. Tissue-specific conditional CCM2 knockout mice establish the essential role of endothelial CCM2 in angiogenesis: implications for human cerebral cavernous malformations. *Dis Model Mech*. 2009;2(3–4):168–177.
12. Stockton RA, Shenkar R, Awad IA, Ginsberg MH. Cerebral cavernous malformations proteins inhibit Rho kinase to stabilize vascular integrity. *J Exp Med*. 2010;207(4):881–896.
13. Glading A, Han J, Stockton RA, Ginsberg MH. KRIT-1/CCM1 is a Rap1 effector that regulates endothelial cell cell junctions. *J Cell Biol*. 2007;179(2):247–254.
14. Borikova AL, et al. Rho kinase inhibition rescues the endothelial cell cerebral cavernous malformation phenotype. *J Biol Chem*. 2010;285(16):11760–11764.
15. Zawistowski JS, et al. CCM1 and CCM2 protein interactions in cell signaling: implications for cerebral cavernous malformations pathogenesis. *Hum Mol Genet*. 2005;14(17):2521–2531.
16. Fidalgo M, Fraile M, Pires A, Force T, Pombo C, Zalvide J. CCM3/PDCD10 stabilizes GCKIII proteins to promote Golgi assembly and cell orientation. *J Cell Sci*. 2010;123(pt 8):1274–1284.
17. Zhang J, Clatterbuck RE, Rigamonti D, Chang DD, Dietz HC. Interaction between krit1 and icap1alpha infers perturbation of integrin beta1-mediated angiogenesis in the pathogenesis of cerebral cavernous malformation. *Hum Mol Genet*. 2001;10(25):2953–2960.
18. Zawistowski JS, Serebriiskii IG, Lee MF, Golemis EA, Marchuk DA. KRIT1 association with the integrin-binding protein ICAP-1: a new direction in the elucidation of cerebral cavernous malformations (CCM1) pathogenesis. *Hum Mol Genet*. 2002;11(4):389–396.
19. Uhlik MT, et al. Rac-MEKK3-MKK3 scaffolding for p38 MAPK activation during hyperosmotic shock. *Nat Cell Biol*. 2003;5(12):1104–1110.
20. Ma X, et al. PDCD10 interacts with Ste20-related kinase MST4 to promote cell growth and transformation via modulation of the ERK pathway. *Mol Biol Cell*. 2007;18(6):1965–1978.
21. Voss K, et al. Functional analyses of human and zebrafish 18-amino acid in-frame deletion pave the way for domain mapping of the cerebral cavernous malformation 3 protein. *Hum Mutat*. 2009;30(6):1003–1011.
22. Goudreault M, et al. A PP2A phosphatase high-density interaction network identifies a novel striatin-interacting phosphatase and kinase complex linked to the cerebral cavernous malformation 3 (CCM3) protein. *Mol Cell Proteomics*. 2008;8(1):157–171.
23. Zheng X, et al. CCM3 signaling through sterile 20-like kinases plays an essential role during zebrafish cardiovascular development and cerebral cavernous malformations. *J Clin Invest*. 2010;120(8):2795–2804.
24. Denier C, et al. Genotype-phenotype correlations in cerebral cavernous malformations patients. *Ann Neurol*. 2006;60(5):550–556.
25. Sirvente J, Enjolras O, Wassef M, Tournier-Lasserve E, Labauge P. Frequency and phenotypes of cutaneous vascular malformations in a consecutive series of 417 patients with familial cerebral cavernous malformations. *J Eur Acad Dermatol Venereol*. 2009;23(9):1066–1072.
26. Labauge P, et al. Multiple dural lesions mimicking meningiomas in patients with CCM3/PDCD10 mutations. *Neurology*. 2009;72(23):2044–2046.
27. Akers AL, Johnson E, Steinberg GK, Zabramski JM, Marchuk DA. Biallelic somatic and germline mutations in cerebral cavernous malformations (CCMs): evidence for a two-hit mechanism of CCM pathogenesis. *Hum Mol Genet*. 2009;18(5):919–930.
28. Gault J, et al. Cerebral cavernous malformations: somatic mutations in vascular endothelial cells. *Neurosurgery*. 2009;65(1):138–144.
29. Pagenstecher A, Stahl S, Sure U, Felbor U. A two-hit mechanism causes cerebral cavernous malformations: complete inactivation of CCM1, CCM2 or CCM3 in affected endothelial cells. *Hum Mol Genet*. 2009;18(5):911–918.
30. Rigamonti D, et al. Cerebral cavernous malformations. Incidence and familial occurrence. *N Engl J Med*. 1988;319(6):343–347.
31. Labauge P, Brunereau L, Levy C, Laberge S, Houtteville JP. The natural history of familial cerebral cavernomas: a retrospective MRI study of 40 patients. *Neuroradiology*. 2000;42(5):327–332.
32. Del Curling O Jr, Kelly DL Jr, Elster AD, Craven TE. An analysis of the natural history of cavernous angiomas. *J Neurosurg*. 1991;75(5):702–708.
33. Knudson AG Jr. Mutation and cancer: statistical study of retinoblastoma. *Proc Natl Acad Sci U S A*. 1971;68(4):820–823.
34. Gault J, Shenkar R, Recksiek P, Awad IA. Biallelic somatic and germ line CCM1 truncating mutations in a cerebral cavernous malformation lesion. *Stroke*. 2005;36(4):872–874.
35. Shenkar R, et al. Advanced magnetic resonance imaging of cerebral cavernous malformations: part II. Imaging of lesions in murine models. *Neurosurgery*. 2008;63(4):790–797.
36. McDonald DA, et al. A novel mouse model of cerebral cavernous malformations based on the two-hit mutation hypothesis recapitulates the human disease. *Hum Mol Genet*. 2011;20(2):211–222.
37. Claxton S, Kostourou V, Jadeja S, Chambon P, Hodivala-Dilke K, Fruttiger M. Efficient, inducible Cre-recombinase activation in vascular endothelium. *Genesis*. 2008;46(2):74–80.
38. Davis GE, Camarillo CW. An alpha 2 beta 1 integrin-dependent pinocytic mechanism involving intracellular vacuole formation and coalescence regulates capillary lumen and tube formation in three-dimensional collagen matrix. *Exp Cell Res*. 1996;224(1):39–51.
39. Ghabrial A, Luschnig S, Metzstein MM, Krasnow MA. Branching morphogenesis of the Drosophila tracheal system. *Annu Rev Cell Dev Biol*. 2003;19:623–647.
40. Manning G, Krasnow MA. Development of the Drosophila tracheal system. In *The Development of Drosophila melanogaster*. Bate M, Martinez Arias A, eds. Plainview, New York, USA: Cold Spring Harbor Laboratory Press; 1993:609–685.
41. Mummery-Widmer JL, et al. Genome-wide analysis of Notch signalling in Drosophila by transgenic RNAi. *Nature*. 2009;458(7241):987–992.
42. Shiga Y, Tanaka-Matakatsu M, Hayashi S. A nuclear GFP/beta-galactosidase fusion protein as a marker for morphogenesis in living Drosophila. *Dev Growth Differ*. 1996;38(1):99–106.
43. Brand AH, Perrimon N. Targeted gene expression as a means of altering cell fates and generating dominant phenotypes. *Development*. 1993;118(2):401–415.
44. Dietzl G, et al. A genome-wide transgenic RNAi library for conditional gene inactivation in Drosophila. *Nature*. 2007;448(7150):151–156.
45. Clatterbuck RE, Eberhart CG, Crain BJ, Rigamonti D. Ultrastructural and immunocytochemical evidence that an incompetent blood-brain barrier is related to the pathophysiology of cavernous malformations. *J Neurol Neurosurg Psychiatry*. 2001;71(2):188–192.
46. Wang L, Seidman JG, Seidman CE. Narrative review: harnessing molecular genetics for the diagnosis and management of hypertrophic cardiomyopathy. *Ann Intern Med*. 2010;152(8):513–520.
47. He Y, et al. Stabilization of VEGFR2 signaling by cerebral cavernous malformation 3 is critical for vascular development. *Sci Signal*. 2010;3(116):ra26.
48. Navankasattusas S, et al. The netrin receptor UNC5B promotes angiogenesis in specific vascular beds. *Development*. 2008;135(4):659–667.
49. di Tomaso E, et al. PDGF-C induces maturation of blood vessels in a model of glioblastoma and attenuates the response to anti-VEGF treatment. *PLoS ONE*. 2009;4(4):e5123.
50. Jones CA, et al. Robo4 stabilizes the vascular network by inhibiting pathologic angiogenesis and endothelial hyperpermeability. *Nat Med*. 2008;14(4):448–453.
51. Saunders WB, Bayless KJ, Davis GE. MMP-1 activation by serine proteases and MMP-10 induces human capillary tubular network collapse and regression in 3D collagen matrices. *J Cell Sci*. 2005;118(pt 10):2325–2340.
52. Groth AC, Fish M, Nusse R, Calos MP. Construction of transgenic Drosophila by using the site-specific integrase from phage phiC31. *Genetics*. 2004;166(4):1775–1782.
53. Venken KJ, He Y, Hoskins RA, Bellen HJ. P[acman]: a BAC transgenic platform for targeted insertion of large DNA fragments in D. melanogaster. *Science*. 2006;314(5806):1747–1751.

# Article amendments

## Corrigendum

**Administration of BMP2/7 in utero partially reverses Rubinstein-Taybi syndrome–like skeletal defects induced by *Pdk1* or *Cbp* mutations in mice**

Jae-Hyuck Shim,[1] Matthew B. Greenblatt,[1,2] Anju Singh,[1] Nicholas Brady,[1] Dorothy Hu,[1] Rebecca Drapp,[1] Wataru Ogawa,[3] Masato Kasuga,[4] Tetsuo Noda,[5] Sang-Hwa Yang,[6] Sang-Kyou Lee,[6] Vivienne I. Rebel,[7] and Laurie H. Glimcher[1,2]

[1]Department of Immunology and Infectious Diseases, Harvard School of Public Health, Boston, Massachusetts, USA. [2]Department of Medicine, Harvard Medical School, Boston, Massachusetts, USA. [3]Department of Internal Medicine, Division of Diabetes and Endocrinology, Kobe University Graduate School of Medicine, Kobe, Japan. [4]Research Institute, National Center for Global Health and Medicine, Shinjuku-ku, Tokyo, Japan. [5]Department of Cell Biology, Cancer Institute, Tokyo, Japan. [6]Department of Biotechnology and National Creative Research Initiatives Center for Inflammatory Response Modulation, Yonsei University, Seoul, Republic of Korea. [7]Department of Cellular and Structural Biology, Greehey Children's Cancer Research Institute, University of Texas Health Science Center at San Antonio, San Antonio, Texas, USA.

Original citation: *J Clin Invest.* 2012;122(1):91–106. doi:10.1172/JCI59466.

Citation for this corrigendum: *J Clin Invest.* 2012;122(5):1948. doi:10.1172/JCI63413.

The affiliation for Sang-Hwa Yang and Sang-Kyou Lee was incorrect. In addition, the sentence in Acknowledgments providing the source for Sang-Kyou Lee's research grant was omitted. The correct affiliations list appears above. The omitted sentence is below.

This work was supported by National Creative Research Initiatives, a grant from the National Research Foundation of Korea funded by a Korean government grant (2011-0000425 to S.-K. Lee) and the Brain Korea 21 (BK21) Program.

The authors regret the errors.

## Corrigendum

**Mutations in 2 distinct genetic pathways result in cerebral cavernous malformations in mice**

Aubrey C. Chan, Stavros G. Drakos, Oscar E. Ruiz, Alexandra C.H. Smith, Christopher C. Gibson, Jing Ling, Samuel F. Passi, Amber N. Stratman, Anastasia Sacharidou, M. Patricia Revelo, Allie H. Grossmann, Nikolaos A. Diakos, George E. Davis, Mark M. Metzstein, Kevin J. Whitehead, and Dean Y. Li

Original citation: *J Clin Invest.* 2011;121(5):1871–1881. doi:10.1172/JCI44393.

Citation for this corrigendum: *J Clin Invest.* 2012;122(5):1948. doi:10.1172/JCI63474.

The control data provided in Figure 7, E, F, and G, were inadvertently provided from incorrectly matched samples. The correct images are below.

The authors regret the error.

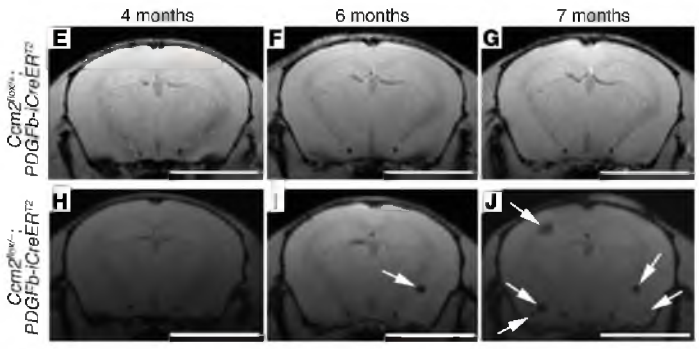

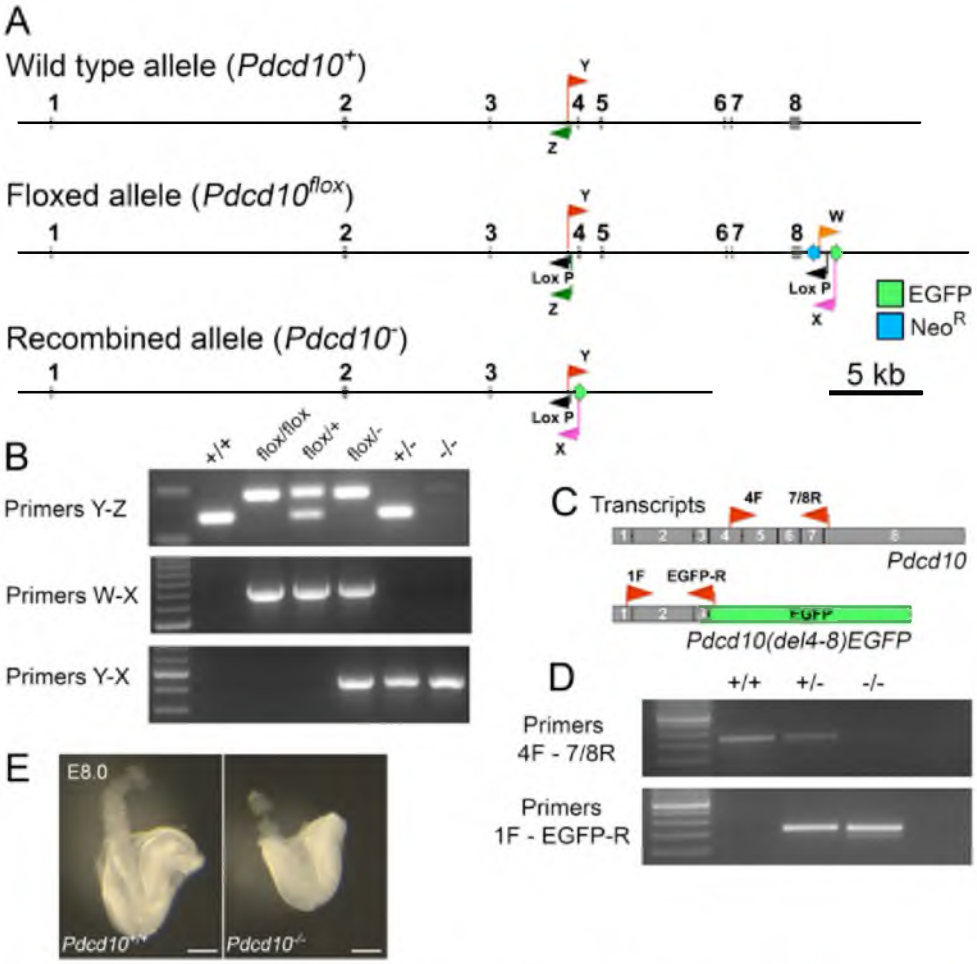


**Supplemental Figure 1. Knockout design for *Pdcd10*. Ubiquitous deletion of *Pdcd10* results in early embryonic death.** (**A**) Alleles of *Pdcd10* are shown. The floxed allele resulting from the targeting strategy includes loxP sites flanking exons 4-8 and places the enhanced green fluorescent protein (EGFP) in position to splice onto exon 3 in a fusion transcript resulting from the recombined allele. Genotyping primers are indicated by the letters W, X, Y and Z. (**B**) Genotyping by PCR using combinations of primers W, X, Y, and Z distinguishes the possible genotypes. (**C**) The wildtype and fusion transcripts are illustrated with exons outlined. The location of primers for RT-PCR are shown. (**D**) Results of RT-PCR performed on cDNA from embryos pooled by genotype that resulted from a mating of $Pdcd10^{+/-}$ vs. $Pdcd10^{+/-}$ mice. (**E**) Gross photos of E8.0 mouse embryos on dissection. Wildtype is shown in (**E**, left panel), *Pdcd10* knockout in (**E**, right panel). Even at this early stage, the knockout embryo has growth arrested and is smaller than its wildtype littermate. Scale bars = 200 μm.

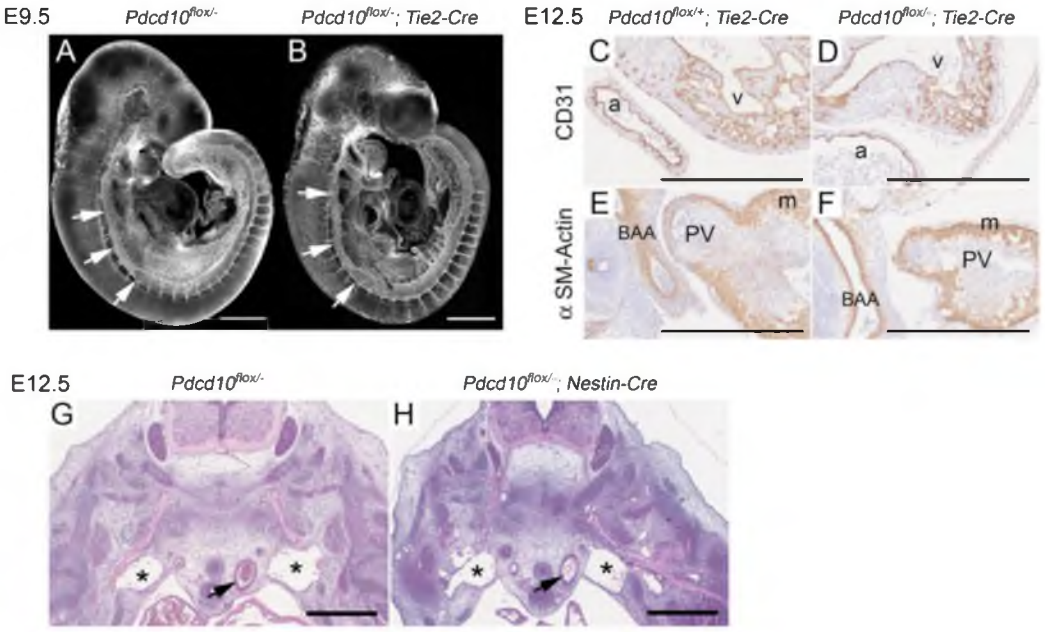


**Supplemental Figure 2. Endothelial knockout of *Pdcd10* does not affect establishment of circulation or cardiac structure. Neural knockout of *Pdcd10* is viable.** (**A-B**) Whole-mount fluorescent staining for CD31 in E9.5 *Pdcd10*$^{flox/-}$ (**A**) and *Pdcd10*$^{flox/-}$*; Tie2-Cre* (**B**) embryos. Arrows denote the dorsal aorta. (**C-D**) Hematoxylin and CD31 staining in E12.5 *Pdcd10*$^{flox/+}$*; Tie2-Cre* (**C**) and *Pdcd10*$^{flox/-}$*; Tie2-Cre* (**D**) embryos. (**E-F**) Hematoxylin and α-smooth muscle actin staining in E12.5 *Pdcd10*$^{flox/+}$*; Tie2-Cre* (**E**) and *Pdcd10*$^{flox/-}$*; Tie2-Cre* (**F**) embryos. a, atrium; v, ventricle; BAA, branchial arch artery; m, myocardium; PV, pulmonary valve. (**G-H**) Hematoxylin and eosin staining in E12.5 *Pdcd10*$^{flox/+}$*; Nestin-Cre* (**G**) and *Pdcd10*$^{flox/-}$*; Nestin-Cre* (**H**) embryos. Asterisks denote the cardinal veins. Arrows denote the dorsal aorta. Scale bars = 500 μm.

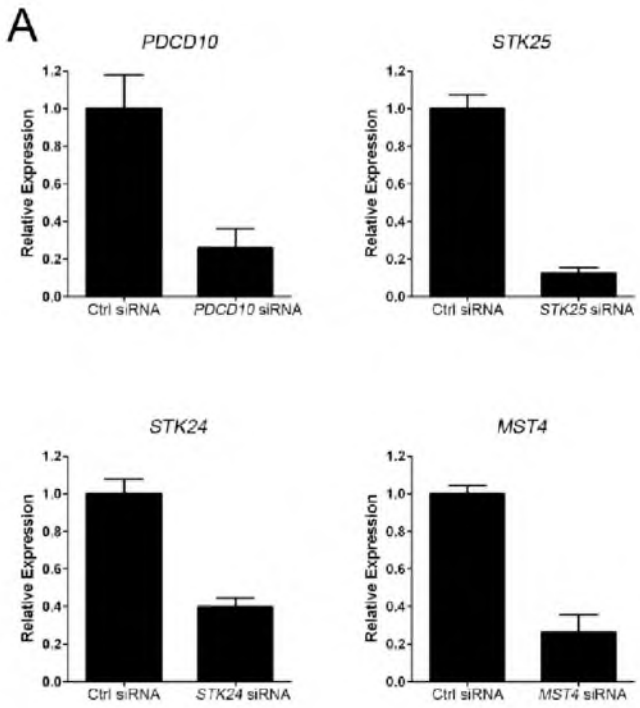


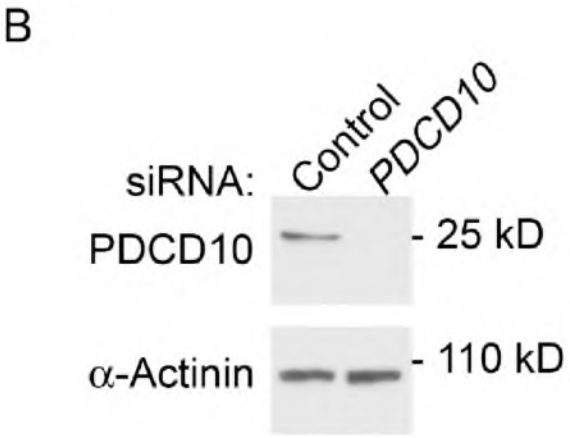


**Supplemental Figure 3. siRNA effectively reduces levels of *PDCD10*, *STK25*, *STK24*, and *MST4*.** (**A**) Quantitative PCR to detect *PDCD10*, *STK25*, *STK24*, and *MST4* was performed on cDNA made from the RNA of human endothelial cells to assess knockdown. (**B**) Western blot for PDCD10 to confirm knockdown.

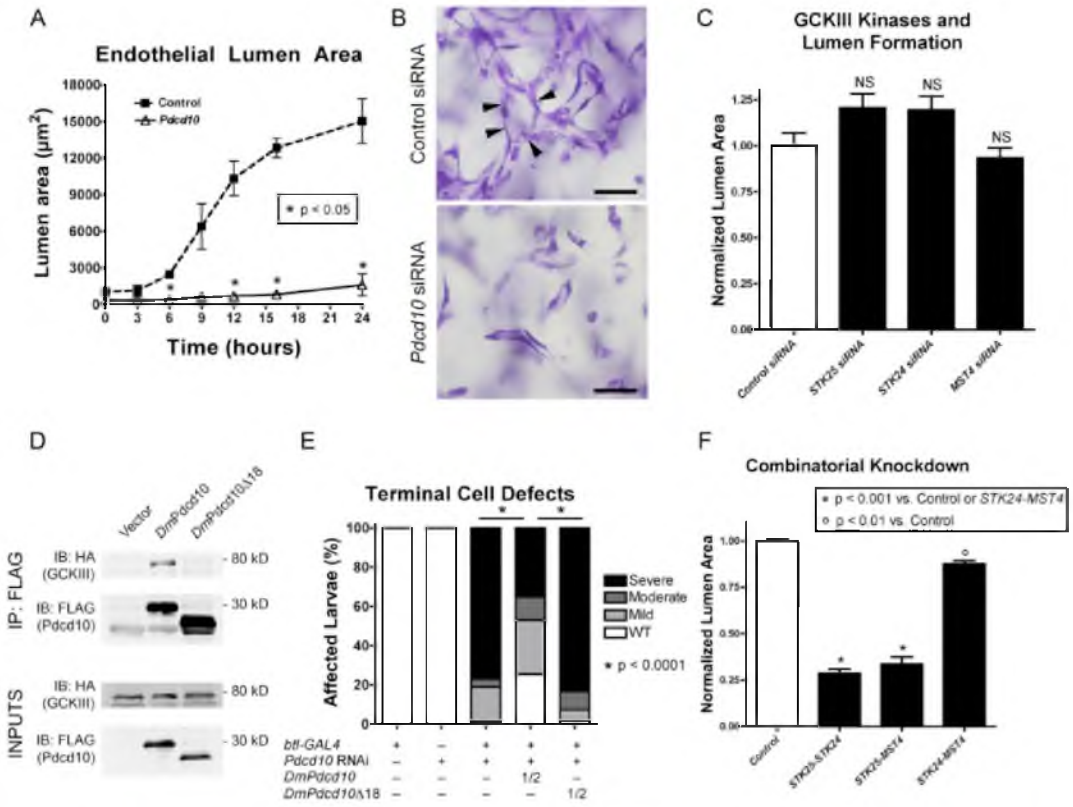


**Supplemental Figure 4. Pdcd10 signals through GCKIII kinases in lumen formation**. (**A**) Quantification of lumen area over time for human umbilical vein endothelial cells after treatment with *PDCD10* siRNA or control siRNA directed against Luciferase. (**B**) Toluidine blue staining of lumen formation assay. Lumens are shown with arrowheads. (**C**) Quantification of lumen area at 24 hours for cells treated with siRNA directed against each of the GCKIII kinases or Luciferase control (5 fields per time point in 3 independent experiments). (**D**) Immunoprecipitation for HA-tagged *Drosophila* GCKIII using full length *Drosophila* Pdcd10 (*Dm*Pdcd10) or *Drosophila* Pdcd10 with 18 amino acid deletion (*Dm*Pdcd10Δ18). Results are representative of 3 independent experiments. (**E**) Quantification of tracheal tube lumen formation defects in *Drosophila* with RNAi knockdown of *Pdcd10* with or without rescue constructs ($N \geq 64$ for each genotype). Note: for rescue experiments only ~50% of all larvae contained the corresponding rescue transgene since they were generated by mating rescue heterozygous males (*btl-GAL4*, *UAS-GFP/+*; *UAS-Rescue/+*) to homozygous *UAS-RNAi* virgin females. (**F**) Quantification of 3D endothelial cell lumen area with combinatorial knockdown of human GCKIII kinases (5 fields per time point in 3 independent experiments). Data indicate mean ± SD. Scale bars = 50 μm.

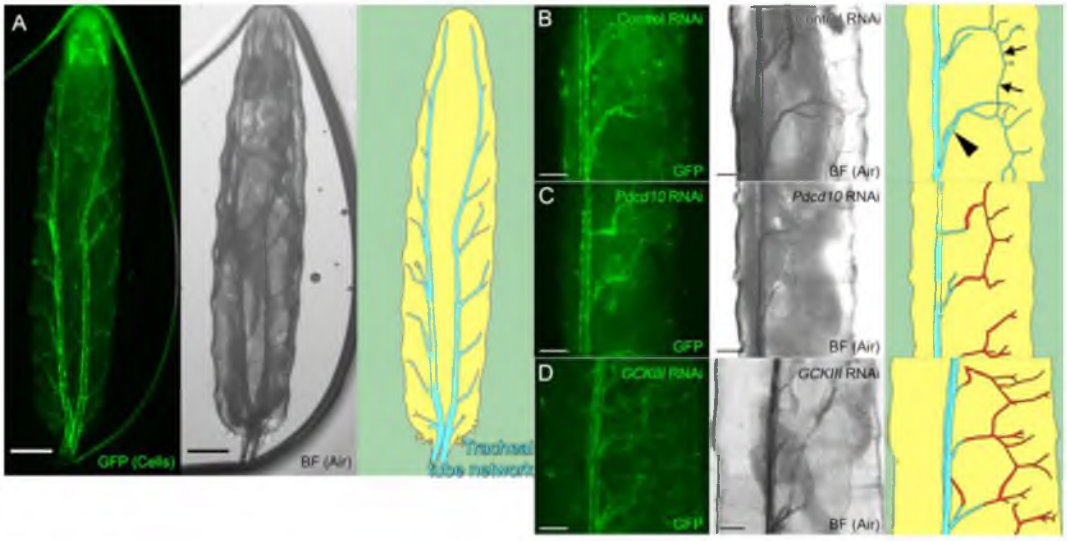


**Supplemental Figure 5. Loss of Pdcd10 or GCKIII results in failure of tracheal tube lumenization in *Drosophila*.** (**A**) The tracheal network of a *Drosophila* larva. A *UAS-GFP* transgene was used to label tracheal cells (left panel). Brightfield images of the same larva show air filling in lumens (middle panel). A cartoon representing the lumenized tube network (cyan) appears in the rightmost panel. (**B-D**) Tracheal tube lumen formation in flies expressing control RNAi (**B**), RNAi directed against *Pdcd10* (**C**), or RNAi directed against *GCKIII* (**D**) under the control of the tracheal-specific *btl-GAL4* driver. Arrowhead (in cartoon panel of **B**) indicates the primary trunk of a tracheal tube (where lumen truncation would indicate a severe phenotype), and arrows indicate the fine terminal branches (where lumen truncation would indicate a mild phenotype). Loss of *Pdcd10* or *GCKIII* results in similar air-filling defects. GFP expressing tracheal cells that lack air-filled lumens are outlined in red on the cartoon panels of **C-D**. Scale bars in (**A**) = 500 μm. Scale bars in (**B-D**) = 200 μm.

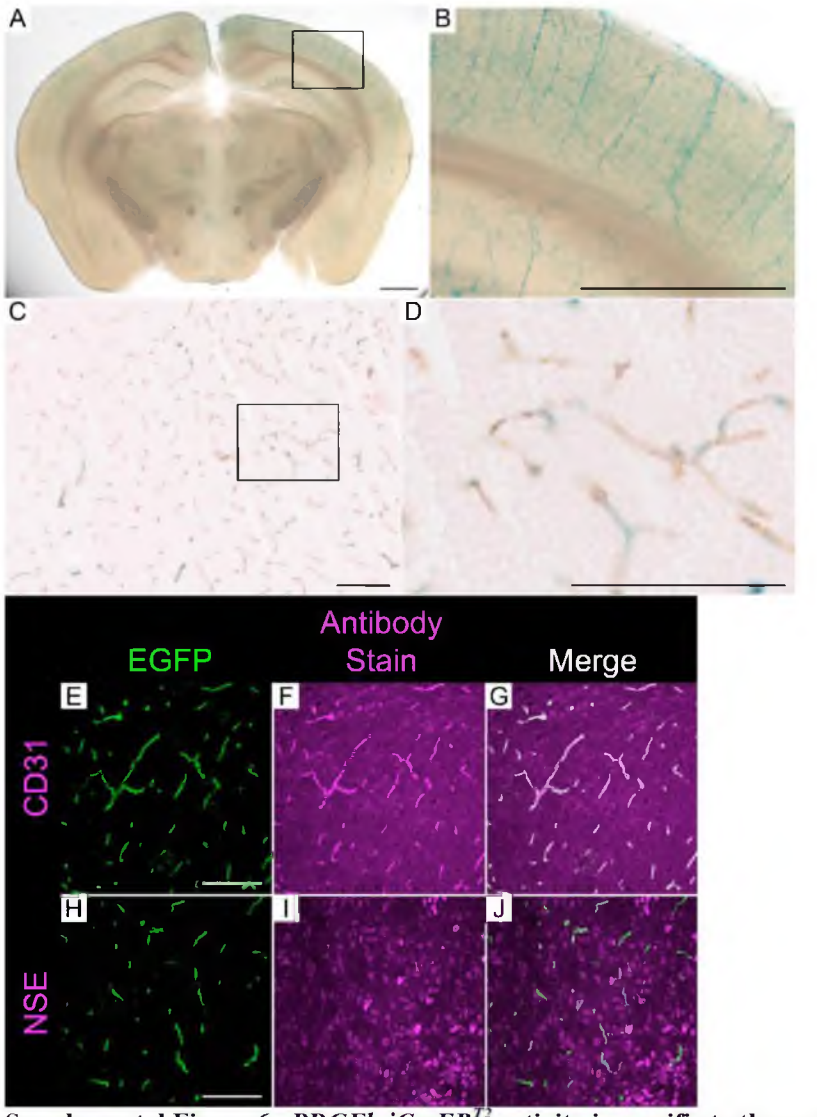


**Supplemental Figure 6. *PDGFb-iCreER$^{T2}$* activity is specific to the endothelium.** (**A**) X-gal staining (blue) of brain from a 6 month old *PDGFb-iCreER$^{T2}$; Rosa26-LacZ* mouse that was given tamoxifen at birth. (**B**) Close-up of the boxed area in panel (**A**). (**C-D**) X-gal (blue) and CD31 (brown) staining of brain from a 6 month old *PDGFb-iCreER$^{T2}$; Rosa26-LacZ* mouse that was given tamoxifen at birth. (**E-G**) CD31 (magenta) staining of brain from a 12 day old *PDGFb-iCreER$^{T2}$; Rosa26-ACTB-tdTomato,-EGFP* mouse that was given tamoxifen at birth. Cre activation converts ubiquitous tomato expression (not shown) to EGFP expression (green). (**H-J**) Neuron-specific enolase (NSE, magenta) staining of brain from a 12 day old *PDGFb-iCreER$^{T2}$; Rosa26-ACTB-tdTomato,-EGFP* mouse that was given tamoxifen at birth. Cre activation converts ubiquitous tomato expression (not shown) to EGFP expression (green). Scale bars in (**A-B**) = 1 mm. Scale bars in (**C-J**) = 100 μm.

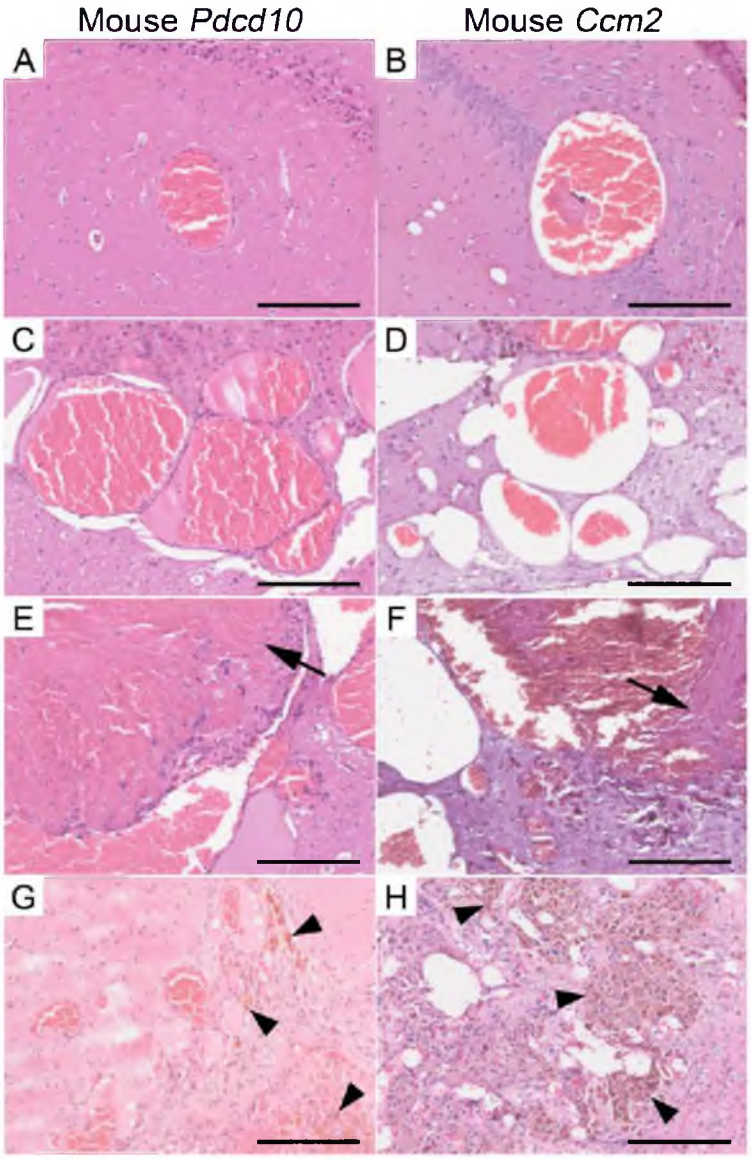


**Supplemental Figure 7. LOH of either *Ccm2* or *Pdcd10* results in a range of vascular malformations.** Both mouse models of CCM exhibit the same spectrum of pathology. Both the *Pdcd10* (**A**, **C**, **E**, and **G**) and *Ccm2* (**B**, **D**, **F**, and **H**) induced endothelial knockout models develop vascular lesions that exhibit the previously described spectrum of CCM pathology. Examples shown here include lesions consistent with solitary telangiectasias (**A-B**), multichannel "pristine" caverns (**C-D**), complex multichannel lesions with organizing thromboses (arrows in **E-F**), and multiple small caverns associated with heavy hemosiderin staining (arrowheads in **G-H**). Scale bars = 200 μm.

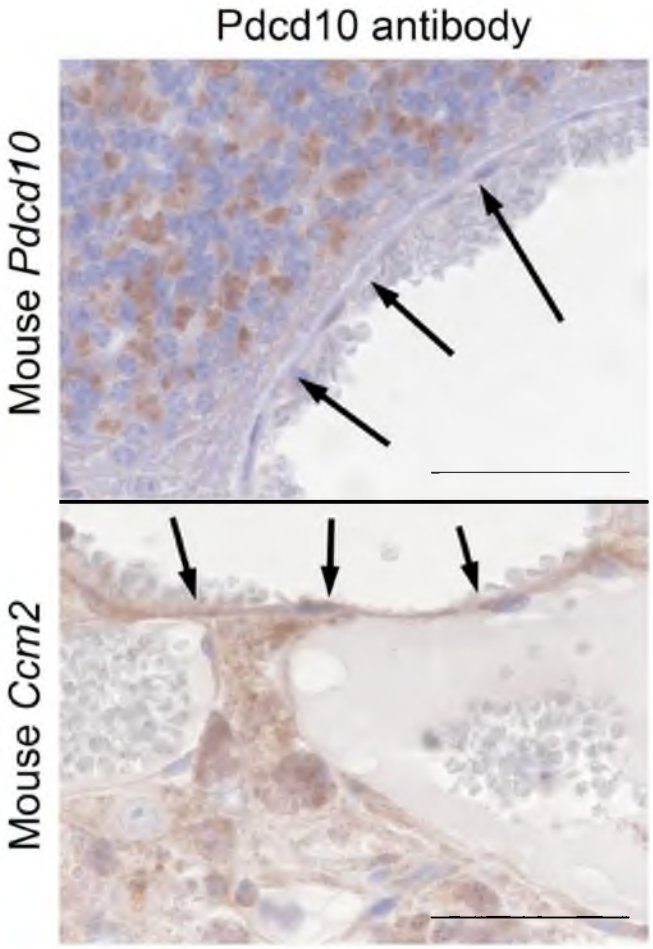


**Supplemental Figure 8. Loss of Pdcd10 protein from *Pdcd10* (but not *Ccm2*) vascular lesions.** An antibody against Pdcd10 does not stain endothelial cells of a CCM lesion from a *Pdcd10* induced knockout mouse (upper panel) but does stain the endothelial cells of a CCM from a *Ccm2* induced knockout mouse (bottom panel). Arrows indicate endothelial cells. Scale bars = 50 μm.

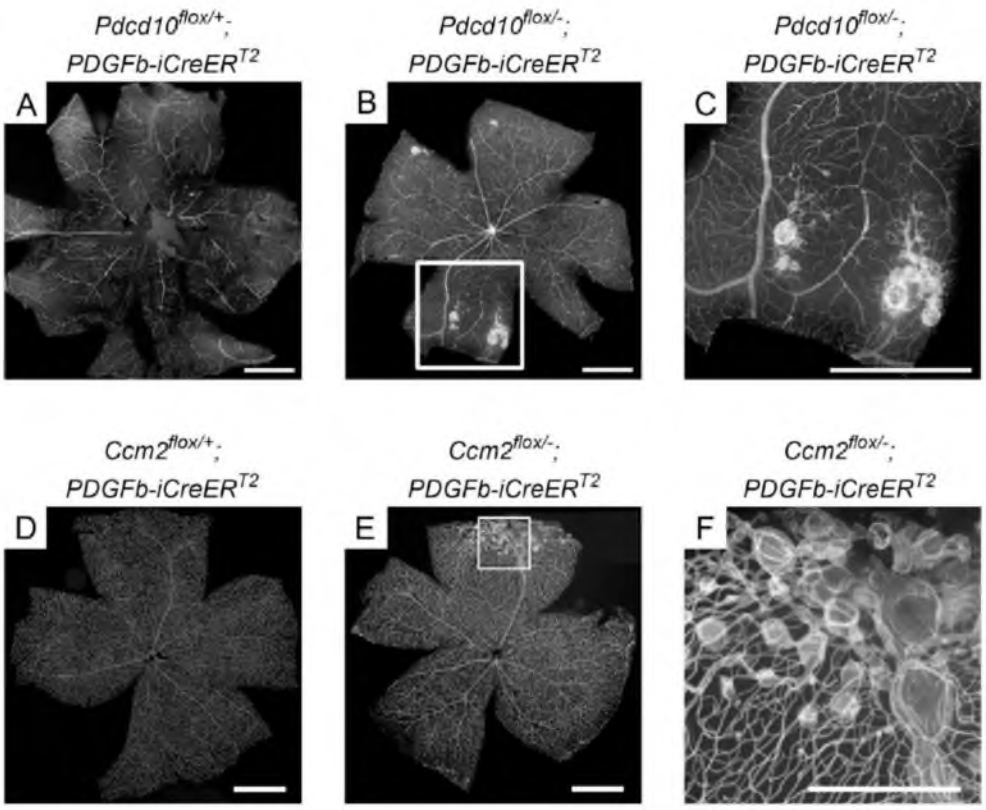


**Supplemental Figure 9. Murine CCMs occur in the retinal vasculature.** Lectin stained retinal flat mounts from a 5 month old *Pdcd10$^{flox/+}$; PDGFb-iCreER$^{T2}$* mouse (**A**), a 5 month old *Pdcd10$^{flox/-}$; PDGFb-iCreER$^{T2}$* mouse (**B-C**), a 7 month old *Ccm2$^{flox/+}$; PDGFb-iCreER$^{T2}$* mouse (**D**), and a 7 month old *Ccm2$^{flox/-}$; PDGFb-iCreER$^{T2}$* mouse (**E-F**). All mice were given tamoxifen at birth. (**C**) Close-up of the boxed, CCM-containing area in (**B**). (**F**) Close-up of the boxed, CCM-containing area in (**E**). Scale bars for all panels = 1 mm, except for panel (**F**), which is 500 μm.

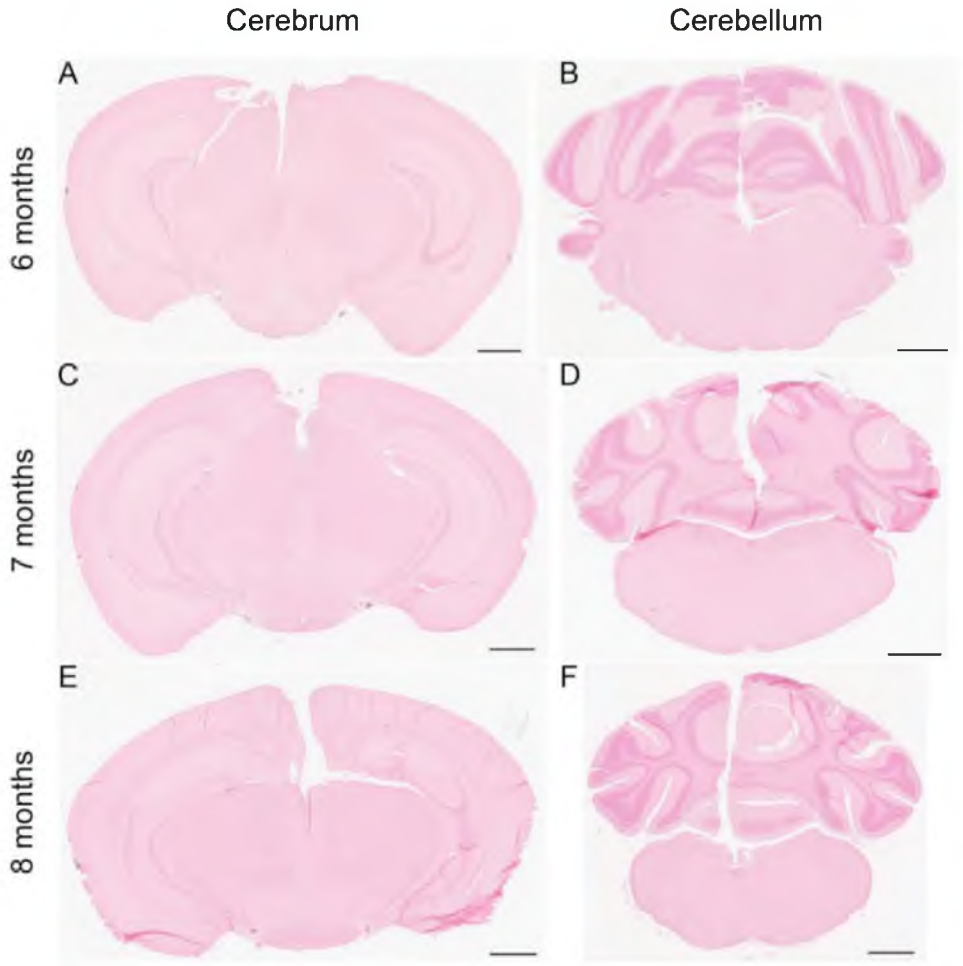


G

| $Ccm2^{flox/-}$; | | CCM postive | CCM negative | Total |
|---|---|---|---|---|
| | *Nestin-Cre* | 0 | 6 | 6 |
| | *PDGFb-iCreER$^{T2}$* | 16 | 0 | 16 |
| | Total | 16 | 6 | 22 |

Fisher's exact test – $p < 0.0001$

**Supplemental Figure 10. Neural-specific deletion of *Ccm2* does not result in CCMs.** (**A-F**) Histology of *$Ccm2^{flox/-}$; Nestin-Cre* mouse brain at 6 months (**A-B**), 7 months (**C-D**), and 8 months (**E-F**). Staining is Prussian blue for hemosiderin with nuclear fast red counterstain. No lesions are found in these brains, and no hemosiderin is apparent. Scale bars = 1 mm. (**G**) Table comparing prevalence of CCMs in neural knockout (*Nestin-Cre*) vs. inducible endothelial knockout (*PDGFb-CreER$^{T2}$*).

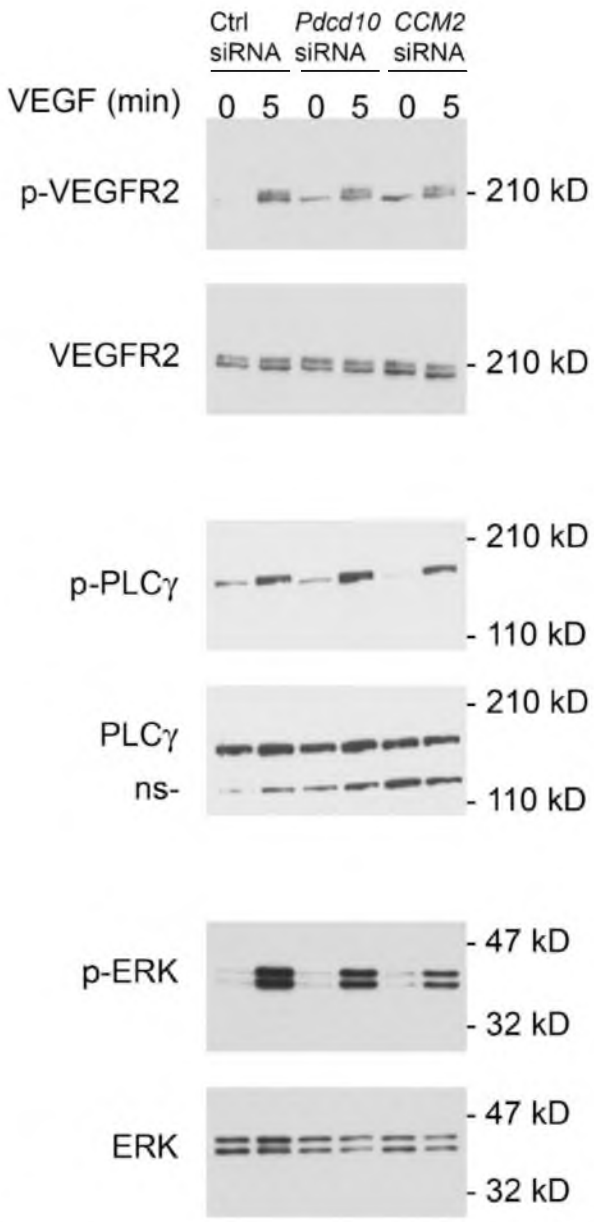


**Supplemental Figure 11. Loss of PDCD10 does not affect VEGFR2-MAPK signaling.** Western blot for VEGFR2, PLCγ, and ERK1/2 phosphorylation after stimulation of HMVECs with 10 ng/mL VEGF for the indicated amounts of time. ns, non-specific band.

| Cross | *Pdcd10*$^{flox/flox}$ X *Pdcd10*$^{+/-}$; *Nestin-Cre* | | | |
|---|---|---|---|---|
| Genotype | *Pdcd10*$^{flox/+}$ | *Pdcd10*$^{flox/-}$ | *Pdcd10*$^{flox/+}$; *Nestin-Cre* | *Pdcd10*$^{flox/-}$; *Nestin-Cre* |
| # of progeny | | | | |
| E12.5 | 2 | 7 | 9 | 8 |
| P1 | 12 | 17 | 7 | 7 |

**Supplemental Table 1.** Table showing numbers of living offspring by genotype in matings between *Pdcd10*$^{flox/flox}$ and *Pdcd10*$^{+/-}$; *Nestin-Cre* parents.

# CHAPTER 5

## A SCALABLE DRUG REPURPOSING PLATFORM FOR A MONOGENIC STROKE DISEASE

There are at least 7,000 diseases designated as rare in the United States[23]. Taken as a whole, at least 25 million Americans are affected by a rare disease[24]. Disease-causing mutations of a single gene account for as many as 5,000 rare diseases, the largest subset[23]. The often arduous quest for a proper diagnosis and treatment by highly specialized practitioners is costly to our healthcare system and for families faced with a rare disease. Further, the high cost of drug development combined with relatively small markets strongly reduced commercial interest in these diseases. The Orphan Drug Act of 1983 and its subsequent amendments created regulatory and economic incentives for drug development in the rare disease space, and there have been major successes both for pharmaceutical companies and for rare-disease patients[23]. However, more than 95% of rare diseases still have no approved treatment[23,24].

An area of excitement and challenge in the pharmaceutical industry is drug repurposing (sometimes referred to as drug rediscovery or drug repositioning), whereby existing drugs are used for additional or alternative indications from those for which they were originally designed or intended[25]. The classic example of drug repurposing is that of sildenafil, intended originally to treat angina, but attaining blockbuster status for the treatment of erectile dysfunction[26]. The vast majority of drug repurposing successes can be attributed to serendipity or to a reasoned approach based on a deep understanding of a specific disease mechanism[25]. While these reasoned approaches may work for well-studied diseases, a complete picture of the molecular mechanisms associated with most rare diseases are lacking. Therefore, development of a scalable platform for drug repurposing with the potential to repurpose drugs across many rare diseases in a near simultaneous fashion would have considerable implications.

Over the past decade, we have studied a monogenic disease, Cerebral Cavernous Malformation (CCM), in an attempt to learn more about the molecular mechanisms underlying vascular stability and with an emphasis on the development of translational research. CCM is a hereditary hemorrhagic stroke

syndrome characterized by the formation of vascular malformations in the central nervous system. CCM lesions are leaky and unstable, with chronic and acute bleeding leading to inflammation and stroke, respectively[27]. The only treatment for CCM is neurosurgical resection[28]. CCM occurs in two forms: sporadic and familial, which together affect as many as 1 in 200 individuals in the United States [29,30]. However, the familial forms together only account for 20% of cases and thus qualify as rare diseases. The familial form of the disease is associated with loss-of-function mutations in one of three genes, *KRIT1, CCM2,* and *PDCD10* [31]. We have previously reported on a target-based drug repurposing strategy for CCM, and we show here results that caused us to rethink our target-centric approach[32]. As a result, we developed an unbiased drug discovery platform for identification of an effective therapeutic for CCM. Here we report on our drug discovery platform, and two drugs we identified as potential treatments for CCM. We demonstrate that both of these compounds successfully reduce CCM lesions in a faithful mouse model of human CCM disease, and further demonstrate that these compounds illuminate the pathophysiology of the disease. We suggest that this drug discovery platform may be scalable to rapid identification of new treatments for many monogenic diseases.

## Results

We and others have identified dysregulation of the small GTPase RHOA in cells lacking KRIT1 or OSM as a possible pathogenic mechanism of CCM disease based on reasoned probing of the molecular mechanisms associated with the disease and a reductionist methodology to target identification[33-35]. Because of that approach, we suggested that statins, which inhibit RHOA activation through antagonistic activity on HMG-CoA reductase, might be repurposed to treat CCM disease[32]. To test this hypothesis, we developed murine genetic models of CCM disease. These mice are compound heterozygous with a loss of function mutation in any one of the three CCM genes (Krit1[36], Osm[37], and Pdcd10[38] ), and a second allele flanked by loxp that can be knocked-out in a postnatal, tissue-specific inducible manner in the endothelium (PDGFb-iCreER$^{T2}$)[39]. Strikingly, these mice develop CCM lesions that reproduce all of the pathologic aspects of human CCM disease. Much to our surprise, four months of simvastatin treatment did not result

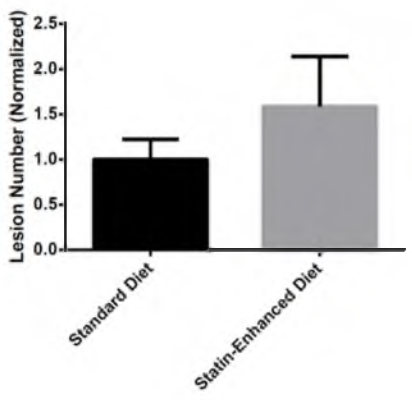


**Figure 5.1: Simvastatin treatment has no effect on lesion burden in a murine model of CCM.** Mice were treated with a diet enhanced with simvastatin for 4 months. At 5 months of age, the lesion number in this group was compared with mice fed a standard control diet using small animal MRI analysis.

in a decreased burden of disease in these mice (Figure 5.1). While potential explanations for this result are myriad and do not exclude a role of RHO activation in CCM pathophysiology, or even of the use of statins as an effective treatment of CCM disease, this result forced us to critically reexamine our preconceived notions about the reductionist target-centric approach to drug discovery we had employed.

We have previously reported that endothelial cells deficient in CCM2 have obvious structural and functional phenotypes[38]. We hypothesized that we could use these phenotypes for unbiased drug discovery. Our strategy was to develop a primary imaging screen based on rescue of the structural defects associated with the loss of CCM2 and an orthogonal secondary screen based upon rescue of functional defects associated with the loss of CCM2 (Figure 5.2). Another important aspect of our strategy was to use a library of 1600 small molecules composed of known drugs and bioactive compounds based upon our hypothesis that hits from this library could more quickly be translated to the bedside.

To develop our high-content imaging primary screen, we first defined a set of imaging constraints. Images would need to (i) support computational recognition of cell nuclei and cell borders, (ii) be captured at a resolution sufficient to allow quantification of structural phenotypes, (iii) be amenable to a 96 or 384-well plate format, and (iv) be highly reproducible. To satisfy these demands, Human Dermal Microvascular Endothelial Cells (HMVEC-D) were treated with CCM2 mRNA-targeting siRNA or a scrambled control, and then seeded into 96-well imaging plates. Large immunofluorescence images were

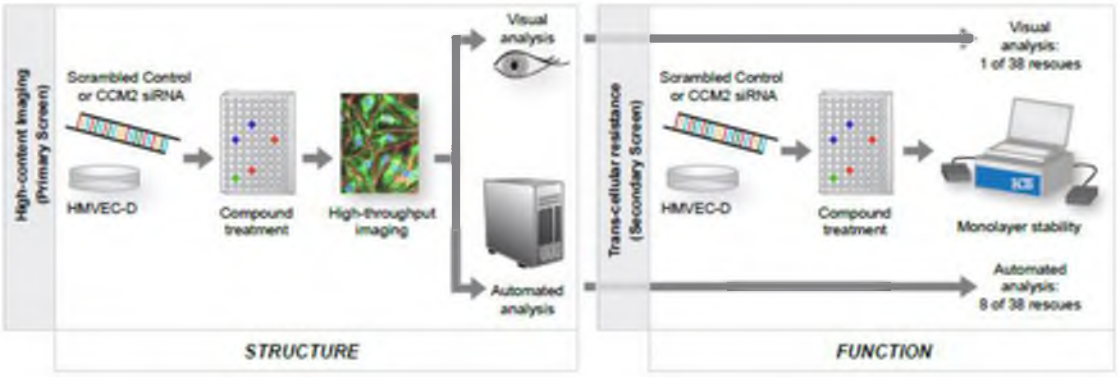


**Figure 5.2: Workflow of chemical suppressor screen**. The primary screen consists of a high-content immunofluorescence-based assay. The secondary screen consists of a nonoptical electrical cell substrate impedance sensing assay. Compounds in the primary screen were analyzed by qualitative human analysis or by automated machine-learning software; compounds identified by the software analysis had a much improved hit-rate in the secondary screen. Our structure-function screening system is amenable to a wide-variety of cell-types and disease states.

captured from each well of a 96-well plate in three channels sufficient to give an impression of the cell structure, including the nucleus, actin stress fibers, and VE-cadherin cell-cell junctions (Figure 5.3a-c and Figure 5.4). A high-throughput microscope developed for phenotypic drug discovery allowed automated imaging of an entire 96-well plate in about 60 minutes. We wrote a custom pipeline in CellProfiler, an open-source image analysis tool from the Broad Institute, to import images, define the borders of each cell, and create a database of a multitude of mathematical descriptors of the structure of each cell (Figure 5.3d and Figure 5.4)[40]. We then used CellProfiler Analyst, a machine-learning tool, to identify rules that could be used to distinguish whether each cell in an image was more likely to have been treated with scrambled control siRNA or siCCM2[41,42]. The software was able to accurately categorize images as 'siCTRL-treated' or 'siCCM2-treated', resulting in a Z' of 0.7, which is considered amenable to high-throughput screening (Figure 5.3e and Figure 5.5) [43].

We then screened 1,600 known drugs to identify those that could rescue the structural phenotype associated with loss of CCM2. We analyzed the resulting images to identify rescue using CellProfiler and CellProfiler Analyst and qualitative analysis by two blinded reviewers as a comparison. Reviewers performing qualitative analysis commonly identified 38 compounds that when added to siCCM2-treated cells resulted in rescue of structural phenotypes (Figure 5.2). We simultaneously ran the images through

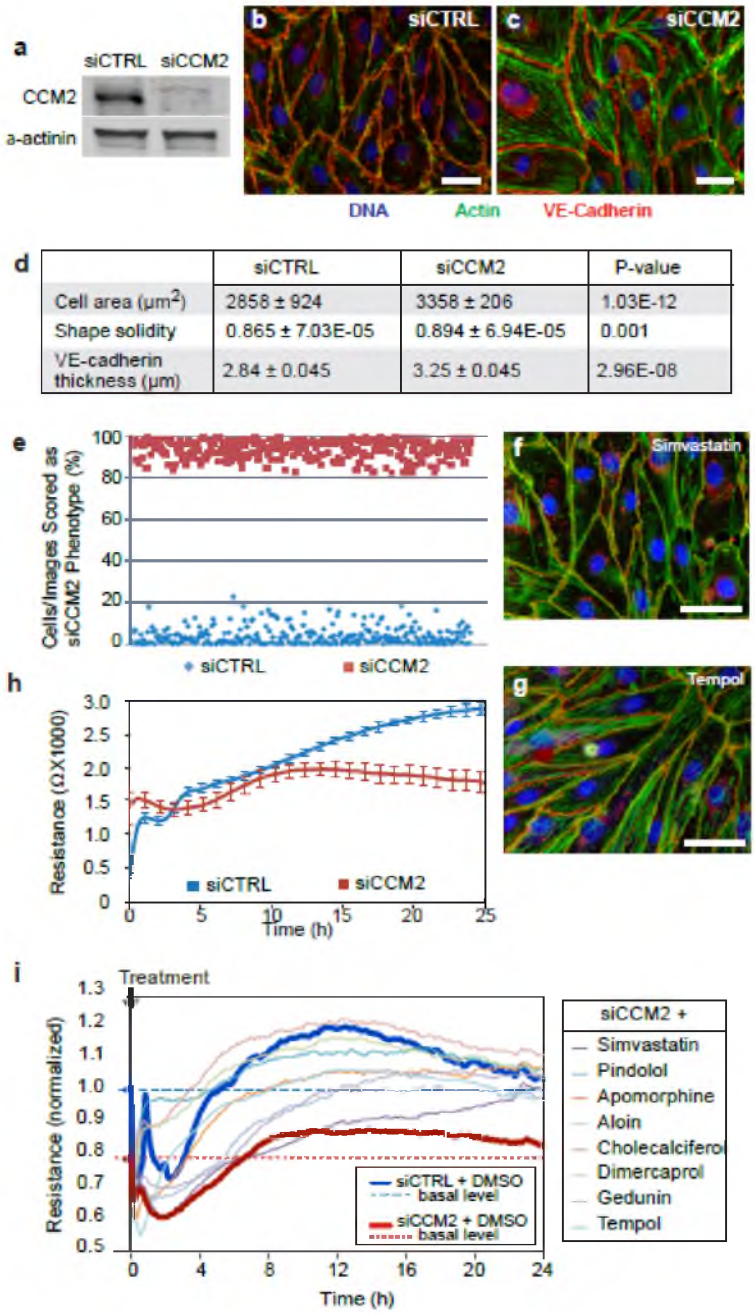


| | siCTRL | siCCM2 | P-value |
|---|---|---|---|
| Cell area (μm²) | 2858 ± 924 | 3358 ± 206 | 1.03E-12 |
| Shape solidity | 0.865 ± 7.03E-05 | 0.894 ± 6.94E-05 | 0.001 |
| VE-cadherin thickness (μm) | 2.84 ± 0.045 | 3.25 ± 0.045 | 2.96E-08 |

**Figure 5.3: Structural and functional phenotypes associated with loss of CCM2.** (**a**) CCM2 was knocked down at least 80% in all assays as determined by western blot. (**b**) Endothelial cells treated with scrambled siRNA show a typical cobblestone monolayer phenotype with cortical actin (green) and VE-cadherin (red) at cell-cell borders, and a paucity of actin stress fibers. (**c**) Endothelial cells treated with CCM2 siRNA show an obvious cytoskeletal phenotype with a large number of actin stress fibers, decreased cortical actin, and increased cell-size. (**d**) Quantification of various parameters from thousands of cells. (**e**) Validation of machine-learning software to correctly classify images. Example primary hit from (**f**) qualitative or (**G**) automated analysis of the high-content imaging screen. (**h**) siCTRL treated cells reach and maintain a higher level of ECIS resistance compared to siCCM2-treated cells. (**i**) Eight compounds significantly improve barrier function in endothelial cells deficient in CCM2 after 24-hours of treatment. Scale bars = 50 μm. All graphs depict mean ± SD.

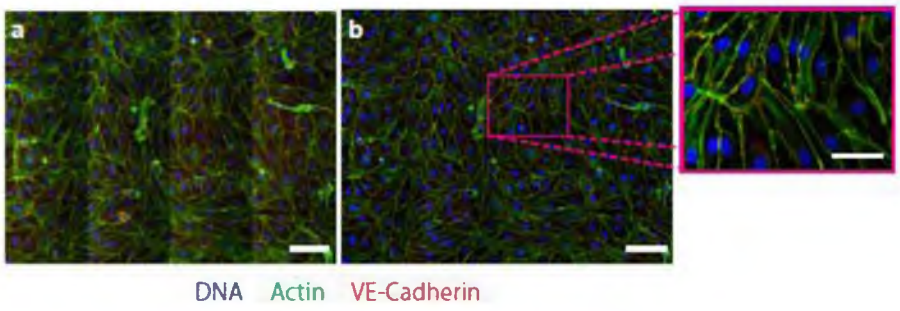


**Figure 5.4: Large image quality control.** (**a**) raw 4x4 montage image obtained using the BD Pathway Bioimager without correction filters. (**b**) The same image after correction filters were applied using CellProfiler software to eliminate montage and light-path artifacts. The inset demonstrates the high-resolution of these large montage images. Scale bars represent 100 µM or 50 µM (inset).

the CellProfiler software system, and we selected the 38 compounds that quantitatively rescued the structural phenotype most (Figure 5.2). Interestingly, there was no overlap between the compounds selected by human analysis and those selected by our automated computational scoring system.

To validate our hits and prioritize future analysis, we developed a secondary orthogonal screen using trans-cellular resistance based on the functional defect in monolayer stability in cells deficient in CCM2[33]. Trans-endothelial resistance works by taking real-time measurements of the resistance encountered when an electrical current is passed between electrodes upon which cells are growing[44]. Using this trans-endothelial resistance assay, we simultaneously screened the two sets of 38 compounds identified by our manual and automated image analysis approaches in our primary screen. Of the 38 compounds selected by human analysis, only one compound (simvastatin) showed any significant rescue of the defect in monolayer stability of cells treated with siCCM2. Excitingly, 7 of the 38 compounds identified using our automated machine-learning analysis showed full or partial rescue of the same phenotype (Figure 5.3g). The eight compounds identified in our secondary screen include compounds from classes previously connected to CCM disease, as well as novel compounds (Figure 5.6).

Due to the time and cost associated with chronic treatment trials in our CCM mouse model, we first took advantage of a microvascular leak phenotype in our mice to quickly prioritize our hits for chronic treatment models. We found that our endothelial specific *Ccm2* knockout mouse (*Ccm2*$^{f/-}$; *Pdgfb-iCreER*$^{T2,+/-}$) had increased dermal vascular leak as measured by a modified Miles assay compared to wild-type

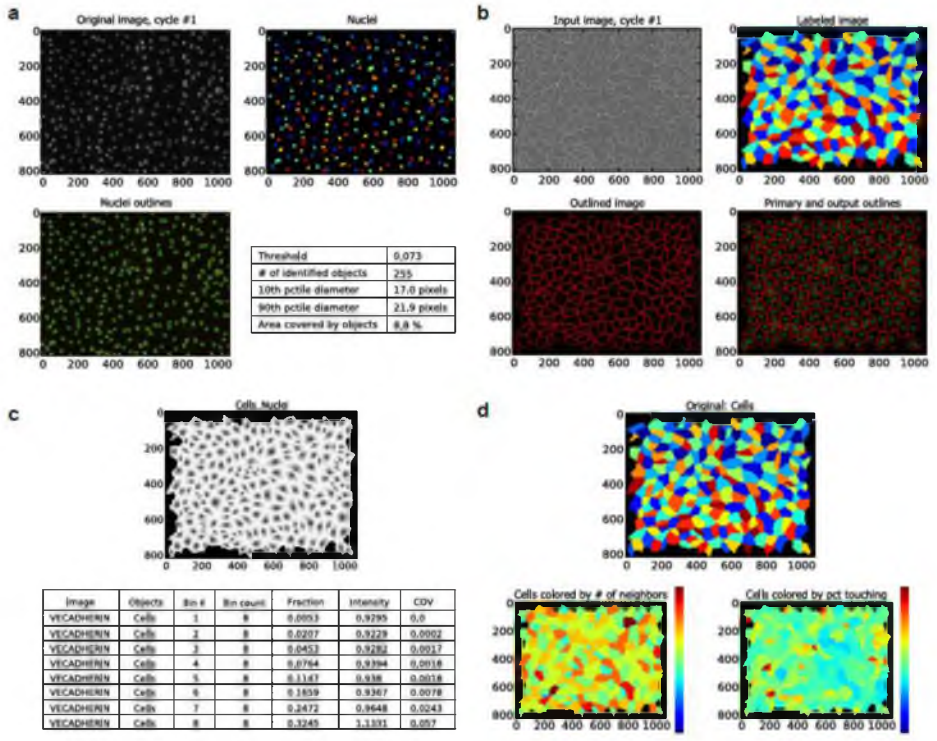


**Figure 5.5: Software analysis of immunofluorescence images.** (**a**) DAPI images are used to seed a database with primary elements called 'nuclei' which are then represented as unique by false coloration. (**b**) VE-cadherin images are used to detect cell-cell borders delineating the border separating the cytoplasm surrounding each 'nuclei', thereby establishing the individual 'cell' elements in each image, also represented as unique by false coloration. Calculations are made for each 'cell' for a wide variety of mathematical descriptors, including (**c**) the radial distribution of VE-cadherin in each cell, and (**d**) the number of neighbors and percent of cell borders touching other cells.

controls (*Ccm2*$^{f/+}$; *Pdgfb-iCreER*$^{T2, -/-}$). When we injected small intradermal wheals of a subset of our hit compounds into these mice, we found that only tempol and cholecalciferol significantly reduced peri-injection microvascular leakiness (Figure 5.7). We do not exclude the possibility that the other compounds could be relevant therapeutic candidates for the treatment of CCM disease, but we elected to prioritize tempol and cholecalciferol for further study.

Next, we performed chronic treatment studies of the effects of tempol and cholecalciferol in our inducible endothelial-specific *Ccm2* knockout mouse (*Ccm2*$^{f/-}$; *Pdgfb-iCreER*$^{T2}$)[38]. These studies would serve not just to evaluate the potential of these treatments for CCM disease, but as a litmus test for the power of our screening platform. Nursing mothers were treated with either standard chow (1.5 IU/g

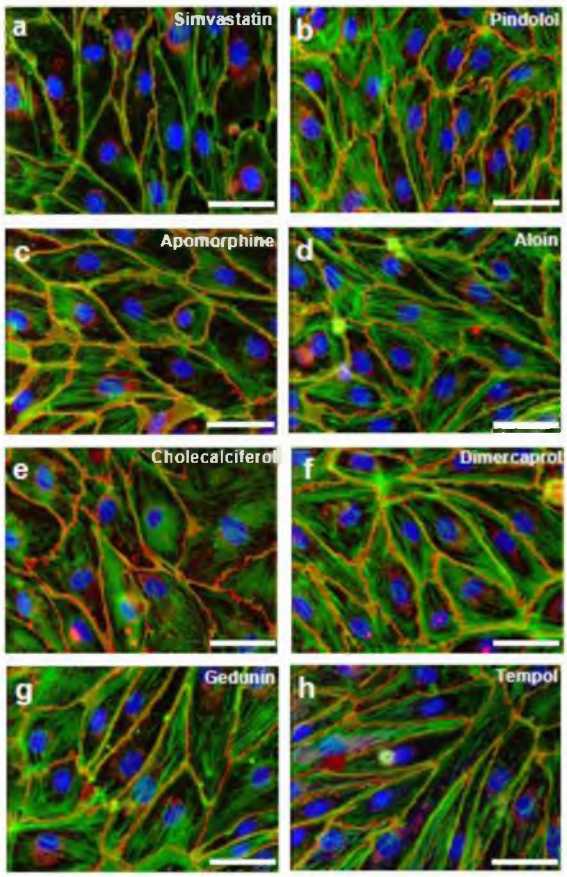


**Figure 5.6: Hits from secondary screen.** Drug candidates were identified using (**a**) qualitative human analysis or (**b-h**) automated machine learning algorithms that subsequently rescued a functional monolayer defect in the secondary screen. Scale bars represent 50 μM.

cholecalciferol), an identical chow enhanced with cholecalciferol (25 IU/g), or standard chow plus tempol dissolved in drinking water (1mM) starting 5 days after delivery of their pups. Treatment with a cholecalciferol-enhanced diet resulted in significantly different levels of the serum marker of cholecalciferol, 25(OH)$D_3$, in pups by weaning (Figure 5.8). After weaning, mice were fed the same diet as their mother until 5 months of age, a point at which 100% of endothelial specific *Ccm2* knockout mice have cerebrovascular lesions detectable by MRI. At this time, mice were evaluated for lesion status. Two blinded reviewers independently evaluated the number and size of CCM lesions using MRI; mice receiving the diet enriched with $D_3$ or tempol had approximately half as many lesions and half the lesion area compared to those receiving standard chow (Figure 5.9a,b). The effect of cholecalciferol and tempol

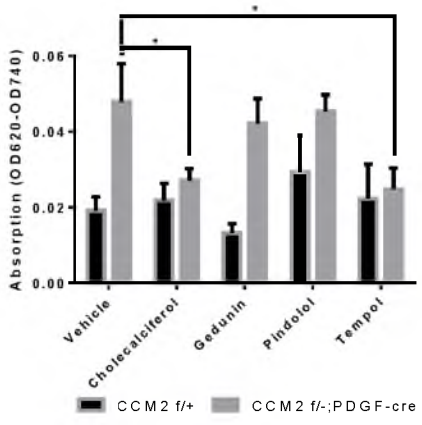


**Figure 5.7:** ***In vivo*** **validation of candidates in a mouse model of CCM**. Quantification of dermal permeability 1.5 hours after an intradermal injection of DMSO, cholecalciferol, gedunin, pindolol, or tempol and 30 minutes after intravenous administration of Evans blue dye. At least 12 mice per group were tested. All graphs depict mean ± SEM. * denotes $P<0.05$

supplementation was qualitatively obvious when comparing MRI-based three-dimensional reconstructions of representative brains and lesions (Figure 5.9c-e).

A major advantage of screening with a library of known drugs and bioactive factors is that a large body of research is generally available regarding the effects of any one of the compounds. Therefore, each validated hit has the potential to immediately inform the pathophysiology under investigation. Further, reagents and probes are more readily available for further study for such compounds.

With knowledge of the various biologic roles of cholecalciferol and other forms of vitamin D at hand, we assessed the timing of the effects of cholecalciferol on the endothelium. We found that knockdown of CCM2 led to increased activation of various pathways relevant to endothelial stability, including transforming protein RhoA (RHOA), phosphorylation of myosin light chain (pMLC), and ADP-ribosylation factor 6 (ARF6) (Figure 5.10a-c). Subsequently, we determined that treatment of monolayers with cholecalciferol, even at a lower physiologic dose (100 nm), inhibited the CCM2 knockdown-induced activation of RHOA, pMLC, and ARF6**.** We further examined the effect of cholecalciferol on ARF6 activation, finding inhibition to occur within 5 minutes in cells induced by loss of CCM2 (Figure 5.10d-e). Knockdown of CCM2 did not affect activation of other proteins known to be important in endothelial stability, including cell division control protein 42 homolog (CDC42), Ras-related C3 botulinum toxin

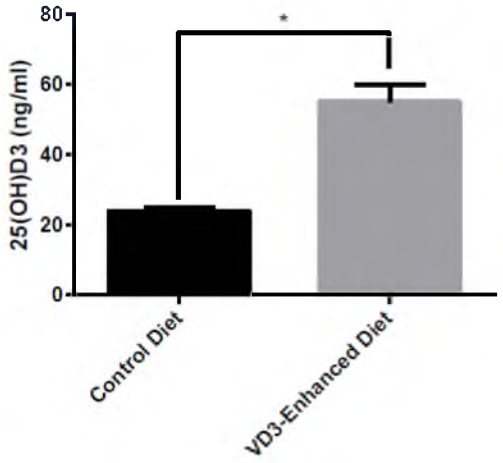


**Figure 5.8: A cholecalciferol-enhanced diet promotes increased 25(OH)$D_3$ levels before weaning.** At 5 days after birth, litters were randomized to receive either standard chow (1.5 IU/g $D_3$) or cholecalciferol-enhanced chow (25 IU/g $D_3$). Because pups have not been weaned at this time-point, the indicated food was provided to the mother. Levels of the cholecalciferol metabolite, 25(OH)$D_3$, were measured at P21, the day of weaning, and indicate that 16 days of dietary modification via mother's breast milk can significantly increase 25(OH)$D_3$ levels in pups. All bars represent mean ± SEM. * indicates $P<0.05$.

substrate 1 (RAC1), or Ras-related protein R-Ras (RRAS); nor did treatment of up to 10 μM cholecalciferol basally inhibit activation of these markers (Figure 5.11). Taken together, these data suggest that cholecalciferol, even at physiologic doses, can rapidly inhibit multiple key intracellular signaling pathways that play a role in endothelial activation in the context of mutation-induced destabilization. These data shed light on CCM, and also inform the study of cholecalciferol, which has not previously been shown to have these specific effects on cell signaling.

The specific target of our second hit, tempol, is superoxide scavenging. Indeed, a role of oxidative stress in the pathophysiology of CCM disease due to two other causative genes, KRIT1 and PDCD10, has been reported[45-47]. In cell culture, loss of CCM2 induced increased ROS and decreased FOX01 expression, suggesting a potential common mechanism of CCM pathophysiology as has been proposed for KRIT1 (Figure 5.10)[45]. These results, and previous work in the field, led us to hypothesize that oxidative stress may be a driving force in CCM at the level of individual cells and may also have broader effects on the physiology of small vessels through effects on endothelial vasodilation[48]. To test this hypothesis, we isolated murine middle cerebral arteries from our endothelial-specific CCM2 knockout mice, and measured both endothelial-dependent and endothelial-independent vasodilation[49]. We found that endothelial-specific loss of CCM2 resulted in a significant defect in endothelial-dependent vasodilation in our model, which

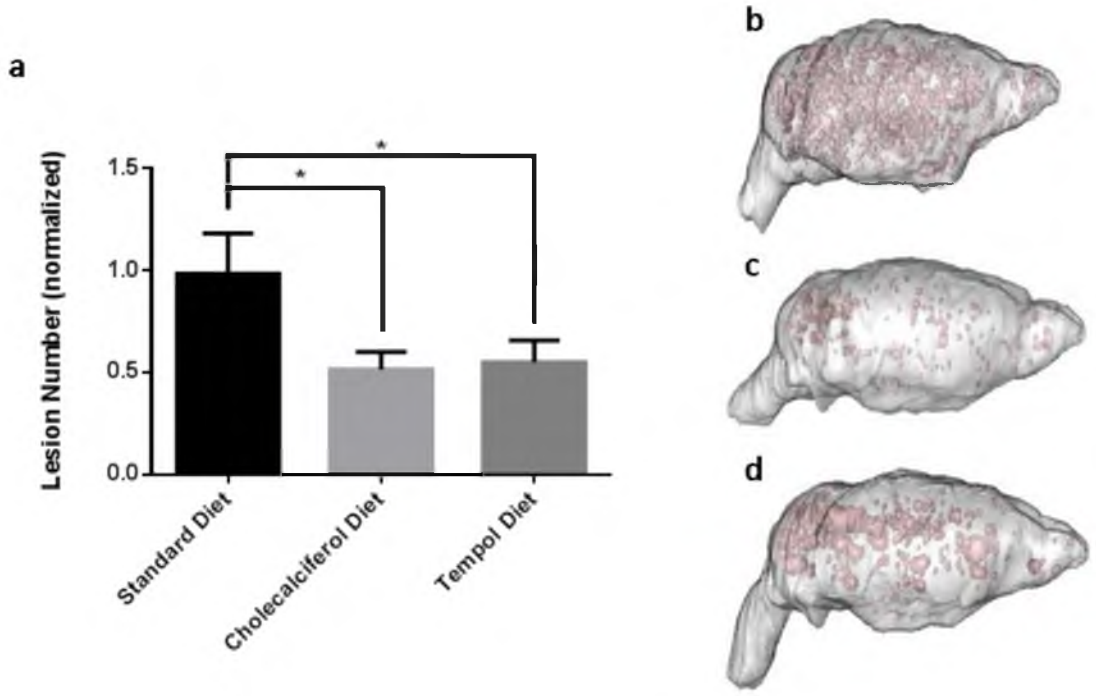


**Figure 5.9: Treatment with cholecalciferol or tempol reduces lesion severity in a CCM mouse model.** (**a**) Endothelial-specific *Ccm2* knockout mice fed a diet high in cholecalciferol or tempol had fewer CCM-like lesions in the brain after 5 months as measured by MRI. Three-dimensional reconstructions from MRI data of the brains of mice with the median number of lesions from (**b**) the untreated group, (**c**) the cholecalciferol treated group, or (**d**) the tempol treated group demonstrate the qualitative reduction in lesions (red). Experiment represents at least N=8 mice per group. All graphs depict mean ± SEM. * denotes $P<0.05$

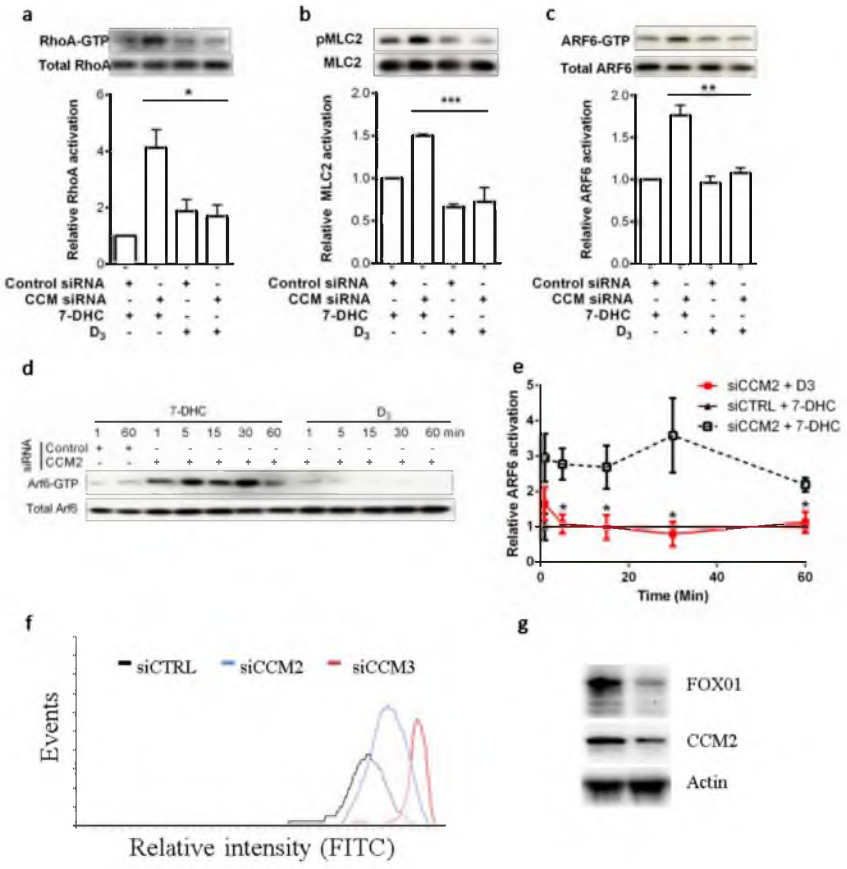


**Figure 5.10: Treatments illuminate pathophysiology of disease.** 60-minute treatment with 100 nM cholecalciferol, but not its precursor 7-DHC, rescues CCM2 knockdown-induced (**a**) RHOA, (**b**) pMLC, and (**c**) ARF6 activation. (**d**) Cholecalciferol rescues CCM2-induced activation of ARF6 within 5 minutes. (**e**) Quantification of (d). (f) Knockdown of CCM2 in EAHY cells induces increased reactive oxygen species. (g) Knockdown of CCM2 in XYZ cells induces a reduction of FOX01 expression. All graphs depict mean ± SEM. * denotes P<0.05, ** denotes P<0.01, and *** denotes P<0.001

could be completely rescued by tempol (Figure 5.12a-d). Additionally, both systolic and diastolic blood pressure were increased in the endothelial knockout mice (Figure 5.12e-g), consistent with constricted, non-responsive vessels. Interestingly, heart rate of the endothelial knockouts was lower than in control mice (Figure 5.12h). Taken together, these data suggest that CCM2 could play an important role in regulating cellular functions directly related to the endothelium, and that dysregulation of these functions may cause perturbances to important organ-level hemodynamic systems. These results have potential implications for understanding the pathophysiology of CCM disease, and suggest that hemodynamics in patients with CCM should be monitored closely.

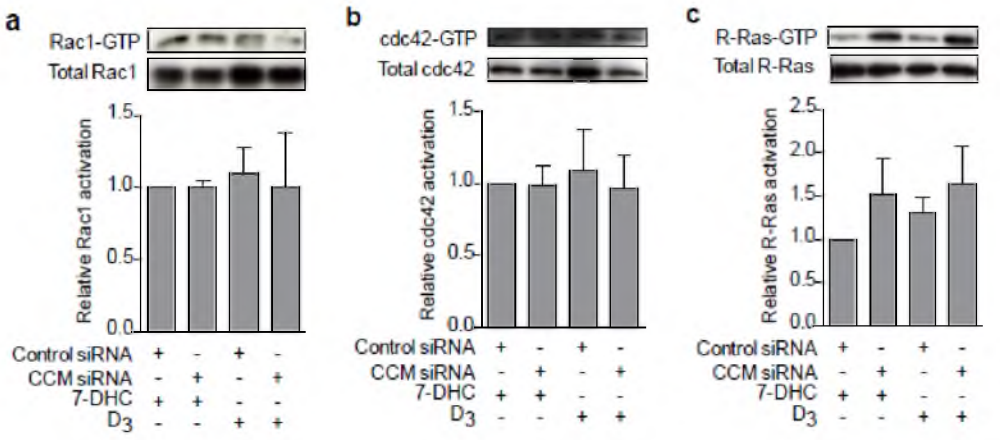


**Figure 5.11: Cholecalciferol has no effect on the activation of certain destabilizing pathways in the endothelium.** 60-minute treatment with 10 μM cholecalciferol had no effect on activation of (**a**) RAC1, (**b**) CDC-42, or (**c**) R-RAS in endothelial cells. All bars represent mean ± SEM.

As a result of our repurposing strategy, we identified not only potential treatments of CCM disease, but also informed the study of the molecular mechanisms of the disease. Further, the compounds we identified are associated with specific biomarkers that may aid in the evaluation of CCM disease.

## Methods

**Reagents.** Primary human adult dermal microvascular endothelial cells (HMVEC-D) and cell culture reagents were obtained from Lonza (Basel, Switzerland). Small interfering RNA (siRNA) were obtained from Dharmacon Thermo Scientific (Waltham, MA). The Spectrum Collection compound library was obtained from MicroSource Discovery Systems (Gaylordsville, CT), via the University of Utah Drug Screening Resource. 7-DHC was obtained from Sigma-Aldrich (St. Louis, MO). All remaining reagents were obtained from Tocris Biosciences (Bristol, U.K.) unless otherwise stated.

**Cell culture.** Four individual lots of Adult Dermal Human Microvascular Endothelial Cells (HMVEC-D) were pooled at passage 0 and expanded according to manufacturer's instructions in EBM-2 media (Lonza) supplemented with EGM-2 MV Bulletkits (Lonza). After two expansions, cells were frozen in identical lots at $1x10^6$ cells/mL for use in all screening experiments. Individual lots of HMVEC-D were expanded as described above and utilized for all mechanism experiments. All *in vitro* experiments were completed using endothelial cells between passage 3 and 6. The continuous human endothelial cell line

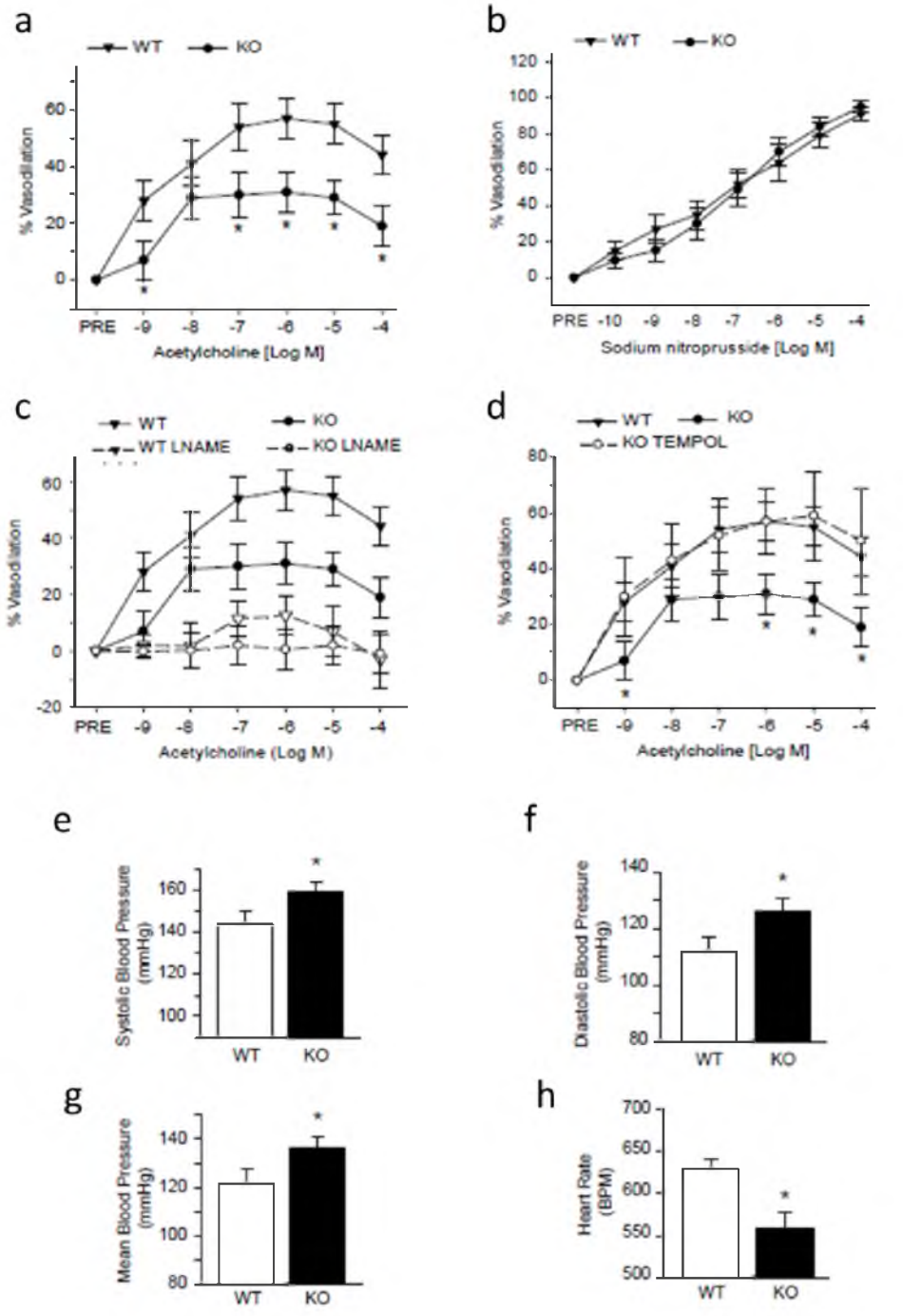


**Figure 5.12: CCM mice display endothelial-dependent vascular dysfunction.** (**a**) Middle cerebral arteries isolated from endothelial-specific CCM2 knockout mice (KO) subjected to acetylcholine-induced vasodilation. (**b**) Sodium Nitroprusside treatment (an NO-donor) of middle cerebral arteries of both mice genotypes demonstrates the normal function of the smooth muscle in both wild-type and knockout mice. (**c**) L-name, a specific inhibitor of eNOS, eliminates the ability of endothelial cells to produce NO. (**d**) Tempol completely rescues acetylcholine-induced vasodilation in endothelial-specific CCM2 knockout mice. (**e**) Systolic, (**f**) diastolic, (**g**) and mean blood pressure were elevated in CCM2 knockout mice, consistent with decreased vasodilatory function. (**h**) Heart rate was increased in the CCM2 knockout mice. All panels depict mean ± SEM. * denotes $P<0.05$

EA-hy926 was maintained according to the protocol provided by the distributor (ATCC cat. CRL 2922, Manassas, Virginia, USA). Specifically, cells were cultured in DMEM medium with 25 mM glucose (HG) supplemented with 10% fetal bovine serum (FBS), 2 mM L-glutamine, and 2% HAT supplement.

**Endothelial transfection.** ON-TARGETplus siRNA targeting CCM2 (5' GGAAUUGUCUCGCCAUUUA 3') or a scrambled control was obtained from Dharmacon. Endothelial cell transfection with siRNA was carried out as previously described[7]. Briefly, cells were passaged into 25nM siRNA with 1:166 HiPerFect reagent (Qiagen) in 4:1 EGM-2 MV to EBM-2, respectively, and plated. After an overnight incubation in the transfection mix, cells were washed and fed with EGM-2 MV. After an additional 48 hours, the transfection process was repeated to achieve more complete knockdown. During the second transfection, cells were seeded into assay plates as described elsewhere. Cells were again fed with EGM-2 MV after overnight incubation with the transfection mix. After an additional 48-72 hours, cells were subjected to experimental conditions.

**EA-hy926 transfection.** EA-hy926 endothelial cells ($1x10^6$) were plated in 10 cm culture dishes in 8 ml antibiotic-free standard growth medium supplemented with FBS. Cells were grown to 60% confluence and then transfected for 5 h at 37°C with either CCM2, CCM3, or control siRNAs (final concentration: 100 nmol/L). Specifically, silencing experiments were performed using CCM2 and CCM3 siRNAs from Dharmacon (Dharmacon ON Target Plus J-014728-05-0050 and J-004436-05-0050, respectively). Cell transfections were performed using INTERFERin kit (Polyplus transfection, New York, NY, USA) according to the manufacturer's protocol. Cells were cultured with siRNAs for 24 h before treatments and analysis.

**Immunofluorescence imaging:** 96-well imaging plates (BD Falcon) were used for immunofluorescent imaging screening. Cells were fixed with 4% paraformaldehyde in PBS for 10 minutes, washed 3x in ultrasaline (Lonza), then incubated overnight with mouse anti-human CD144 antibody (BD Biosciences). Cells were washed 3x with ultrasaline, then a mixture of Hoescht 33342, Alexa-Fluor 488 Phalloidin (Invitrogen), and Alexa-fluor 594 goat anti-mouse antibody in ultrasaline were added for 6 hours. After an additional 3 washes, 200 µl ultrasaline was added to each well, and then the plates were covered with adhesive foil and immediately imaged. 96-well imaging plates were imaged using a high-throughput BD Pathway 855 Bioimager. A custom macro was written using the Attovision

software (BD) encompassing imaging autofocus at each well, followed by acquisition of each channel. Each image consisted of a 4x4 montage using a 40x objective, covering a total area of 810 x 600 μm in each well. Images were automatically saved, and each plate was changed by hand when imaging was complete.

**Automated image analysis.** Images were analyzed using CellProfiler and CellProfiler Analyst. A custom CellProfiler pipeline imported all images, applied a light correction filter, and decreased the size of the images to reduce imaging time. The Hoescht channel was first utilized to identify nuclei using an Otsu Global thresholding method. The VE-cadherin channel was utilized next to identify cell-cell borders again using an Otsu Global thresholding method minimizing entropy. A threshold correction factor of 0.7 and a regularization factor of 0.001 were used. Cells not completely enclosed within the image were excluded from analysis. A variety of quantifications were calculated and recorded for each cell, including co-localization of each channel, radial localization of actin and VE-cadherin, texture of actin and VE-cadherin, nuclear and cell shape characteristics, etc. These quantifications were stored in a database accessible by CellProfiler Analyst. CellProfiler Analyst was subsequently used to open 100 control images (siCTRL or siCCM2 treated). Approximately 100 cells were selected at random from each control image and added to categorization bins if qualitatively meeting their respective prototypic phenotype. This process was repeated until approximately 10,000 cells comprised each bin; positive (siCCM2) and negative (siCTRL). Subsequently, rules were automatically developed using machine-learning algorithms to sort these cell populations based on their quantitative descriptions (as previously calculated for each cell and stored in MySQL database). Previously unused control images (siCTRL or siCCM2 treated) were then evaluated using the rules, and obvious miscategorization of cells was corrected. Cells not meeting the prototypic phenotype for a given treatment were not evaluated. After rule refinement and minimization, images from wells treated with each screen compound were evaluated. Compounds changing the score of an siCCM2-treated well to within three standard deviations of the siCTRL-treated mean score in both N=1 and N=2 of the primary screen were considered hits (n=38).

**Drug treatment.** Compounds were obtained in 100% DMSO at 2 mM concentration in 96-well polypropylene assay plates from the University of Utah Drug Screening Resource Core and kept frozen at -20°C. Libraries acquired included the Microsource Spectrum Library of exactly 2000 known drugs and

bioactive compounds. At the time of treatment, drugs were added to 96-well imaging plates containing confluent siCCM2 treated HMVEC-D endothelial monolayers using a 12-channel electronic pipette (Eppendorf Xplorer) at final concentration of 10uM, 0.5% DMSO (vehicle) in starvation media (EBM-2 + 0.2% bovine serum albumin) and gently mixed. Positive (siCCM2) and negative (siCTRL) control wells received 0.5% DMSO in starvation media without any compound treatment. Follow-up experiments were performed using the highest available grade of reagent from Tocris or Sigma.

**Electric cell substrate impedance sensing.** For screening applications, a 96-well ECIS plate (96W10E+, Applied Biophysics) was used. At the second siRNA transfection, HMVEC-D were seeded at $4x10^4$ cell/well. Plates were monitored using an ECIS Zθ system (Applied Biophysics) to measure impedance of an alternating current across the cell monolayer. Resistance was normalized for each well to just before treatment, and was plotted in real time. Cells were fed according to the same schedule as in the transfection protocol. 72 hours after the second siRNA transfection, compounds were added to each well at a final concentration of 10 μM in 0.5% DMSO.

**Mouse strains.** Mice used have been previously reported [11,16]. Briefly, a construct for the conditional *Ccm2* allele was derive from genomic sequence data from a BAC clone (RP22 library, Invitrogen). The construct extended from a *Sal*I site 5' of exon 3 through a *Bam*HI site 3' of exon 10. All mice were backcrossed into the C57BL/6J strain. *PDGFb-iCreER*$^{T2}$ mice were generously provided by Marcus Fruttiger (University College London Institute of Ophthalmology, London, United Kingdom) via Holger Gerhardt (London Research Institute – Cancer Research UK, London, United Kingdom). Genotypes were determined by PCR analysis of genomic DNA isolated from ear biopsies using previously described primers. Tamoxifen (Sigma-Aldrich) was resuspended in corn oil (Sigma-Aldrich), and 40 ng was given as an intraperitoneal injection to mouse pups on perinatal day 1. 'Control' and 'Wild-type' mice were CCM2$^{f/+}$ and tamoxifen-treated (but without PDGF-cre).

**Dermal permeability.** We performed a modification of a previously described Miles Assay [14]. Male mice between 2 and 4 months of age were anesthetized with isoflurane and their backs gently shaved and depilated using a hair-removal cream. The mice were then gently washed and allowed to recover. The following day, the mice were again anesthetized with isoflurane and 20 μL intradermal injections of treatments (50 uM in 0.5% DMSO in sterile saline) in various positions on the back. 90 minutes later, we

performed tail vein injections of Evans blue dye (100 µL of 1% dye in sterile saline, Sigma). After 30 minutes, mice were sacrificed and equal-sized skin biopsies from each injection site were collected and placed in formamide (Invitrogen) overnight at 60˚C. Absorbance at 620 nm (measurement of blue dye) and 740 nm (to normalize for any blood in the sample) was used to quantify the amount of Evans blue dye in each sample. The absorbance is reported with the standard error of the mean.

**Murine CCM lesion formation and MRI analysis.** At 5 days after birth (P5), litters were assigned to either a standard chow (Harlan 2018, 1.5 IU/g $D_3$) or $D_3$ enhanced chow (Harlan 2018 + 25 IU/g $D_3$). The chow was provided to the mother of each litter until the mice were weaned at P21. Mice from each litter continued on their respective diets until 5 months of age. At 5 months of age, mice were sacrificed by exsanguination (blood was collected for later analysis), and subsequent perfusion with saline and then 4% formalin. Brains were dissected from the skull. Postmortem MRI scanning was subsequently performed. A gradient recalled echo sequence was used to acquire coronal slices spanning the whole brain. Sequence parameters were as follows: repetition time, 328 ms; echo time, 5.4 ms; flip-angle, 40°; 12 averages, in-plane-resolution, 125 µm × 125 µm; and slice thickness, 0.5 mm. For a representative subset of brains, high-resolution 3D gradient echo was acquired using the following parameters: isotropic voxel size of 78 µm × 78 µm × 78 µm over 9 hours. Other sequence parameters were as follows: repetition time, 250 ms; echo time, 7.5 ms; flip angle, 30°; and 2 averages. Lesion area and number were quantified by multiple blind reviewers using ImageJ and Osirix software. 3D reconstructions were assembled using Osirix software by a blinded reviewer.

**Middle cerebral artery endothelial function.** Endothelial function assays are based upon previously published methods[26]. Middle cerebral artery endothelial function was performed as previously described. Mice (N=7-14/group) were euthanized via exsanguinations by cardiac puncture while under isoflurane anesthesia. Right and left middle cerebral arteries approximately 100-120 micrometers in luminal diameter were excised from the brain and placed in myograph chambers (DMT A/S, Aarhus, Denmark) containing EDTA-buffered physiological saline solution (PSS), cannulated onto glass micropipettes and secured with nylon (11–0) suture. Once cannulated, the middle cerebral arteries were warmed to 37˚C and pressurized to 60 mmHg intraluminal pressure and allowed to equilibrate for 1 h. All arteries were then submaximally preconstricted with phenylephrine (2 µM). Increases in luminal diameter

in response to increasing concentrations of the endothelium-dependent dilator acetylcholine (Ach; 1×10−9 to 1×10−4 M) in the absence or presence of the nitric oxide synthase inhibitor, L-NAME (0.1 mmol/L, 30 min) or the superoxide scavenger, TEMPOL (1 mmol/L, 60 min) was assessed. Endothelium-independent dilation to sodium nitroprusside (SNP: 1x10-10 to 1x10-4 mol/L) also was determined (5). Arterial segments were imaged and diameters measured by an automated edge detection; VAS software (DMT A/S, Aarhus, Denmark). All dose response data are presented as a percent of possible dilation after phenylephrine preconstriction.

**Noninvasive blood pressure measurements in conscious mice.** Murine blood pressures were noninvasively measured by determining the tail blood volume with a volume pressure recording (VPR) sensor and an occlusion tail-cuff (CODA System, Kent Scientific, Torrington, CT) as previously described in detail. This method has been previously validated versus arterial catheter blood pressure. Blood pressure and heart rate recordings were made in a quiet and warm (24 C) environment. Mice were placed in restrainers on a heating unit and given 15-20 minutes to acclimate and reach a steady body temperature (30-35 C). Each session consisted of 5-10 acclimatization measurements; if those measures were stable, they were followed by 20 experimental measures. Measures with aberrant movement/behavior or inadequate volume pressure measures were treated as outliers. Averages from each session were used for systolic blood pressure, diastolic blood pressure, mean blood pressure, and heart rate for each individual mouse.

**Mouse experiments.** All mouse experiments were approved by the University of Utah Institutional Animal Care and Use Committee or the George E. Wahlen Department of Veterans Affairs Medical Center Institutional Animal Care and Use Committee. Measures of serum 25(OH)$D_3$ were made by ARUP clinical laboratories using standard clinical assays.

**Biochemical assays.** Wild-type, siCTRL or siCCM2 treated HMVEC-D cells were incubated with either 100 nM or 10μM cholecalciferol (Tocris), 7-DHC (Sigma) or vehicle (0.5% DMSO) for 60 minutes (pMLC, ARF6, RAC, CDC42, RRAS) or 24 hours (RHOA), unless otherwise indicated. After treatment, the cells were washed with ice-cold PBS and lysed in 50mM Tris pH 7.4, 150mM NaCl, 10mM MgCl2, 10% Glycerol, 1% NP-40, 1X protease inhibitors, and 1X phosphatase inhibitors. For RhoA, ARF6, Rac1 /cdc42 and R-Ras activation assays, crude total cell lysate were generated and GTP-RhoA, ARF6, Rac1/ cdc42 and R-Ras were precipitated with Rhotekin-RBD (Millipore), GGA3-PBD (Cell

Biolabs), PAK-1-PBD (Millipore), and Raf-1 RBD, respectively. Following three washes with lysis buffer, bound proteins were eluted with 2X sample buffer. RhoA, ARF6, Rac1 /cdc42, and R-Ras were detected by western blotting with antibodies (RhoA, Rac1, and R-Ras antibody are from Cell Signaling, ARF6, and cad42 antibody are from Millipore). Each blot is representative of at least three independent experiments, for which quantification is shown.

**Fluorimetric intracellular ROS detection.** Briefly, EA-hy926 cells grown to confluence in complete medium were washed twice with PBS, incubated with 2',7'-dichlorfluorescein-diacetate (DCFH-DA) at a final concentration of 5μM in PBS at 37°C for 30 minutes and analyzed by Tali image based cytometer (Invitrogen). Raw data were elaborated by Flowing software (v. 2.5.0, by Perttu Terho, University of Turku, Finland).

**Statistics.** Data presented are mean ± SEM unless otherwise indicated. Statistical significance is indicated generally by a single symbol (i.e. *) to indicate $P < 0.05$, two symbols (i.e. **) to indicate $P < 0.01$, three symbols (i.e. ***) to indicate $P < 0.001$, and so on. Standard statistical analysis was used. For comparisons of two groups, a Student's T-test was performed. For comparison of more than three groups, 1-way ANOVA with Tukey's or Bonferroni's multiple comparison post hoc analysis was utilized. For comparison of data with at least two grouping variables, a two way ANOVA was used. Significance was set at $P < 0.05$ for all experiments.

# CHAPTER 6

## CONCLUDING REMARKS

During my time as a graduate student in the laboratory of Dr. Dean Y. Li, I have had the privilege to work on a number of projects. Through my investigation of the role of elastin in the endothelialization of intravascular devices, to my investigation of the role of the small GTPase ARF6 in both vascular stability and vascular mechanotransduction, I have been building a suite of tools that would enable me to use the mouse model of CCM disease we developed to perform translational research to try to bring drugs to patients with CCM disease. This final project, identification of two new treatments for CCM disease, was the culmination of all of my work detailed in Chapters 1-4. In Chapter 5, I laid out my final major work, in which we conceived and implemented a high-content screen querying both structural and functional cellular phenotypes to discover novel factors active in the CCM2 pathway. We combined high-content imaging, machine-learning software, as well as trans-cellular electrical resistance measurements as efficient and powerful tools for drug screening. We specifically focused on known drugs and bioactive compounds because we believe such drugs have a much higher chance of making a rapid impact on patient outcomes. By focusing on such molecules, our high-tech screening method, which combines advances in molecular biology, imaging, and computing, has led to a low-tech solution: the potential for a modulatory role of an inexpensive widely-available drug with a wide safety margin on a disease for which no pharmaceutical intervention has yet been approved.

Of particular excitement to us are recent advances by other groups who have expanded our understanding of the pathophysiology of CCM disease and who have, in some cases, put forth potential treatments for the disease. In particular, recent evidence suggests that endothelial to mesenchymal transition (endMT) plays a critical role in the pathophysiology of CCM disease[31]. Through inhibition of TGF-β, a key driver of endMT, reduction in severity of disease in a mouse model of CCM disease was identified. Interestingly, the target of tempol, oxidative stress, drives and is driven by increased TGF-β signaling and endMT[32]. Additionally, metabolites of cholecalciferol have also been shown to strongly

inhibit TGF-β signaling and epithelial-mesenchymal transition (EMT)[33,34]. We have also shown here that RHOA activation, proposed by us and others as critical in CCM pathophysiology, is inhibited by both cholecalciferol and tempol. Taken together, these studies suggest that both compounds identified in a completely unbiased manner in our screen could be inhibiting pathways previously shown to be critical for CCM pathogenesis. The accessibility of cholecalciferol at trivial cost to patients, and the myriad clinical trials underway in the United States for tempol in a variety of conditions suggest that one or both of these drugs could be rapidly applied to the treatment of CCM disease. Moreover, their identification provides an avenue toward discovery of additional molecular mechanisms relevant to CCM disease.

Future work will determine whether our findings, obtained in both human endothelial cells and a mouse model of CCM disease, will fully translate to humans with CCM disease. Our findings underline major priorities upon which the field must agree. Specifically, success of any clinical trial, especially in rare disease research, hinges upon well-studied natural history and clinically meaningful endpoints. The long-term sustainability of treatment often also relies on establishment of relevant biomarkers. In advance of, or in conjunction with, human clinical trials for cholecalciferol or tempol treatment, our work strongly supports immediate amendment of research protocols on human patients with CCM to include measurement of both $25(OH)D_3$ and an agreeable marker of oxidative stress. We must also develop widely-acceptable standards for tracking the natural history of CCM, including specific imaging modalities, lesion evaluation, and symptom assessment. We must use these standards as a platform by which to perform both observational and interventional studies of and CCM disease and treatments such as cholecalciferol. As with any rare condition, the probability of success is exponentially enhanced by agreement and adherence of the field to specific protocols so that data can be aggregated across clinical sites.

Finally, the opportunities to easily adapt the screening system described herein to effectively search for new therapies for a large and diverse set of monogenic diseases is perhaps the most exciting aspect of this project. By combining the platform we propose here with libraries of repurposable drugs, we are hopeful that we and others can quickly and efficiently bring new treatments to patients with many monogenic loss of function diseases that otherwise may not be the target of pharmaceutical discovery. However, we must be strategic in this approach; our success in identifying novel treatments for CCM was

and will continue to be enabled by a strong animal model and a reasonably strong understanding of the natural history of the disease. Therefore, our expansion of this unbiased drug discovery platform to other monogenic diseases will require us to selectively apply a bias toward studying those diseases in which strong preclinical models and clinical knowledge exist. Some might argue that though this platform has the potential to affect many diseases, the reach of the system in terms of the total number of patients affected might be low. This would be to ignore, however, that rare diseases have a proven track record of enabling the study of, and treatments developed for, some of the most widely used drugs in medicine[35].

REFERENCES


1. Lloyd-Jones, D., *et al.* Heart Disease and Stroke Statistics--2010 Update. A Report From the American Heart Association. *Circulation* (2009).

2. Glagov, S., Zarins, C., Giddens, D.P. & Ku, D.N. Hemodynamics and atherosclerosis. Insights and perspectives gained from studies of human arteries. *Arch Pathol Lab Med* **112**, 1018-1031 (1988).

3. Conway, D.E., Williams, M.R., Eskin, S.G. & McIntire, L.V. Endothelial cell responses to atheroprone flow are driven by two separate flow components, low time-average shear stress and fluid flow reversal. *Am J Physiol Heart Circ Physiol* (2009).

4. Mohan, S., Mohan, N. & Sprague, E.A. Differential activation of NF-kappa B in human aortic endothelial cells conditioned to specific flow environments. *Am J Physiol* **273**, C572-578 (1997).

5. Hoger, J.H., Ilyin, V.I., Forsyth, S. & Hoger, A. Shear stress regulates the endothelial Kir2.1 ion channel. *Proc Natl Acad Sci U S A* **99**, 7780-7785 (2002).

6. Tzima, E., del Pozo, M.A., Shattil, S.J., Chien, S. & Schwartz, M.A. Activation of integrins in endothelial cells by fluid shear stress mediates Rho-dependent cytoskeletal alignment. *EMBO J* **20**, 4639-4647 (2001).

7. Otte, L.A., *et al.* Rapid changes in shear stress induce dissociation of a G alpha(q/11)-platelet endothelial cell adhesion molecule-1 complex. *J Physiol* **587**, 2365-2373 (2009).

8. Smith, M.L., Long, D.S., Damiano, E.R. & Ley, K. Near-wall micro-PIV reveals a hydrodynamically relevant endothelial surface layer in venules in vivo. *Biophys J* **85**, 637-645 (2003).

9. Van der Heiden, K., *et al.* Endothelial primary cilia in areas of disturbed flow are at the base of atherosclerosis. *Atherosclerosis* **196**, 542-550 (2008).

10. Chiu, J.J., Usami, S. & Chien, S. Vascular endothelial responses to altered shear stress: pathologic implications for atherosclerosis. *Ann Med* **41**, 19-28 (2009).

11. Tzima, E., *et al.* A mechanosensory complex that mediates the endothelial cell response to fluid shear stress. *Nature* **437**, 426-431 (2005).

12. Chien, S. Effects of disturbed flow on endothelial cells. *Ann Biomed Eng* **36**, 554-562 (2008).

13. Dekker, R.J., *et al.* Prolonged fluid shear stress induces a distinct set of endothelial cell genes, most specifically lung Kruppel-like factor (KLF2). *Blood* **100**, 1689-1698 (2002).

14. Shyy, Y.J., Hsieh, H.J., Usami, S. & Chien, S. Fluid shear stress induces a biphasic response of human monocyte chemotactic protein 1 gene expression in vascular endothelium. *Proc Natl Acad Sci U S A* **91**, 4678-4682 (1994).

15. Chiu, J.J., *et al.* Analysis of the effect of disturbed flow on monocytic adhesion to endothelial cells. *J Biomech* **36**, 1883-1895 (2003).

16. Harry, B.L., *et al.* Endothelial cell PECAM-1 promotes atherosclerotic lesions in areas of disturbed flow in ApoE-deficient mice. *Arterioscler Thromb Vasc Biol* **28**, 2003-2008 (2008).

17. Biswas, P., *et al.* PECAM-1 affects GSK-3beta-mediated beta-catenin phosphorylation and degradation. *Am J Pathol* **169**, 314-324 (2006).

18. Park, K.W., *et al.* Robo4 is a vascular-specific receptor that inhibits endothelial migration. *Dev Biol* **261**, 251-267 (2003).

19. Jones, C.A., *et al.* Robo4 stabilizes the vascular network by inhibiting pathologic angiogenesis and endothelial hyperpermeability. *Nat Med* **14**, 448-453 (2008).

20. Jones, C.A., *et al.* Slit2-Robo4 signalling promotes vascular stability by blocking Arf6 activity. *Nature cell biology* **11**, 1325-1331 (2009).

21. Turner, C.E. Paxillin. *Int J Biochem Cell Biol* **30**, 955-959 (1998).

22. Frangos, J.A., Eskin, S.G., McIntire, L.V. & Ives, C.L. Flow effects on prostacyclin production by cultured human endothelial cells. *Science* **227**, 1477-1479 (1985).

23. Field, M.J., Boat, T.F., Institute of Medicine (U.S.). Committee on Accelerating Rare Diseases Research and Orphan Product Development. & National Academies Press (U.S.). *Rare diseases and orphan products : accelerating research and development*, (National Academies Press, Washington, D.C., 2010).

24. Rinaldi, A. Adopting an orphan. *EMBO reports* **6**, 507-510 (2005).

25. Boguski, M.S., Mandl, K.D. & Sukhatme, V.P. Drug discovery. Repurposing with a difference. *Science* **324**, 1394-1395 (2009).

26. Ghofrani, H.A., Osterloh, I.H. & Grimminger, F. Sildenafil: from angina to erectile dysfunction to pulmonary hypertension and beyond. *Nature reviews. Drug discovery* **5**, 689-702 (2006).

27. Gault, J., Sarin, H., Awadallah, N.A., Shenkar, R. & Awad, I.A. Pathobiology of human cerebrovascular malformations: basic mechanisms and clinical relevance. *Neurosurgery* **55**, 1-16; discussion 16-17 (2004).

28. Batra, S., Lin, D., Recinos, P.F., Zhang, J. & Rigamonti, D. Cavernous malformations: natural history, diagnosis and treatment. *Nat Rev Neurol* **5**, 659-670 (2009).

29. Otten P, P.G., Rilliet B, Berney J. A propos de 131 cas d'angiomes caverneux (cavernomes) du S.N.C. reperes par l'analyse retrospective de 24535 autopsies. *Neurochirurgie* **35**, 82-83 (1989).

30. Vernooij, M.W., *et al.* Incidental findings on brain MRI in the general population. *N Engl J Med* **357**, 1821-1828 (2007).

31. Riant, F., Bergametti, F., Ayrignac, X., Boulday, G. & Tournier-Lasserve, E. Recent insights into cerebral cavernous malformations: the molecular genetics of CCM. *FEBS J* **277**, 1070-1075 (2010).

32. Li, D.Y. & Whitehead, K.J. Evaluating strategies for the treatment of cerebral cavernous malformations. *Stroke* **41**, S92-94 (2010).

33. Whitehead, K.J., *et al.* The cerebral cavernous malformation signaling pathway promotes vascular integrity via Rho GTPases. *Nat Med* **15**, 177-184 (2009).

34. Stockton, R.A., Shenkar, R., Awad, I.A. & Ginsberg, M.H. Cerebral cavernous malformations proteins inhibit Rho kinase to stabilize vascular integrity. *The Journal of experimental medicine* **207**, 881-896 (2010).

35. Borikova, A.L., *et al.* Rho kinase inhibition rescues the endothelial cell cerebral cavernous malformation phenotype. *J Biol Chem* **285**, 11760-11764 (2010).

36. Whitehead, K.J., Plummer, N.W., Adams, J.A., Marchuk, D.A. & Li, D.Y. Ccm1 is required for arterial morphogenesis: implications for the etiology of human cavernous malformations. *Development* **131**, 1437-1448 (2004).

37. Whitehead, K.J., *et al.* The cerebral cavernous malformation signaling pathway promotes vascular integrity via Rho GTPases. *Nat Med* **15**, 177-184 (2009).

38. Chan, A.C., *et al.* Mutations in 2 distinct genetic pathways result in cerebral cavernous malformations in mice. *J Clin Invest* **121**, 1871-1881 (2011).

39. Claxton, S., *et al.* Efficient, inducible Cre-recombinase activation in vascular endothelium. *Genesis* **46**, 74-80 (2008).

40. Carpenter, A.E., *et al.* CellProfiler: image analysis software for identifying and quantifying cell phenotypes. *Genome Biol* **7**, R100 (2006).

41. Jones, T.R., *et al.* Scoring diverse cellular morphologies in image-based screens with iterative feedback and machine learning. *Proc Natl Acad Sci U S A* **106**, 1826-1831 (2009).

42. Jones, T.R., *et al.* CellProfiler Analyst: data exploration and analysis software for complex image-based screens. *BMC Bioinformatics* **9**, 482 (2008).

43. Zhang, J.H., Chung, T.D. & Oldenburg, K.R. A Simple Statistical Parameter for Use in Evaluation and Validation of High Throughput Screening Assays. *J Biomol Screen* **4**, 67-73 (1999).

44. Wegener, J., Keese, C.R. & Giaever, I. Electric cell-substrate impedance sensing (ECIS) as a noninvasive means to monitor the kinetics of cell spreading to artificial surfaces. *Experimental cell research* **259**, 158-166 (2000).

45. Goitre, L., *et al.* KRIT1 regulates the homeostasis of intracellular reactive oxygen species. *PLoS One* **5**, e11786 (2010).

46. Guazzi, P., *et al.* Identification of the Kelch family protein Nd1-L as a novel molecular interactor of KRIT1. *PLoS One* **7**, e44705 (2012).

47. Fidalgo, M., *et al.* CCM3/PDCD10 stabilizes GCKIII proteins to promote Golgi assembly and cell orientation. *Journal of cell science* **123**, 1274-1284 (2010).

48. Durrant, J.R., *et al.* Voluntary wheel running restores endothelial function in conduit arteries of old mice: direct evidence for reduced oxidative stress, increased superoxide dismutase activity and down-regulation of NADPH oxidase. *J Physiol* **587**, 3271-3285 (2009).

49. Rippe, C., *et al.* Short-term calorie restriction reverses vascular endothelial dysfunction in old mice by increasing nitric oxide and reducing oxidative stress. *Aging Cell* **9**, 304-312 (2010).

CURRICULUM VITA

Christopher C. Gibson
Chris.Gibson@hsc.utah.edu

## *Education*

| | |
|---|---|
| *2009-Present* | The University of Utah. Salt Lake City, Utah.<br>**Doctor of Medicine** and **Doctor of Philosophy in Biomedical Engineering, expected May 2016** |
| *2005-2009* | The University of Texas Health Science Center at San Antonio and the University of Texas at San Antonio. San Antonio, Texas.<br>Courses toward combined MD/PhD degree. |
| *2001- 2005* | Rice University. Houston, Texas.<br>**Bachelors of Science in Bioengineering**<br>**Bachelors of Arts in Managerial Studies - Honors Program** |

## *Research Experience*

| | |
|---|---|
| *2009-Present* | **Graduate Research Assistant**<br>Dean Y. Li, M.D., Ph.D. and Yan-Ting Shiu, Ph.D. (co-advisors).<br>*University of Utah, Department of Bioengineering*<br>Project 1 – Development of novel structure/function screening systems for drug discovery and applications of this technology for the identification of therapeutics for diseases related to vascular stability.<br>Project 2 – Blunting acute endothelial cell mechanotransduction using neural-guidance cues to stabilize the vasculature. |
| *2006 – 2009* | **Graduate Research Assistant**<br>Rena Bizios, Ph.D.<br>*University of Texas at San Antonio, Department of Biomedical Engineering*<br>Setup new lab and purchased major equipment. Completed review of the use of growth factors in modulating cell-material interactions. |
| *2006* | **Graduate Research Assistant**<br>Dr. Jeffrey Y. Thompson<br>*University of Texas at San Antonio, Department of Biomedical Engineering*<br>Setup new lab and purchased major equipment. Completed studies for dental industry consultation. |
| *2004-2005* | **Senior Design and Research Project**<br>Dr. Michael Liebschner<br>*Rice University, Department of Bioengineering*<br>Development of a vibration and compression countermeasure device for bone and muscle loss in microgravity environments. |

*Summer 2002* **Field Researcher**
Dr. Barry Sullender
*Rice University, Department of Ecology and Evolutionary Biology*
Independent research project studying the effects of parasite loads on non-native *B. marinus* toads in tropical Mexico.

## *Research Publications and Reports*

**Gibson, C.C.,** Zhu, W., Davis, C.T., Bowman-Kirigin, J.A., Chan, A.C., Ling, J., Shiu, Y.T., Whitehead, K..J., Li, D.Y., Vitamin D directly stabilizes the endothelium and suppresses a hereditary stroke syndrome. (Submitted)
Wilkins, J.R., **Gibson, C.C.,** Pike, D.B., Iwamoto, M.N., Kubota, A., Shiu, Y.T., Roles of cyclic stretch and actin filaments in bFGF-mediated sprouting angiogenesis. (Submitted).
Wilkins, J.R., **Gibson, C.C.,** Pike, D.B., Iwamoto, M.N., Kubota, A., Shiu, Y.T. Differential effects of cyclic stretch on bFGF- and VEGF-induced sprouting angiogenesis. (Submitted).
Wilkins, J.R., Pike, D.B., **Gibson, C.C.,** Li, L., Shiu, Y.T., The interplay of cyclic stretch and vascular endothelial growth factor in regulating angiogenesis. (Submitted).
Zhu, W.*, London, N.R.*, **Gibson, C.C.***, Tong, Z., Sorenson, L.K., Shi, D.S., Guo, J., Davis, C.T., Smith, M.C.P., Grossmann, A.H., Thomas, K.R., Li, D.Y. Interleukin receptor activates a MyD88-ARNO-ARF6 cascade to disrupt vascular stability. **Nature**. 492: 252-255. 2012
***Co-First Authors**

Jones, C.F., Campbell, R.A., Franks, Z., **Gibson, C.C.,** Thiagarajan, G., Vieira-de-Abreu, A., Sukavaneshvar, S., Mohammad, S.F., Li, D.Y., Ghandehari, H., Weyrich, A.S., Brooks, B.D., Grainger, D.W. Cationic PAMAM dendrimers disrupt key platelet functions. **Molecular Pharmaceutics**. 4:9(6): 1599-1611. 2012.
Chan, A.C., Drakos, S.G., Ruiz, O.E., Smith, A.C.H., **Gibson, C.C.**, Ling, J., Passi, S.F., Stratman, A.N., Sacharidou, A., Revelo, M.P., Grossmann, A.H., Diakos, N.A., Davis, G.E., Metzstein, M.M.m Whitehead, K.J., Li, D.Y. Mutations in 2 distinct genetic pathways result in cerebral cavernous malformation in mice. **Journal of Clinical Investigation**, 121(5): 1871-1881. 2011
Wilson, B.D.*, **Gibson, C.C.***, Sorensen, L.K., Guilhermier, M.Y., Clinger, M., Kelley, L.L., Shiu, Y.T., Li, D.Y. Novel Approach for Endothelializing Vascular Devices: Understanding and Exploiting Elastin-Endothelial Interactions. **Annals of Biomedical Engineering** 39(1): 337-346. 2011
***Co-First Authors**

**Gibson, C.C.**, Puleo, D.A., Bizios, R. "Cell and Tissue Interactions with Materials: The Role of Growth Factors." in Biological Interactions on Material Surfaces. Ed. Puleo, D.A., Bizios, R. Springer. (2009).

## *Presentations and Posters*

**Gibson, C.C.**, Davis, C.T., Ling, J., Shiu, Y.T., Lesniewski, L.A., Donato, A.J., Whitehead, K.J., Li, D.Y. "A High-Content Screen Identifies Novel Therapeutics for a Hereditary Stroke Syndrome" University of Utah Research Trainee Symposium. Deer Valley, Utah. September 13th, 2012.
**Gibson, C.C.**, McCullagh, J.P., Mleynek, T.M., Shiu, Y.T., Lesniewski, L.A., Donato, A.J., Whitehead, K.J., Li, D.Y. "CCM2 Regulates Superoxide and Nitric Oxide in the Endothelium" International Angioma Alliance Meeting. Paris, France. November 17th, 2011.
Melia, B., **Gibson, C.C.,** Fernandez, E., Clark, D., Felton, J., Fielding, S., Gray, M., Koller, J., Norwood, A., Spurlock, R., Nierenberg, N., Ulysse, J.C., Berggren, R. "Sustainable Healthcare in the Central Plateau of Haiti." University of Texas Medical Community Service Learning Conference, Poster and discussion panelist. April 2, 2009.

**Gibson, C.C.**, Rooney, T., Elam, A., Metwalli, Z., Robb, R., Liebschner, M., "Advanced Space Health Maintenance System: Technology Enabling Extended Manned Space Exploration". Conference Proceedings: SPACE 2005, Long Beach, CA. October 2005.
**Gibson, C.C.**, Rooney, T., Elam, A., Metwalli, Z., Robb, R., Liebschner, M., "STEVE: Spine and Trochanter External Vibration Effector". Conference Proceedings: Revolutionary Aerospace Academic Linkage, Cape Canaveral, FL. May, 2005.

## *Patents*

William Marsh Rice University. Inventors: M. Liebschner, **C. Gibson**, T. Rooney, A, Elam, Z. Metwalli, and R. Robb. 2006. Vibration and Compression Countermeasure Harness and Belt for Bone and Muscle Loss in microgravity. Patent Cooperation Treaty Application. WO/2006/110545, filed Oct. 19, 2006. Patent Pending.

## *Industry Experience*

*2004 – 2005*
**Project Manager**
*Medi-Screw, Inc., Portland, Oregon*
Life-Science startup company; developed novel pedicle-screw head system for increased operating room control. Managed manufacturing, directed research plan, and developed research protocols. Reported directly to CEO.

*Summer 2004*
**Business Development Intern**
*Medi-Screw, Inc., Portland, Oregon*
Wrote business plan, created venture capital presentations, presented to venture capitalists, and researched customers and markets. Primary liaison to project engineer.

## *Teaching Experience*

*2011-present*
**Mentor,** Research mentor to young graduate students, one post-baccalaureate student, and two high school students working in the Li Lab.
Dr. Dean Y. Li
The University of Utah

*2010 – 2011*
**Teaching Assistant and Lecturer,** *Physics of the Human Body.*
The University of Utah

*Summer 2007*
**Teaching Assistant,** *Human Gross Anatomy, CSBL 5019.*
Dr. Ron Philo.
The University of Texas Health Science Center at San Antonio

*Spring 2006*
**Teaching Assistant,** *Advanced Biomaterials, ME 6973*
Dr. Jeffrey Y. Thompson.
The University of Texas at San Antonio

## *Leadership, Honors, and Awards*

2009
Member, UTHSCSA Energy Conservation Committee, Appointed by Executive V.P. and COO, UTHSCSA.

| | |
|---|---|
| 2009 | Selected Participant, American Medical Student Association Environmental Health Leadership Institute, Mount Sinai School of Medicine. |
| 2009 | President and Founder, 'Sustainability Club' student group, UTHSCSA. |
| 2009 | Co-President and Co-Founder, "Project Haiti' student group, UTHSCSA. |
| 2008-2009 | Greehey MD/PhD Scholarship, University of Texas Health Science Center at San Antonio. Tuition, benefits, and $21,500 yearly stipend. |
| 2008 | UT Health Sciences Center at San Antonio Alumni Merit Award for service to the University, First-Year Medical Student - $1000.00. |
| 2008 | Big Brothers and Big Sisters of South Texas 'Big Couple' of the Year. |
| 2007-2009 | UTHSCSA Green Initiative Student Leader**.** Worked with Executive VP, created "Green Initiative Task-Force". New building policies, recycling policies, energy policies, and other 'green' policies instituted campus-wide. |
| 2006-2007 | President, Biomedical Engineering Society, Joint Ph.D. Program in Biomedical Engineering at the University of Texas Health Science Center at San Antonio and the University of Texas at San Antonio. |
| 2005 | First Place Team, Revolutionary Aerospace Academic Linkage Undergraduate Research and Design Competition. Kennedy Space Center, Florida. |
| 2005 | Nine team awards including "Legends Award", Texas Space Grant Consortium Undergraduate Research and Design Competition Spring Design Challenge. Johnson Space Center, Texas. |
| 2004 | Six team awards including "Best Poster" and "Best Presentation", Texas Space Grant Consortium Undergraduate Research and Design Competition Fall Design Challenge. Johnson Space Center, Texas. |
| 2004 | Undergraduate Representative, 2004 Rice University, Dean of Engineering Search Committee (Appointed). |
| 2002-2003 | College Representative, Martel College, Rice University (Elected). |
| 2001-2002 | Western Athletic Conference (WAC) Scholar-Athlete, NCAA Division 1 Men's Track and Field. |
| 2001- 2003 | Rice University Men's Track and Field Team. NCAA Division-1. Decathlon. |

## *Medical Arts, Writing, and Ethics – Electives and Publications*

| | |
|---|---|
| 2013 | **Christopher C. Gibson.** *Why the conversations that start in TEDMED need to continue.* Guest Column. **KevinMD.com**, May 11th, 2013 |
| 2010 | *Writing Medical Experience¸* Medical Elective Education, University of Utah. |
| 2010 | **Christopher C. Gibson.** *Haitians Can Teach Us.* Opinion Column. **Deseret News**, January 16th, 2010. |

| | |
|---|---|
| 2010 | **Christopher C. Gibson.** *Reaching out to a devastated Haiti*. Opinion: letters. **New York Times**, January 14th, 2010. |
| 2008-2009 | *Literature and Medicine*, Medical Student Elective Education, UTHSCSA. |
| 2008 | *The History of Anatomy*, Medical Student Elective Education, UTHSCSA. |
| 2008 | *Issues in Death and Dying,* Medical Student Elective Education, UTHSCSA. |

## *Volunteering and Service*

| | |
|---|---|
| 2009 | Participant, UTHSCSA medical service trip to Thomonde, Haiti. |
| 2009 | UTHSCSA Haiti Nutrition Center Fundraising Leader. |
| 2008 | Trip-leader, Inaugural UTHSCSA medical service trip to Thomonde, Haiti. |
| 2006 – 2009 | Big Brother<br>*Big Brothers and Big Sisters of South Texas* |